Reliability-Based Calibration for the Design and Load Rating of Segmental Bridges

by

Karina Popok

A dissertation submitted to the Graduate Faculty of
Auburn University
in partial fulfillment of the
requirements for the Degree of
Doctor of Philosophy

Auburn, Alabama
December 14, 2024

Keywords: segmental bridge, service limit state, load rating, prestressed concrete, reliability of structures, reliability-based calibration

Approved by

Andrzej S. Nowak, Chair, Professor, Department of Civil and Environmental Engineering
Robert W. Barnes, Co-Chair, Professor, Department of Civil and Environmental Engineering
Mary Hughes, Senior Lecturer, Department of Civil and Environmental Engineering
Jeffrey LaMondia, Professor, Department of Civil and Environmental Engineering

Abstract

This dissertation addresses the need for rational provisions in the design and load rating of segmental bridges, emphasizing clearer distinctions between the inventory level, which demands higher reliability, and the operating level, which requires a lower level of reliability. Bridge engineers have advocated for less stringent evaluations at the operating level, prompting a request to refine the AASHTO Manual for Bridge Evaluation (MBE) provisions to better reflect operational conditions.

The reliability analysis was conducted for both service and strength limit states. The primary objective of this study is to determine and validate the load and resistance factors required for the design and load rating for the Service III limit state, which governs post-tensioned segmental bridge superstructure components. This involved the statistical analysis of segmental bridges, the selection of representative bridges, the formulation of limit state functions, the selection of a reliability analysis procedure, and the determination of the target reliability index. Statistical models of load and resistance were developed, including parameters for thermal gradient, fabrication factor for flexural strength, and yield stress of reinforcing bars for shear strength.

Reliability analysis was conducted for the selected representative bridges across the considered limit states, and target reliability indices were determined. The load and resistance factors for the service limit state were then calibrated and verified, and the effect of the proposed changes on the rating factors was determined.

The main results include recommendations for updating provisions for the operating rating of segmental bridges. These findings are expected to be valuable for designers and load rating engineers of post-tensioned segmental bridges.

Acknowledgments

I would like to express my deepest gratitude to my advisor, Professor Andrzej Nowak, for providing me with the unique opportunity to pursue the Ph.D. degree at Auburn University, as well as his guidance and support throughout this journey. His expertise in structural reliability and bridge engineering has been incredibly valuable and was especially helpful during my research. His early conversations with industry practitioners provided vital insights into the advantages of segmental bridge construction and highlighted the importance of utilizing these benefits in bridge evaluation.

I would like to express my heartfelt gratitude to my co-advisor, Professor Robert Barnes, for his invaluable assistance in helping me understand various aspects of reinforced and prestressed concrete behavior. His support was especially crucial during the final stages of my dissertation.

I would like to thank my committee members, Professor Jeffrey LaMondia and Lecturer Mary Hughes, for their invaluable insights, assistance, and encouragement throughout this research. I also extend my thanks to Professor Oladiran Fasina for serving as a university reader. His feedback was enlightening and helpful.

I would like to thank the National Cooperative Highway Research Program (NCHRP) for sponsoring a major part of this research and the NCHRP 12-123 “Proposed AASHTO Guideline for Load Rating of Segmental Bridges” project team for their collaborative efforts and insights, which greatly enhanced my understanding of segmental bridges and structural reliability. Special thanks to Dr. Andrzej Nowak, Dr. Robert Barnes, Dr. Pablo Hurtado, Dr. Jacek Chmielewski (Auburn University), Dr. Hani Nassif, Dr. Patrick Lou (Rutgers University), Dr. Fatmir Menkulasi, Dr. Christopher Eamon (Wayne State University), John Corven (Hardesty & Hanover / Corven Engineering), Eddie He, and Benjamin Morris (Parsons). I also extend my gratitude to John Corven

and the Departments of Transportation in Alabama, California, Colorado, Massachusetts, Michigan, and Texas for providing the bridge data. Much of the work presented in this dissertation is also documented in the NCHRP 12-123 final project report (Popok et al. 2024).

My gratitude also goes to the Precast/Prestressed Concrete Institute (PCI) for co-sponsoring the present research under the study “Calibration of Flexural Strength Reduction Factor for Precast, Prestressed Concrete Slabs and Beams” (Popok et al. 2021) and to the project team for their guidance on the specifics of precast, prestressed concrete construction compared to cast-in-place concrete. Special thanks to Dr. Andrzej Nowak, Dr. Robert Barnes, Dr. Anton Schindler, Dr. Victor Aguilar, and Dr. Pablo Hurtado.

I am grateful to the Concrete Reinforcing Steel Institute (CRSI) for providing data on reinforcing steel properties, which was crucial for deriving the statistical parameters of yield strength. A portion of this work was supported by the American Concrete Institute (ACI) Foundation under the study "Reliability Evaluation of ACI 318 Strength Reduction Factor for One-Way Shear” (Aguilar et al. 2024) . I extend my gratitude to the American Concrete Institute (ACI) Foundation for their support, as well as to the project team: Dr. Robert Barnes, Dr. Andrzej Nowak, Dr. Victor Aguilar, and Dr. Pablo Hurtado.

I appreciate the Midas team for providing our institution with the academic license for Midas Civil software, enabling the finite-element modeling of the bridges.

Special appreciation goes to the professors of the Civil and Environmental Engineering Department, whose courses I have taken, for enriching and broadening my technical knowledge. I would like to extend my heartfelt thanks to Dr. Olga Iatsko, whose support was instrumental in making this journey possible. I am also deeply grateful to my amazing research group: Dr. Anjan

Babu, Dr. Victor Aguilar, Dr. Jacek Chmielewski, Dr. Sylwia Stawska, Dr. Pablo Hurtado, Andrea Kouame, Aneta Luszczynska, and Rafal Roszczenko.

I would like to deeply thank my mother, Nadiia Popok, for her unwavering dedication that is not subject to any circumstances, her endless patience, and for her constant encouragement. I am also grateful to my aunt, cousins, and nephews. Even though we are far apart, I know you are with me in spirit.

Lastly, I would like to take a moment to reflect on the ongoing war in Ukraine. As a proud Ukrainian, I am deeply affected by the challenges my country faces. I encourage people from all over the world to stand with Ukraine and support efforts towards peace and rebuilding. Your solidarity and support mean a great deal to us, who are striving for a brighter future for our nation.

Dedicated to my mother

Table of Contents

List of Tables

List of Figures

Chapter 1. INTRODUCTION

1.1 Overview of Segmental Bridges

A segmental bridge is a bridge type constructed in short sections, or segments, as opposed to large, continuous spans (Figure 1-1). These segments can be either cast-in-place—constructed directly at the final location—or precast at a different site and then transported to the construction site. Segmental bridges typically have one- or two-cell box cross sections (Figure 1-2). This construction method is particularly economical and efficient for moderate- to long-span bridges, especially in cases where site access is constrained (Lucko 1999).

Figure 1-1 Segmental Bridge Structure. Source: Datai Crane (2024)

Segmental bridges are often selected for their aesthetic qualities and their adaptability to complex and challenging environments. The step-by-step construction process allows for enhanced precision and flexibility, while also facilitating the management of stresses and loads

during construction. This makes segmental bridges a preferred choice for many contemporary bridge projects (Lucko 1999; Huang and Hu 2020).

a) 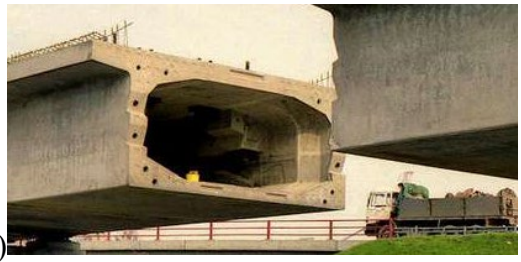 b) 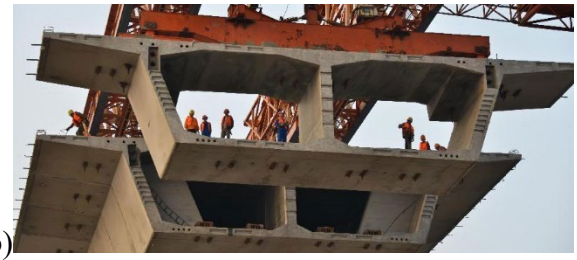

Figure 1-2 Examples of: a) One-Cell Box Cross Section, and b) Two-Cell Box Cross Section. Sourses: RePicture (2024); CivilArc (2024)

The joints between segments are the critical components of a segmental bridge. They play a key role in maintaining structural integrity, durability, flexibility, and ease of construction, as well as facilitating maintenance. Proper stress management at these joints is essential to prevent localized failures and ensure the long-term performance of the bridge. There are two primary types of joints between segments: Type A, which utilizes epoxy, and Type B, which is a dry joint without epoxy (Corven Engineering 2004).

1.2 Motivation and Problem Statement

Segmental bridges were first constructed in the United States during the 1970s. The initial segmental bridges were designed, built, and load rated using techniques that were not explicitly covered by the guidelines of the American Association of State Highway and Transportation Officials (AASHTO). Consequently, the application of AASHTO's load factor rating (LFR) and the current load and resistance factor rating (LRFR) methodologies often results in a significant decrease in capacity for existing segmental bridges compared to what was anticipated in the original design. Furthermore, the existing AASHTO LRFR method for load rating contemporary segmental bridges, as outlined in the AASHTO Manual for Bridge Evaluation (AASHTO MBE

2018), offers limited guidance for accurately load rating these structures due to their intricate nature. Additionally, the resources available in academic literature are seldom presented in a comprehensive format that is directly applicable for load rating according to AASHTO standards.

Another challenge is that the AASHTO Load and Resistance Factor Design (LRFD) specifications were developed and calibrated nearly three decades ago. This calibration, performed to ensure that bridge components were designed to achieve a consistent and desired level of reliability, was only conducted for girder-type bridges. The most recent edition of these specifications is AASHTO LRFD (2020). Likewise, the most recent calibration of (AASHTO MBE 2018) did not include segmental bridges. Therefore, the current level of reliability achieved when rating segmental bridges using the load and resistance factors developed for girder bridges may not be suitable. Specifically, segmental bridges are often assessed using overly conservative criteria, resulting in a reliability level higher than intended.

Design and load rating of segmental bridges are typically governed by allowable stresses at the service limit state. Serviceability limit states (SLS) necessitate a different approach compared to ultimate limit states (ULS). While ULS considers a single instance of heavy load, SLS takes into account both the magnitude and the frequency of load occurrences (Nowak and Grouni 1986). Service limit state focuses on durability rather than ultimate failure.

The AASHTO LRFD (2020) specifies the following service limit state load combinations:

- Service I: Pertains to the normal operational use of the bridge, accounting for a 70-mph wind and all loads at their nominal values. It is also used to control crack width in reinforced concrete structures, and for transverse analysis involving tension in concrete segmental girders. Compression in prestressed concrete components and tension in prestressed bent caps are also investigated using this load combination.

- Service II: Designed to control the yielding of steel structures and the slip of slip-critical connections under vehicular live loads.
- Service III: Used for longitudinal analysis, addressing tension in prestressed concrete superstructures to control cracking, and principal tension in the webs of segmental concrete girders.
- Service IV: Relates only to tension in prestressed concrete columns with the objective of crack control.

The Service III limit state is used to evaluate tensile stresses in prestressed concrete components. As segmental bridges are generally controlled by allowable stresses at the service limit state, Service III is a key consideration for their assessment.

Bridge engineers highlighted the superior quality of segmental bridge construction compared to other types and expressed a desire to leverage this advantage in bridge evaluation (Popok et al. 2024). Specifically, they emphasized the need for a clearer distinction between the inventory level of load rating for segmental bridges, which demands higher reliability, and the operating level, which requires a lower level of reliability. The *inventory* level of load refers to the load rating that allows comparisons with the capacity of new structures, indicating a live load that an existing structure can safely carry indefinitely. In contrast, the *operating* level of load describes the maximum permissible live load for an in-service structure under current conditions, but not indefinitely, allowing for occasional higher loads. Bridge engineers have stated that the current methodology for evaluation of segmental bridges at the operating level is too restrictive and have advocated for a less stringent evaluation at this level. As a result, it was requested that the AASHTO MBE provisions for load rating of segmental bridges be refined to better account for

these considerations, particularly to provide more efficient guidelines for load rating the bridges under operational conditions.

Therefore, there is a pressing need to determine and implement a consistent and rational target reliability level for segmental bridges, ensuring that the LRFR procedure is specifically calibrated to maintain this level for design and rating purposes. The aim of this research is to address this gap and conduct an LRFD and LRFR calibration for segmental bridges based on logical criteria.

1.3 Research Objectives

The objectives of this research are to:

1) Develop a reliability-based calibration procedure for the Service III limit state tailored to post-tensioned segmental bridge superstructure components,
2) Determine and validate the load and resistance factors required for the design and load rating of Service III limit state in post-tensioned segmental bridge superstructure components.

The ultimate goal is to achieve a level of reliability that aligns with similar superstructure components of girder-type bridges. This alignment is based on the standards in the AASHTO LRFD Bridge Design Specification and AASHTO Manual for Bridge Evaluation.

1.4 Background

1.4.1 Reliability of Structures and Limit State Design of Structural Components

1.4.1.1 Historical Perspective

In the past, uncertainties in load and resistance calculations were managed using a single, global safety factor. This is exemplified by the Allowable Stress Design (ASD) method, which includes a safety margin in the conservative allowable stress. However, a more nuanced approach was later developed, known as the Load and Resistance Factor Design (LRFD) methodology. This method applies load factors to each load component (such as dead, live, wind, snow, earthquake loads, etc.) to account for their associated uncertainties, and a resistance factor to account for uncertainties in load-resisting capacity (Nilson, Darwin, and Dolan 2004; Wight 2015). The latest versions of most major design and construction codes now follow this LRFD philosophy, which aims to design more efficiently and manage risk in a rational manner.

Reliability analysis procedures have been in development since the 1970s. Load and load combination models were formulated using available data, with Turkstra's Rule being the most widely applied method today (Benjamin and Cornell 1970; Nowak and Collins 2013). Similarly, resistance models were developed based on available data (Benjamin and Cornell 1970; Nowak and Collins 2013).

The structural load is subject to variability, particularly the live load, which changes with time and differs in various locations. Besides the clear variability in loads that structures encounter, there are multiple sources of uncertainty intrinsic to structural design. For instance, concrete compressive strength, reinforcement yield strength, and material unit weight often show different observed values under identical test conditions. Therefore, these design parameters can be treated as random variables. A random variable is a concept that is explained by considering the results of

an experiment. If an experiment is repeated under precisely the same conditions and the results are identical, then the measured variables can be considered deterministic. However, if the results vary, then the variables are random (Hart 1982). Since load and resistance are random variables, absolute safety (or zero probability of failure) is unattainable. As a result, structures must be designed to fulfill their functions with a certain finite probability of failure (Nowak and Collins 2013).

The approach to dealing with uncertainties can differ based on the situation. If the variability is small and the consequences of exceeding acceptable values are not severe, the uncertainty can be ignored, and the variable can be set equal to the best available estimate. This is often the case with the elastic moduli of materials, or the physical dimensions of components built with a high level of quality control. If the uncertainty is significant, it may be necessary to use a safe ("conservative") estimate of the variable. This is the case with the specified minimum strength properties of materials and members. This raises some questions: How can engineers maintain consistency in their conservatism from one situation to another (Benjamin and Cornell 1970)? How can they maintain consistency in the degree of conservatism within the same construction project? The design strengths of various structural components in a building should be consistent, reflecting a level of safety that is appropriate given the potential consequences of the failure mode considered. Reliability-based methods have been used in the development of modern design codes to answer these questions. The reliability-based calibration in this study is applied to the post-tensioned segmental bridge superstructure components for the service limit state. This is particularly relevant as segmental bridges are usually regulated by allowable stresses at service (Corven Engineering, 2004; Wassef et al. 2014).

1.4.1.2 Reliability Analysis

This section introduces the concepts of reliability analysis, including the limit state function, probability of failure, reliability index, and design formula. This information is adapted from (Nowak and Collins 2013).

A structure or structural component is designed to resist an expected load. If the load effect is represented by Q and the resistance (load-carrying capacity) by R, the condition of the structure can be assessed by considering the function g, defined as:

$$g = R - Q \tag{1-1}$$

If $g \geq 0$, the structure is considered safe; otherwise ($g < 0$), failure occurs. The limit state of the structure can be mathematically expressed using the limit state function $g = 0$.

$$g = R - Q = 0 \tag{1-2}$$

The probability of failure, P_f, is defined as the probability that $g < 0$. Assuming that the load, resistance, and limit state function variables are normal, their probability density function (PDF) distributions can be illustrated as shown in Figure 1-3.

$$P_f = P(g < 0) \tag{1-3}$$

If R and Q are normal random variables, then g is also a normal variable, and the probability of failure can be calculated using the following equation:

$$P_f = P(g < 0) = \Phi\left(-\frac{\mu_g}{\sigma_g}\right) \tag{1-4}$$

where μ_g is the mean of g, σ_g is the standard deviation of g, and Φ is the standard normal cumulative distribution function (CDF).

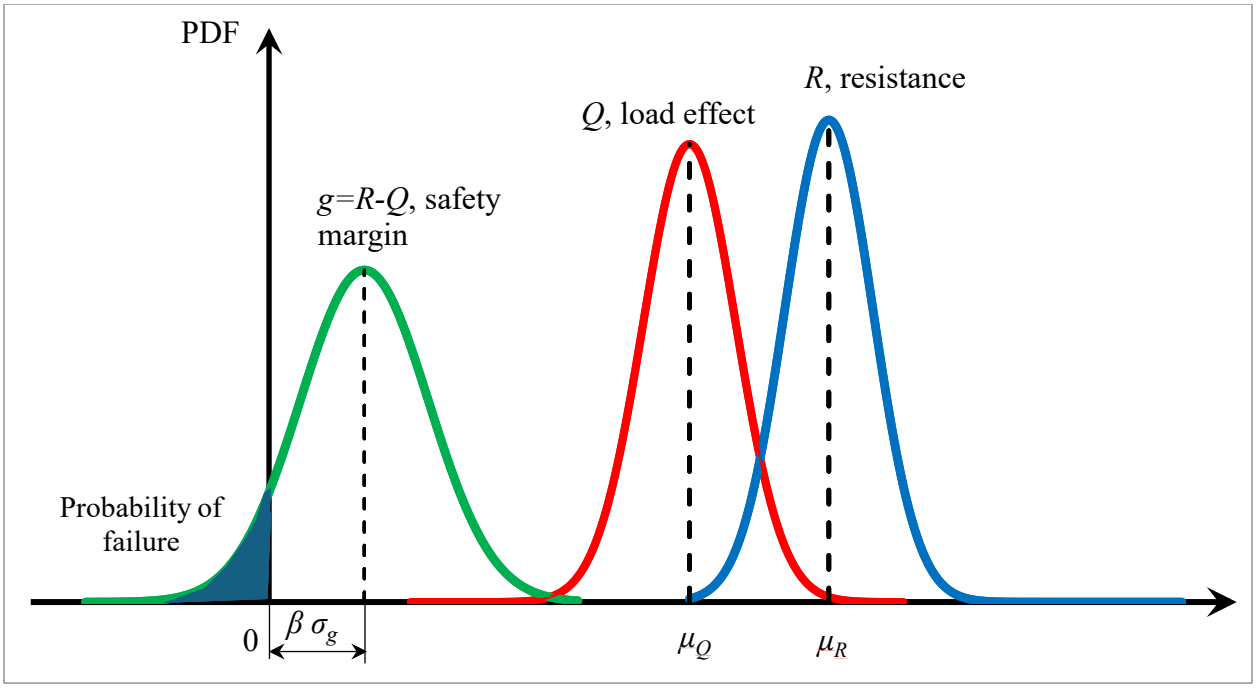

Figure 1-3 Normal Distributions of the Q, R, and g variables

(Adapted from Nowak and Collins 2013)

The reliability index, β, is a measure used to quantify the safety and reliability of a structure or component. It essentially indicates how likely a structure is to perform its intended function without failure over a specified period. The reliability index is defined as follows:

$$\beta = \frac{\mu_g}{\sigma_g} \tag{1-5}$$

Thus, the reliability index, β, is a function of the probability of failure (P_f). As the probability of failure decreases, the reliability index increases.

Reliability index, reliability, and probability of failure values are essential for determining the target level of safety, or the target reliability index (β_T). If the limit state function is linear and all variables follow a normal distribution, then β is related to the reliability and probability of failure as shown in Table 1-1. Otherwise, these relationships are approximate. The acceptance

criterion for structural performance is the ability to achieve a reliability index close to a predetermined target value, β_T.

Design parameters vary due to uncertainties and can be treated as random variables, including load components, concrete compressive strength, prestressing strength, prestressing strand location, etc. In reliability analysis, Q is treated as the total load, representing the sum of various load components. Different load combinations are used to account for varying conditions and influences on the structure. For instance, one combination may include the dead load due to the structure's self-weight (DC), dead load due to wearing surfaces and utilities (DW), and the live load (LL). Consequently, the limit state function is expressed as:

$$g = R - (DC + DW + LL) = 0 \tag{1-6}$$

Table 1-1 Reliability Index, Reliability, and Probability of Failure (Nowak 1999)

Reliability Index β	**Reliability** $S = 1 - P_f$	**Probability of Failure** P_f
0.0	0.500	0.500×10^{0}
0.5	0.691	0.309×10^{0}
1.0	0.841	0.159×10^{0}
1.5	0.933 2	0.668×10^{-1}
2.0	0.977 2	0.228×10^{-1}
2.5	0.993 79	0.621×10^{-2}
3.0	0.998 65	0.135×10^{-2}
3.5	0.999 767	0.233×10^{-3}
4.0	0.999 968 3	0.317×10^{-4}
4.5	0.999 996 60	0.340×10^{-5}
5.0	0.999 999 713	0.287×10^{-6}
5.5	0.999 999 981 0	0.190×10^{-7}
6.0	0.999 999 999 013	0.987×10^{-9}

where *DC, DW, LL*, and *R* are random variables corresponding to the load effects described above, and corresponding resistance, respectively. The corresponding design formula is:

$$\phi R_n \geq \gamma_{DC} DC_n + \gamma_{DW} DW_n + \gamma_{LL} LL_n \quad (1\text{-}7)$$

where DC_n, DW_n, LL_n, and R_n are the nominal (expected) values of the dead load effects, live load effect, and corresponding resistance, respectively, γ_{DC}, γ_{DW}, and γ_{LL} are the load factors for the corresponding load effects, and ϕ is the resistance factor. Nominal values are what is used in the design and rating.

Load and resistance factors are used to ensure safety and reliability in the design of structures. Load factors are multipliers applied to the nominal loads to account for uncertainties in the load estimates. These factors typically increase the loads to ensure that the structure can handle unexpected increases in load. The exception is load factors for Service Limit States, which are discussed further in the document. Resistance factors are multipliers applied to the nominal resistance of a structure to account for uncertainties in material properties, construction methods, and other factors, which are also discussed in more detail further. These factors reduce the nominal resistance to ensure a margin of safety.

1.4.2 Evolution of Bridge Design and Load Rating Calibration

1.4.2.1 Strength Limit States

The initial calibration of the AASHTO LRFD Bridge Design Specifications was conducted during the 1990s and published in NCHRP Report 368 (Nowak 1999). This work involved the reliability analysis of typical existing girder bridge structures with respect to Strength Limit States. The target reliability index for these limit states was set at β_T = 3.5, and the corresponding live load factor was established as γ_{LL} =1.75. This factor was subsequently adopted by the AASHTO LRFD Bridge

Design Specifications and incorporated into the design formula with a load combination of dead and live loads as follows:

$$\phi R_n \geq 1.25DC_n + 1.5DW_n + 1.75LL_n \quad (1\text{-}8)$$

Load rating refers to the evaluation of the structural capacity of existing bridges. This process involves assessing the bridge's ability to safely carry loads based on its current condition, design, and materials, ensuring that it meets the necessary safety standards for continued operation.

The first calibration of load factors for LRFR evaluation of existing bridges was conducted and published in NCHRP Report 454 (Moses 2001). Design load rating is an assessment of an existing bridge based on the HL-93 loading and LRFD design standards, using dimensions and properties of the bridge in its present as-inspected condition. It is a measure of the performance of existing bridges relative to current LRFD bridge design standards. Under this check, bridges are screened for the strength limit state at the LRFD design level of reliability. The load-rating level that precisely corresponds to the LRFD design level of reliability, including the same live load factors, is the inventory rating. The two levels of design rating, namely inventory and operating ratings, are discussed further in this section. The load rating also considers all applicable LRFD serviceability limit states (AASHTO MBE 2018).

AASHTO MBE (2018) prescribes the determination of load ratings using the *rating factor*. A rating factor quantifies the capacity of a bridge to safely carry loads relative to the loads it is anticipated to experience. It serves as a measure to evaluate the structural adequacy of bridges and ensure safety. Specifically, the rating factor is calculated as the ratio of the bridge's available live load capacity, inclusive of safety margins, to the prescribed live load. The rating factor equation is derived from fundamental principles of structural engineering, balancing demand (loads) and capacity (resistance) within structural systems, as shown below.

The capacity for the load rating calculations is expressed as follows:

$$C = \phi_c \, \phi_s \, R_n \tag{1-9}$$

where ϕ_c is the condition factor, and ϕ_s is the system factor.

Modifying the load components as per AASHTO MBE (2018), inequality (1-8) can be generally rewritten as follows:

$$C \geq \gamma_{DC} DC + \gamma_{DW} DW \mp \gamma_P P + \gamma_{LL}(LL + IM) \tag{1-10}$$

where P is permanent loads other than dead loads, including prestress; IM is the dynamic load allowance; and γ_P is load factor for permanent loads other than dead loads.

By moving all factored loads other than the live load to the left-hand side, the live load capacity will be on the left-hand side and the live load demand on the right-hand side, as follows:

$$C - \gamma_{DC} DC - \gamma_{DW} DW \pm \gamma_P P \geq \gamma_{LL}(LL + IM) \tag{1-11}$$

The rating factor (RF) is introduced to account for the difference between the live load capacity and demand, in order to make it an equality, as follows:

$$C - \gamma_{DC} DC - \gamma_{DW} DW \pm \gamma_P P = RF \cdot \gamma_{LL}(LL + IM) \tag{1-12}$$

Therefore, the rating factor can be expressed as:

$$RF = \frac{C - \gamma_{DC} DC - \gamma_{DW} DW \pm \gamma_P P}{\gamma_{LL}(LL + IM)} \tag{1-13}$$

The LRFR methodology defines two levels of the design load rating (AASHTO MBE 2018):

- Inventory Rating—allows comparisons with the capacity of new structures. Therefore, inventory rating results in a rating factor relative to a live load that could safely utilize an existing structure for an indefinite period of time.

- Operating Rating—generally describes the maximum permissible live load to which an in-service structure may be subjected under the current operating conditions, but not indefinitely. This level permits a less stringent evaluation, implying lower levels of reliability and allowing for occasional higher loads without compromising the overall safety or serviceability.

Since the inventory rating corresponds to the same level of reliability as the design, the target reliability index β_T and the corresponding live load factor γ_{LL} for this level of evaluation were proposed in NCHRP Report 454 (Moses 2001) to be the same as those established in NCHRP Report 368 (Nowak, 1999), with β_T = 3.5 and γ_{LL} = 1.75. The target reliability index for the Operating Rating was determined as β_T = 2.5 with the corresponding live load factor γ_{LL} = 1.35 and the design formula as (Moses 2001):

$$\phi R_n \geq 1.25DC_n + 1.5DW_n + 1.35LL_n \quad (1\text{-}14)$$

1.4.2.2 Service Limit States

The AASHTO Standard Specifications (AASHTO Standard 2002), which preceded the AASHTO LRFD, assigned all load and resistance factors as 1.0 for Service Limit States. Under these conditions, the design formula for a load combination of dead and live loads is expressed as follows:

$$R_n \geq DC_n + DW_n + LL_n \quad (1\text{-}15)$$

The design live load specified in the AASHTO LRFD Specifications (HL-93) generates higher unfactored, undistributed load effects in prestressed concrete bridge girders than those generated by AASHTO Standard Specifications load (HS-20). The girder distribution factors, particularly for interior girders, are lower in the AASHTO LRFD Specifications, reducing the

difference between the unfactored distributed load effects in both specifications. However, even with the smaller distribution factors, the unfactored distributed load effects in the AASHTO LRFD Specifications were still higher for most girder systems. Using the same load factor for the service limit state (γ_{LL} = 1.0) resulted in higher factored load effects in AASHTO LRFD designs compared to those designed under the AASHTO Standard Specifications. Trial designs conducted during the development of the AASHTO LRFD Specifications indicated a need for more prestressing strands than required by the AASHTO Standard Specifications. This suggests that designs following the AASHTO Standard Specifications may have led to under-designed components, potentially prone to cracking. In the absence of widespread cracking, the live load factor was reduced to γ_{LL} = 0.8. This adjustment led to a similar amount of required prestressing force in comparative concrete bridge designs conducted using the AASHTO Standard and the AASHTO LRFD Specifications (Wassef et al. 2014).

In the study completed during NCHRP Project 12-83 (Wassef et al. 2014) the refined live load factor for the Service III Limit State was calibrated. Before 2005, the AASHTO LRFD Specifications included a simple method for estimating time-dependent prestress losses, known as the "Approximate Lump Sum Estimate of Time-Dependent Losses" (Wassef et al. 2014). In 2005, a new method to determine the time-dependent prestress losses was introduced, named "Refined Estimates of Time-Dependent Losses" (Wassef et al. 2014). The post-2005 method is considered to provide a more accurate estimate of prestressing losses (Tadros et al. 2003; Wassef et al. 2014). This method introduced new equations for calculating time-dependent prestressing losses, including the use of transformed section properties, and explicitly incorporated the concept of "elastic gain." After the initial prestressing loss at transfer, when load components that generate tensile stresses in the concrete near the strand locations are applied to the girder, the strands

experience additional tensile strain, equal to the strain in the surrounding concrete due to the applied loads. This results in an increase in the force within the strands, referred to as "elastic gain." The post-2005 prestressing loss method allows this elastic gain to offset some of the prestressing losses (Wassef et al. 2014).

The post-2005 prestress loss method frequently resulted in lower prestressing force losses leading to fewer required prestressing strands than those specified under the AASHTO Standard Specifications and earlier AASHTO LRFD Specifications. This raised concerns, as the higher prestressing losses calculated by the pre-2005 method helped offset the lower live load effects due to the reduced design live load in the AASHTO Standard Specifications or the lower load factor used in the Service III load combination of the AASHTO LRFD Specifications (Wassef et al. 2014). The NCHRP Project 12-83 demonstrated that sections designed using the post-2005 method exhibit lower reliability indices compared to those designed using the pre-2005 method. To address this issue, the live load factor for these sections was increased to $\gamma_{LL} = 1.0$, compensating for the lower reliability indices.

In the AASHTO MBE (2018) load-rating equation, the capacity for service limit states is defined as the allowable stress specified in the LRFD code, f_R:

$$C = f_R \tag{1-16}$$

The allowable stresses, or stress limits, for prestressed concrete are delineated in AASHTO LRFD (2020) Article 5.9.2.3, both prior to and following prestress losses. Specifically, the AASHTO LRFD tensile stress limits for segmental bridges after losses are detailed in Table 1-2. In joints and other areas without bonded reinforcement, no tension is allowed. Conversely, in joints and other areas with bonded reinforcement, a certain amount of tension is allowed. The allowable stress is related to the modulus of rupture, f_r, which is defined as $0.24\lambda\sqrt{f'_c}$ ksi (AASHTO LRFD

2020). The tested units for the modulus of rupture were either 4.0 or 6.0 inches deep. It has been demonstrated that the cracking stress of concrete members significantly decreases with increasing member depth. Consequently, the cracking stress for bridge members, which have a significantly greater depth than the tested units, is lower than that of the tested units composed of the same concrete. Therefore, the appropriate stress limits in Table 1-2, f_R, are lower than the modulus of rupture, f_r.

Table 1-2 Tensile Stress Limits in Prestressed Concrete at Service Limit State after Losses (Adapted from AASHTO LRFD 2020)

Bridge Type	**Location**	**Stress Limit, f_R**
Segmentally Constructed Bridges These limits may be used for normal weight concrete with concrete compressive strengths for use in design up to 15.0 ksi and lightweight concrete up to 10.0 ksi.	Longitudinal Stresses through Joints in the Precompressed Tensile Zone	
	Joints with minimum bonded auxiliary reinforcement through the joints sufficient to carry the calculated longitudinal tensile force at a stress of $0.5f_y$; internal tendons or external tendons	$0.0948\lambda\sqrt{f'_c} \leq 0.3$ (ksi)
	Joints without the minimum bonded auxiliary reinforcement through joints	No tension
	Transverse Stresses Tension in the transverse direction in precompressed tensile zone	$0.0948\lambda\sqrt{f'_c} \leq 0.3$ (ksi)
	Stresses in Other Areas For areas without bonded reinforcement	No tension
	In areas with bonded reinforcement sufficient to resist the tensile force in the concrete computed assuming an uncracked section, where reinforcement is proportioned using a stress of $0.5f_y$, not to exceed 30.0 ksi	$0.19\lambda\sqrt{f'_c}$ (ksi)
	Principal tensile stresses in webs	$0.110\lambda\sqrt{f'c}$ (ksi)

1.4.3 Segmental Bridge Provisions and Guidelines

1.4.3.1 Bridge Design Provisions

The AASHTO *Guide Specifications for Design and Construction of Segmental Bridges* was initially introduced in 1989 to address the unique needs of segmental bridges, offering comprehensive guidelines on design, construction techniques, prestressing methods, and joint connections to ensure the safety, efficiency, and longevity of these structures. The second edition of the AASHTO Guide Specifications was published in 1999 (AASHTO Guide Specifications 1999), with the last revisions made in 2002. Since then, it has been archived and is now considered outdated, as newer specifications and methodologies have replaced it to align with current engineering practices and standards.

Article 5.12.5, "Segmental Concrete Bridges," in the current AASHTO LRFD Specifications, is largely derived from the AASHTO Guide Specifications for the Design and Construction of Segmental Concrete Bridges. This article addresses critical aspects of segmental bridge analysis, including the redistribution of construction-stage force effects, construction loads, and load combinations at both strength and service limit states. It also considers thermal effects during construction, time-dependent phenomena such as creep and shrinkage, and alternative shear design procedures for discontinuity regions. Additionally, it encompasses seismic design considerations. The article provides comprehensive information on various types of segmental bridges and includes provisions for the segmental construction of bridge substructures (AASHTO LRFD 2020).

There are three primary methods for constructing segmental bridges (AASHTO LRFD 2020 Article 5.12.5.4):

- *Span-by-span*: AASHTO LRFD (2020) Article C5.12.5.4.5 defines span-by span construction as

  > *construction … where the segments, either precast or cast-in-place, are assembled or cast on falsework supporting one entire span between permanent piers. The falsework is removed after application of posttensioning to make the span capable of supporting its own weight and any construction loads. Additional stressing may be utilized after adjacent spans are in place to develop continuity over piers.*

- *Balanced cantilever*: segments are alternately added on either side of a pier to maintain a balanced system, which minimizes bending moments and stresses on the piers and foundations. This method can be applied to both precast and cast-in-place cantilever construction. AASHTO LRFD (2020) Article 5.12.5.4.4 states,

  > *The cantilevered portion of the structure shall be investigated for overturning during erection. The factor of safety against overturning shall not be less than 1.5 under any combination of loads.*

  Additionally, Article C5.12.5.4.4 specifies,

  > *Stability during erection may be provided by moment resisting column/superstructure connections, falsework bents, or a launching girder. Loads to be considered include construction equipment, forms, stored material, and wind.*

- *Incremental launching*: involves building bridge segments in a casting yard behind one of the abutments and then pushing the completed segments forward along the bridge axis using hydraulic jacks. Each segment is match-cast against the previous one and prestressed

to form a continuous structure. This process is repeated until the entire bridge is in its final position. AASHTO LRFD (2020) Article 5.12.5.4.6 states,

> *Stresses under all stages of launching shall not exceed the limits specified in Article 5.9.2.3 for members with bonded reinforcement through the joint and internal tendons.*
>
> *Provision shall be made to resist the frictional forces on the substructure during launching and to restrain the superstructure if the structure is launched down a gradient.*

There are also two additional considerations in AASHTO LRFD (2020) specific to segmental bridges. As outlined in Section 1.2, AASHTO LRFD (2020) Article 3.4.1 mandates the consideration of principal tension in webs under the Service III limit state for segmental bridges. Additionally, with respect to the thermal gradient (*TG*) load effect, this article prescribes the evaluation of two load combinations involving *TG* and live load (*LL*) at service limit states, which are $\gamma_{LL}\,LL + 0.5TG$ and $1.0TG + 0LL$.

1.4.3.2 Bridge Load Rating Provisions

AASHTO MBE (2018) includes Article 6A.5.11, titled "Rating of Segmental Concrete Bridges", which outlines general rating requirements for segmental bridges, particularly for assessing load-rating capacity in both longitudinal and transverse directions.

AASHTO MBE (2018) Article 6A.5.11 also specifies that the number of striped lanes should be used as the number of live load lanes for operating rating, as opposed to the number of design lanes used in inventory rating. Striped lanes refer to the actual, physical traffic lanes marked on the roadway, representing real-world vehicle travel patterns across the bridge. In contrast,

design lanes are idealized, hypothetical lanes with a width of 12 ft, employed for bridge design. They represent the distribution of traffic loads for analytical purposes, independent of the actual striped lane configuration. An illustrative example of striped versus design lane configurations is depicted in Figure 1-4. Configuration 1 represents a scenario where the bridge is load-rated based on the number of striped lanes, while Configuration 2 illustrates a scenario where the bridge is load-rated based on the number of design lanes. The number of striped lanes is always less than or equal to the number of design lanes; consequently, a lesser or equal amount of live load would be applied for load rating at the operating level.

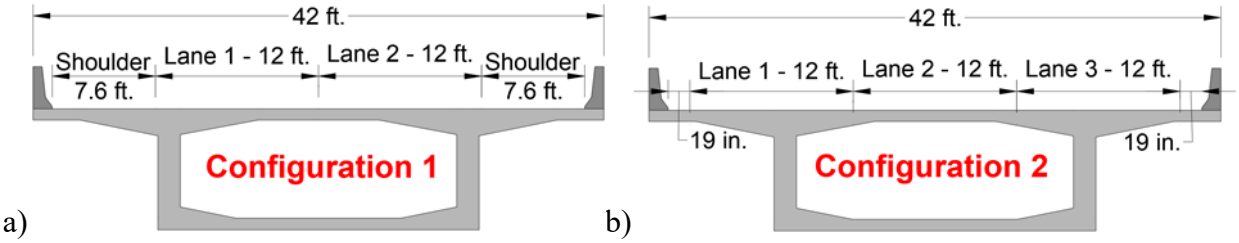

a) b)

Figure 1-4 Lane Configurations for the Concrete Segmental Bridge: a) Striped-Lane Configuration (Configuration 1); and b) Design-Lane Configuration (Configuration 2)

AASHTO MBE (2018) Article 6A.5.11 provides system factors for the longitudinal flexure of segmental bridges, accounting for appropriate redundancy. These system factors consider longitudinally continuous versus simply supported spans, the inherent integrity provided by the closed continuum of the box section, multiple-tendon load paths, the number of webs per box, and the types of details and their post-tensioning.

The Florida Department of Transportation (FDOT) developed specific provisions for the load rating of segmental bridges, detailed in the document titled "New Directions for Florida Post-tensioned Bridges – Volume 10A: Load Rating Post-tensioned Concrete Segmental Bridges"

(Corven Engineering 2004). This document presents a more comprehensive version of the load-rating equation, as follows:

$$RF = \frac{C - \gamma_{DC}DC - \gamma_{DW}DW \pm \gamma_{EL}(PS + EL) - \gamma_{FR}FR - \gamma_{CR,SH}(CR + SH) - \gamma_{TU}TU - \gamma_{TG}TG}{\gamma_{LL}(LL + IM)} \quad (1\text{-}17)$$

where *EL* is miscellaneous locked-in force effects resulting from the construction process, including jacking apart of cantilevers in segmental construction; *FR* is the friction load; *CR, SH, TU* and *TG* are force effects due to creep, shrinkage, uniform temperature, and temperature gradient, respectively; and γ_{EL}, γ_{FR}, γ_{CR}, γ_{SH}, γ_{TU}, and γ_{TG} are load factors for the corresponding load effects.

Corven Engineering (2004) includes a table detailing the allowable stresses for concrete bridges, separately for inventory and operating ratings (Table 1-3). The table specifies distinct stress limits for Type A and Type B joints, as well as for other areas beyond the joints. Additionally, it outlines higher stress limits for operating ratings. The stress values in Table 1-3 are indicated in psi units, whereas they are indicated in ksi units in Table 1-2. The conversion factor is $0.0316\sqrt{f'_c}$ ksi per $1\sqrt{f'_c}$ psi.

Table 1-3 FDOT Table 8.2.B - Allowable Stresses for Concrete Bridges

(Corven Engineering 2004)

At the Service Limit State after losses	Stress Limit INVENTORY Rating	Stress Limit OPERATING Rating	Source of Criteria
Compression (Longitudinal or Transverse):			
• Compressive stress under effective prestress, permanent loads, and transient loads	$0.60f'_c$	$0.60f'_c$	LRFD Table 5.9.4.2.1-1 Seg Guide Spec 9.2.2.1
• Allowable compressive stress shall be reduced accordingto AASHTO Guide Specification for Segmental Bridges when slenderness of flange or web is greater than 15 (For both New Design and Load Rating purposes)			Seg Guide Spec 9.2.2.1
Longitudinal Tensile Stress in Precompressed Tensile Zone: (Intended for Pre and Post-Tensioned Beams and similar construction)For components with bonded pretressing tendons or reinforcement that are subject to not worse than: For (a) an aggressive corrosion environment and (b) moderately aggressive corrosion environment For components with unbonded prestressing tendons	$3\sqrt{f'_c}$ psi tension No Tension	$7.5\sqrt{f'_c}$ psi tension No Tension	LRFD Table 5.9.4.2.2-1 and FDOT FDOT no distinction for Environ't LRFD Table 5.9.4.2.2-1
Longitudinal Tensile Stress through Joints in Precompressed Tensile Zone: (Intended for Segmental and similar construction)			
• Type A joints with minumum bonded auxiliary longitudinal reinforcement sufficient to carry the calculated longitudinal tensile force at a stress of0.5fy; for internal and/or external PT (e.g.cast-in-place construction) For (a) an aggressive corrosion environment and (b) moderately aggressive corrosion environment	$3\sqrt{f'_c}$ psi tension	$7.5\sqrt{f'_c}$ psi tension	LRFD Table 5.9.4.2.2-1 Seg Guide Spec 9.2.2.2 FDOT no distinction for Environ't
• Type A joints without the minimum bonded auxiliary longitudinal reinforcement through the joints; internal and/or external PT (e.g. match-cast epoxy joints or unreinforced cast-in-place closures between precast segments or between spliced girders or similar components.)	No Tension	No Tension	Ditto and FDOT Seg. Rating Criteria
• Type B joints (dry joints - no epoxy); external tendons:	100 psi min comp	No Tension	Seg Guide Spec 9.2.2.2 FDOT Seg. Rating Criteria
Transverse Tension, Bonded PT:			
• Tension in the transverse direction in precompressed tensile zone calculated on basis of uncracked section (i.e. top prestressed slab) For (a) an aggressive corrosion environment and (b) moderately aggressive corrosion environment	$3\sqrt{f'_c}$ psi tension	$6\sqrt{f'_c}$ psi tension	Seg Guide Spec 9.2.2.3 LRFD Table 5.9.4.2.2-1 FDOT no distinction for Environ't FDOT Seg. Rating Criteria
Tensile Stress in Other Areas:			
• Areas without bonded reinforcement	No tension	No tension	Seg Guide Spec 9.2.2.4 LRFD Table 5.9.4.2.2-1
• Areas with bonded reinforcement sufficient to carry the tensileforce in the concrete calculated on the assumption of an uncracked section is provided at a stress of 0.5fy (< 30 ksi)	$6\sqrt{f'_c}$ psi tension	$6\sqrt{f'_c}$ psi tension	Seg Guide Spec 9.2.2.4 LRFD Table 5.9.4.2.2-1
Principal Tensile Stress at Neutral Axis in Webs (Service III):			
• All types of segmental or beam construction with internal and/or external tendons.*	$3\sqrt{f'_c}$ psi tension	$4\sqrt{f'_c}$ psi tension	FDOT LRFR Rating Criteria

* Principal tensile stress is calculated for longitudinal stress and maximum shear stress due to shear or combination of shear and torsion, whichever is the greater. For segmental box, check neutral axis. For composite beam, check at neutral axis of beam only and at neutral axis of composite section and take the maximum value. Web width is measured perpendicular to plane of web. For segmental box, it is not necessary to consider coexistent web flexure. Account should be taken of vertical compressive stress from vertical PT bars provided in the web, if any, but not including vertical component of longitudinal draped post-tensioning - the latter should be deducted from shear force due to applied loads.
Check section at H/2 from edge of bearing or face of diaphragm, or at end of anchor block transition, whichever is more critical.
For the design of a new bridge, a temporary principal tensile stress of $4.5\sqrt{f'_c}$ psi may be allowed during construction - per AASHTO Seg. Guide Spec.

Initial load ratings for new design should be based upon specified concrete strength.
Load rating of an existing bridge should be based upon actual concrete strength from construction or subsequent test data.

1.4.4 Identified Literature Gaps

The existing literature provides a substantial number of provisions that generally address segmental bridges. However, these provisions do not comprehensively cover all specific aspects of segmental bridges, resulting in certain gaps.

Wassef et al. (2014) made significant advancements in refining the live load factor for service limit states. However, their focus was on transitioning the estimated time-dependent prestress losses from the "pre-2005" to the "post-2005" method, known as "Refined Estimates of Time-Dependent Losses", and the latter method was based on, and intended for, precast, prestressed girder bridges (Tadros et al. 2003), rather than segmental bridges. AASHTO LRFD (2020) mandates that time-dependent losses for segmental bridges be determined using the detailed time step method. Historically, segmental bridges have also been designed using gross-section properties rather than transformed-section properties employed in the "Refined Estimates of Time-Dependent Losses". The changes in prestress loss methods in 2005 did not impact the time step method (Tadros et al. 2003). Therefore, the increase in the load factor from $\gamma_{LL} = 0.8$ to $\gamma_{LL} = 1.0$ does not apply to segmental bridge sections designed using the time step method. Consequently, the live load factor specific to segmental bridge sections needs to be calibrated.

As mentioned in Section 1.4.3.2, AASHTO MBE (2018) prescribes using the number of striped lanes for operating rating, which implies applying a lower live load on a bridge than for inventory rating, thereby reducing reliability for operating rating as intended. However, Article C6A.5.11.4 notes that while using the number of striped lanes resulted in lower reliability for ratings at the service limit states compared to the reliability computed by using the number of design lanes, the resultant increment in β_T was unknown. AASHTO MBE (2018) C6A.5.11.4 references a brief study of existing bridges, which suggested that using the number of striped lanes

resulted in adequate operating ratings at the service limit states for well-performing segmental box girder bridges. This was not the case when using the number of design lanes. However, AASHTO MBE (2018) does not cite a source for this study. Therefore, a more precise reliability analysis should be conducted to calibrate guidelines for inventory and operating ratings and to ensure that the provisions are well justified.

In light of the identified literature gaps, it is imperative to calibrate the load and resistance factors for the Service III limit state in segmental bridges using a probabilistic approach.

1.5 Research Plan

The research plan for the present study involves implementing a reliability-based calibration procedure, adapted from previous reliability-based calibration studies (Nowak 1999; Wassef et. al. 2014), and encompasses the following steps:

1. Select representative structures.
2. Formulate limit state functions.
3. Establish the reliability analysis procedure.
4. Develop statistical parameters of load.
5. Develop statistical parameters of resistance.
6. Identify representative load and resistance design values.
7. Compute reliability for representative structures.
8. Select the target reliability index.
9. Calculate and verify load and resistance factors.

1.6 Organization

The subsequent chapters of this dissertation are organized as follows. Chapter 2 presents statistics on segmental bridges, the selection of representative structures, and the formulation of limit state functions for segmental bridges. Chapter 3 outlines the reliability analysis procedure. Chapter 4 focuses on developing statistical parameters for loads. Chapter 5 covers the development of statistical parameters for resistance. Chapter 6 discusses the application of reliability analysis to the selected representative structures, the selection of target reliability indices, and the derivation of load and resistance factors. Chapter 7 provides a summary of conclusions and offers recommendations for future work aimed at accurately reflecting the reliability of precast, prestressed construction.

Chapter 2. SELECTION OF REPRESENTATIVE STRUCTURES AND LIMIT STATES OF SEGMENTAL BRIDGES

2.1. Segmental Bridge Statistics

According to the American Segmental Bridge Institute (ASBI 2024), there are over 450 segmental bridges in the United States (Figure 2-1). These bridges are distributed across various states. A statistical analysis of segmental bridges was performed using data from the National Bridge Inventory (NBI) database (FHWA 2024), which includes information on 399 bridges across 43 states. The distribution of bridges by state is illustrated in Figure 2-2. Notably, approximately 50% of these bridges are concentrated in three states: Florida, Massachusetts, and Texas (Popok et al. 2024) . Popok et al. (2024) reported the results of project NCHRP 12-123, completion of which led to the development of the guideline document for the load rating of segmental bridges.

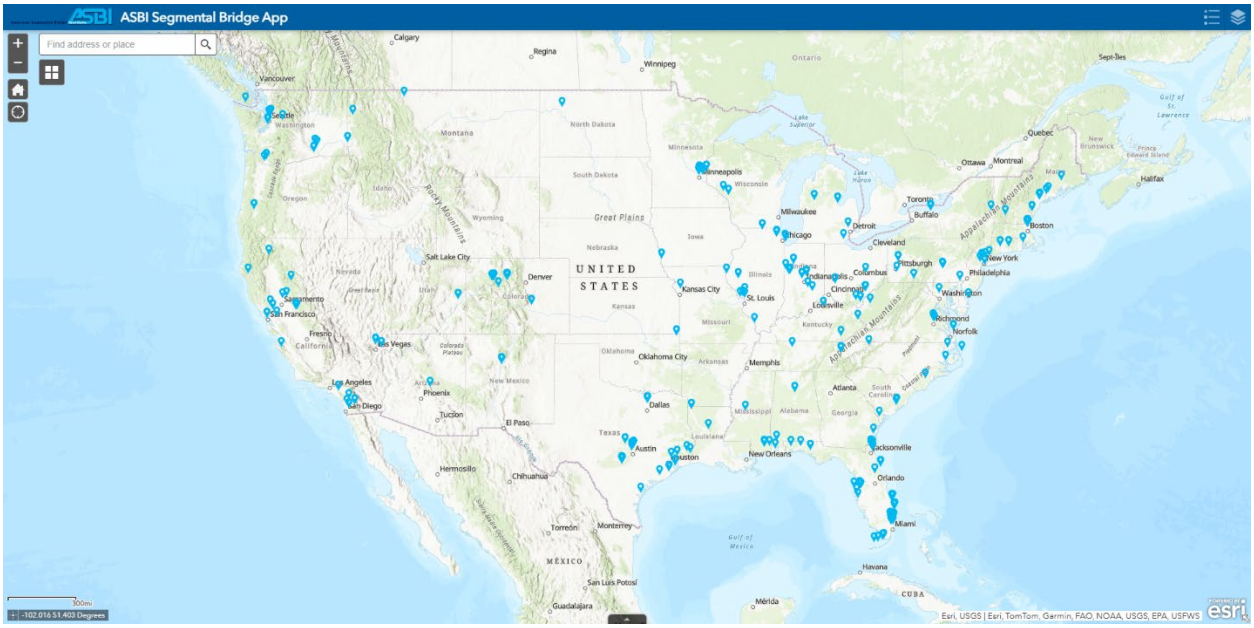

Figure 2-1 Map of Segmental Bridges in the United States (ASBI 2024)

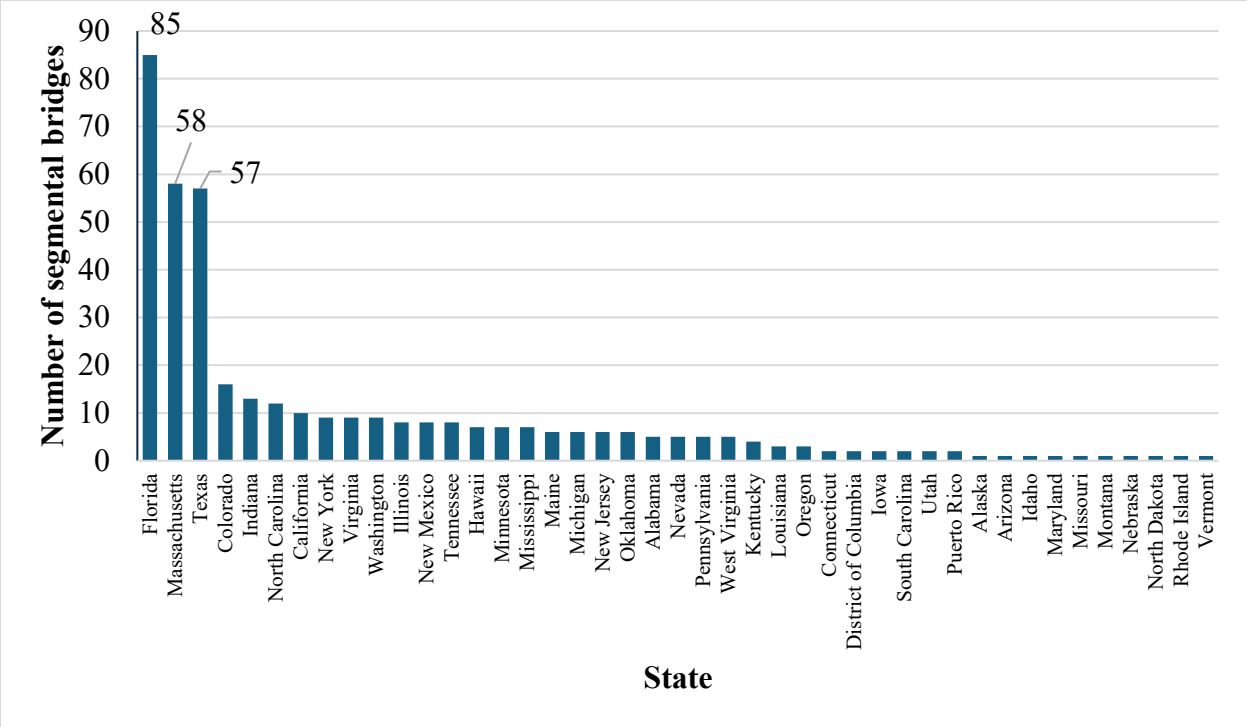

Figure 2-2 Distribution of Segmental Bridges by State (Based on Data Taken from FHWA (2024))

The following figures illustrate the distributions of segmental bridges based on various criteria as indicated in NBI. Figure 2-3 presents the distribution by type of main structure and number of lanes. It is evident that continuous prestressed concrete bridges predominate, and the majority of the bridges feature two lanes.

The data for Figure 2-4 was considered for segmental bridges in the following selected states: Florida, Massachusetts, Texas, Colorado, California, Alabama, Michigan, and Minnesota. These states were chosen based on the number of segmental bridges and the availability of data for analysis. The statistical data for all segmental bridges in these states is presented for various parameters, including bridge age, maximum span length, total length, number of approaching spans, number of lanes, Average Daily Truck Traffic (ADTT) per lane, superstructure rating, and

rating method. Figure 2-4 illustrates the distributions of these parameters, along with the percentage representation of each group for all segmental bridges (Popok et al. 2024).

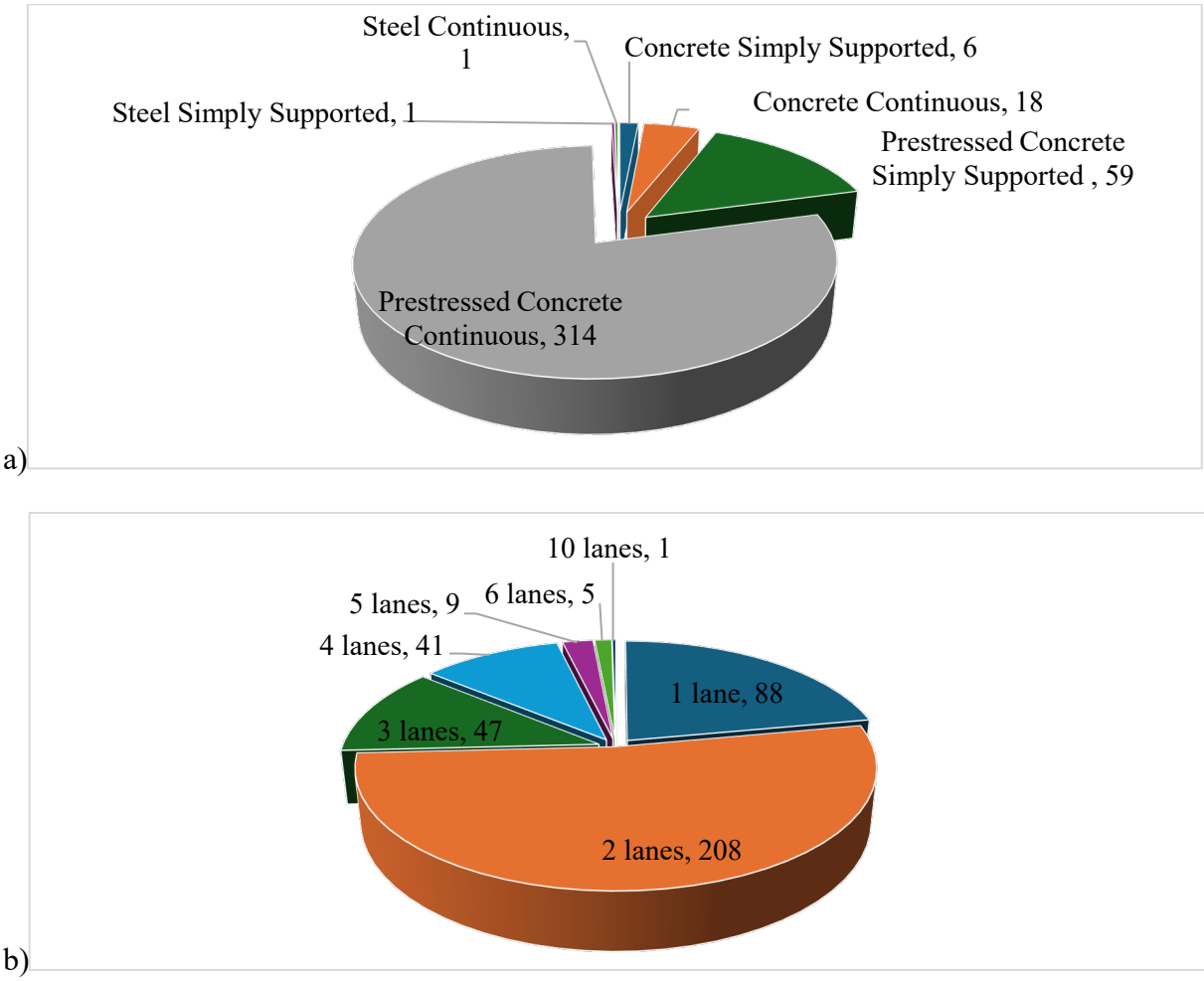

Figure 2-3 Distribution of Segmental Bridges (Based on Data Taken from NBI) by a) Type of the Main Structure, and b) Number of Lanes

Figure 2-5 illustrates the distribution of segmental bridges based on their condition ratings. It indicates that the majority of bridge superstructures are in good condition, as are the majority of bridge decks. Overall, the majority of segmental bridges are rated as being in good condition.

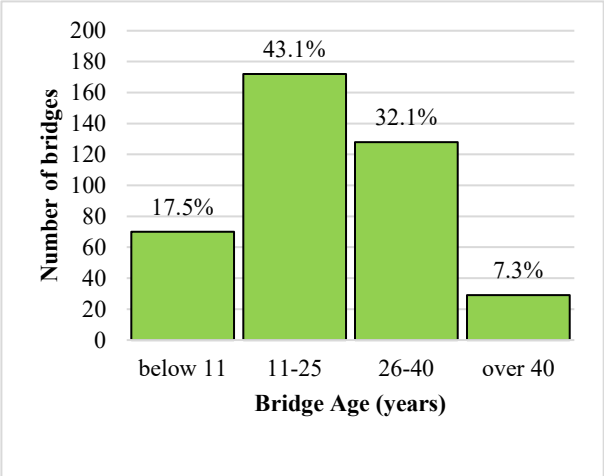
Number of bridges
200
180
160
140
120
100
80
60
40
20
0
17.5%
43.1%
32.1%
7.3%
below 11
11-25
26-40
over 40
Bridge Age (years)

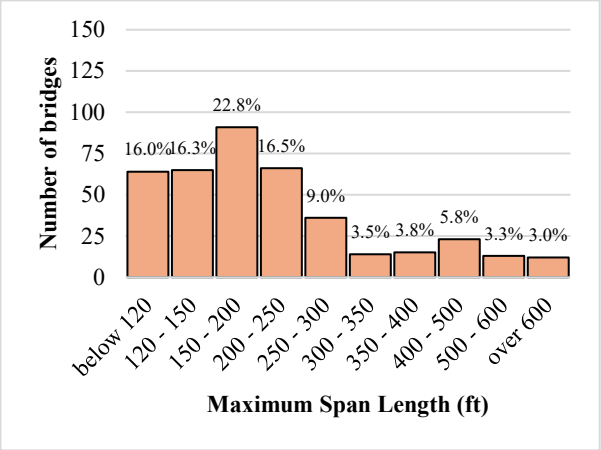
Number of bridges
150
125
100
75
50
25
0
16.0%
16.3%
22.8%
16.5%
9.0%
3.5%
3.8%
5.8%
3.3%
3.0%
below 120
120 - 150
150 - 200
200 - 250
250 - 300
300 - 350
350 - 400
400 - 500
500 - 600
over 600
Maximum Span Length (ft)

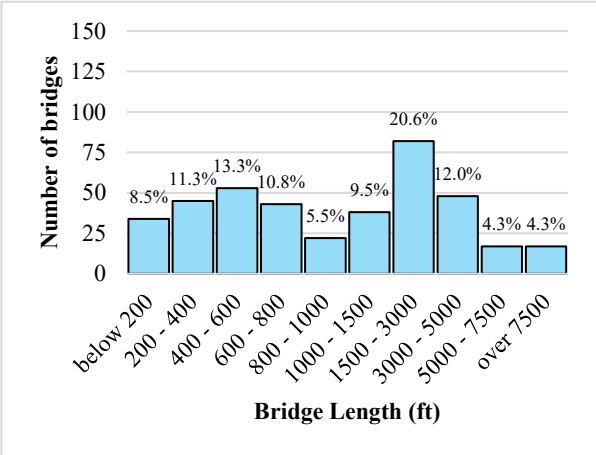
Number of bridges
150
125
100
75
50
25
0
8.5%
11.3%
13.3%
10.8%
5.5%
9.5%
20.6%
12.0%
4.3%
4.3%
below 200
200 - 400
400 - 600
600 - 800
800 - 1000
1000 - 1500
1500 - 3000
3000 - 5000
5000 - 7500
over 7500
Bridge Length (ft)

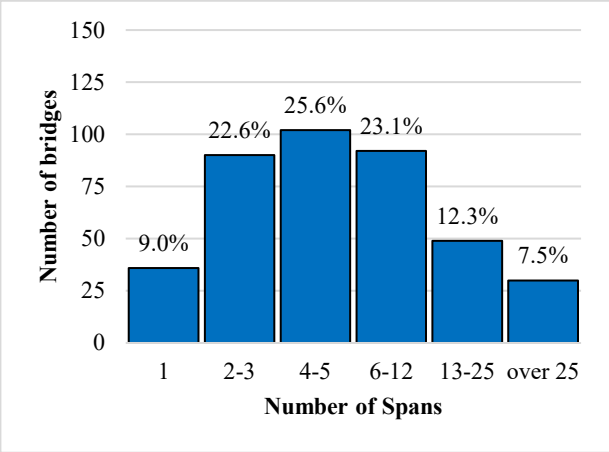
Number of bridges
150
125
100
75
50
25
0
9.0%
22.6%
25.6%
23.1%
12.3%
7.5%
1
2-3
4-5
6-12
13-25
over 25
Number of Spans

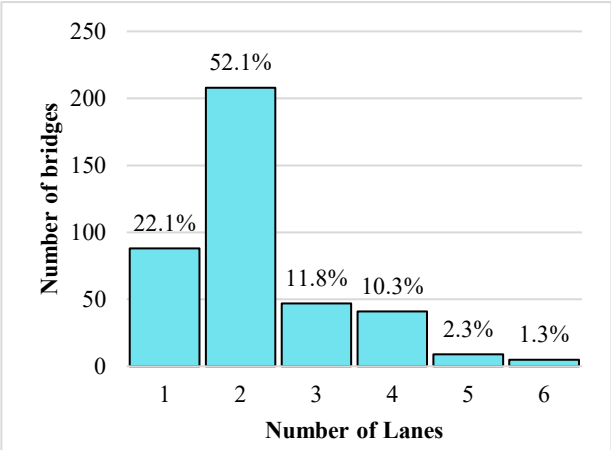
Number of bridges
250
200
150
100
50
0
22.1%
52.1%
11.8%
10.3%
2.3%
1.3%
1
2
3
4
5
6
Number of Lanes

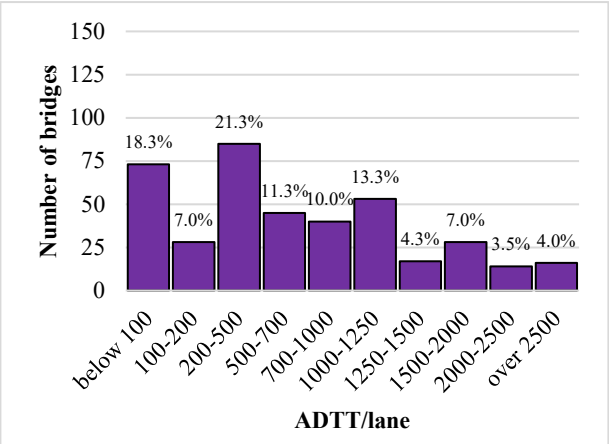
Number of bridges
150
125
100
75
50
25
0
18.3%
7.0%
21.3%
11.3%
10.0%
13.3%
4.3%
7.0%
3.5%
4.0%
below 100
100-200
200-500
500-700
700-1000
1000-1250
1250-1500
1500-2000
2000-2500
over 2500
ADTT/lane

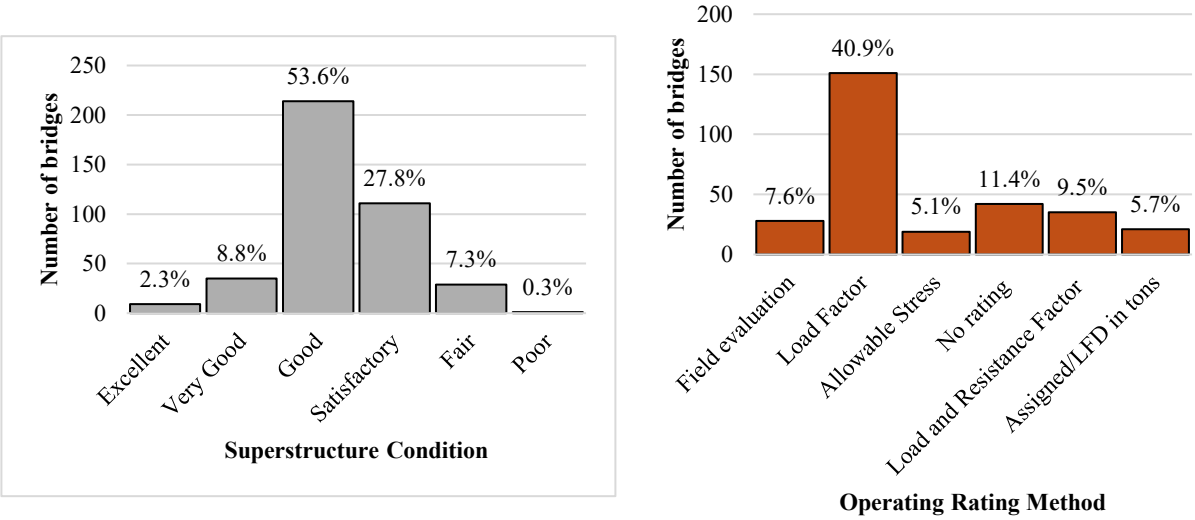

Figure 2-4 Comparison of Selected Segmental Bridges to All Segmental Bridges for Selected States (Based on Data Taken from NBI)

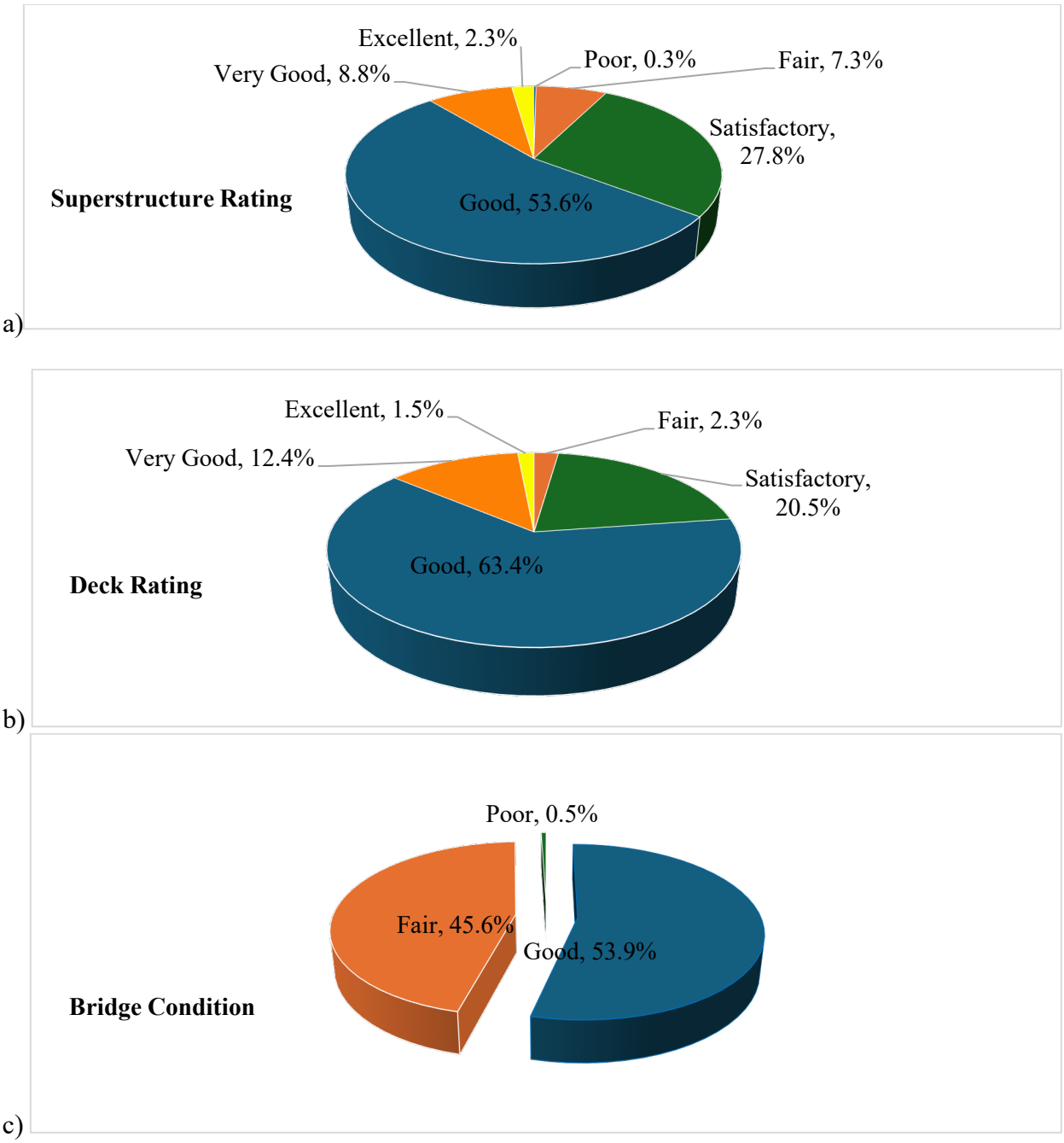

Figure 2-5 Condition Rating Statistics of Segmental Bridges (Based on Data Taken from NBI):

a) Superstructure Rating, b) Deck Rating, c) Bridge Condition

2.2. Selection of Representative Structures

The aim of this task was to choose a set of segmental bridges for inclusion in this study. The chosen set exemplifies the common segmental bridges found in real-world applications.

The bridge structures selected for analysis are representative based on various parameters, including geographic location (specific states), age, maximum span length, total length, width, curvature, material type, rating method, design live load model, traffic volume (measured by ADTT), and overall condition. These selection criteria were established based on the availability of public domain data. Additionally, the selection process was informed by bridge parameter data available in the literature, such as finite element modeling (FEM) software (Midas Civil) tutorials that provide idealized versions of actual bridges, and data from sources like the Corven Engineering, Inc. company and state Departments of Transportation (DOTs).

Based on the above-mentioned selection criteria and the available data, representative segmental bridge structures were selected as shown in Table 2-1.

The Midas Civil tutorials (MIDAS 2021a; 2021b; 2021c) provide data from three examples (idealized versions of actual existing bridges) that represent the primary construction methods: span-by-span, balanced cantilever, and incremental launching. These example bridges were also included in the analysis. The elevation and cross-sectional views of these bridges are illustrated in Figure 2-6 through Figure 2-8.

Table 2-1 Representative Structures

State	Bridge ID	Year built	Material	Max span length [ft]	Total span length [ft]	Number of spans in main unit	Deck Width [ft]	Number of lanes	Erection Type	ADTT per lane	Rating Method	Superstructure Condition
Florida	890150	2006	P/C Cont.	152	4,661	31	61	2	Span-by-Span	455	LRFR	Good
	150189	1986	P/C Cont.	1,200	21,877	11	95	4	Span-by-Span	1,078	LRFR	Good
	580174	1999	P/C Cont.	225	18,425	131	43	2	Span-by-Span	595	LRFR	Fair
North Carolina	5140182P	1983	P/C Cont.	508	1,249	8	45	2	Progressive Cantilever	718	LRFR	Good
Tennessee	5460214P	2013	P/C Cont.	180	790	5	38	2	Balanced Cantilever	340	AS	Good
Colorado	F-07-AL	1986	P/C Cont.	132	613	5	38	2	Span-by-Span	553	LF	Good

The characteristics of all bridge structures utilized in the reliability analysis, including partial structures, are presented in Table 2-2. This selection includes bridges from various states, spanning different ages and employing diverse construction and erection methods. For the Garcon Point Bridge, two structures were considered: the main unit, constructed using the balanced cantilever method, and the typical unit, constructed using the span-by-span method. Consequently, the representative bridge database comprises ten bridge structures in total.

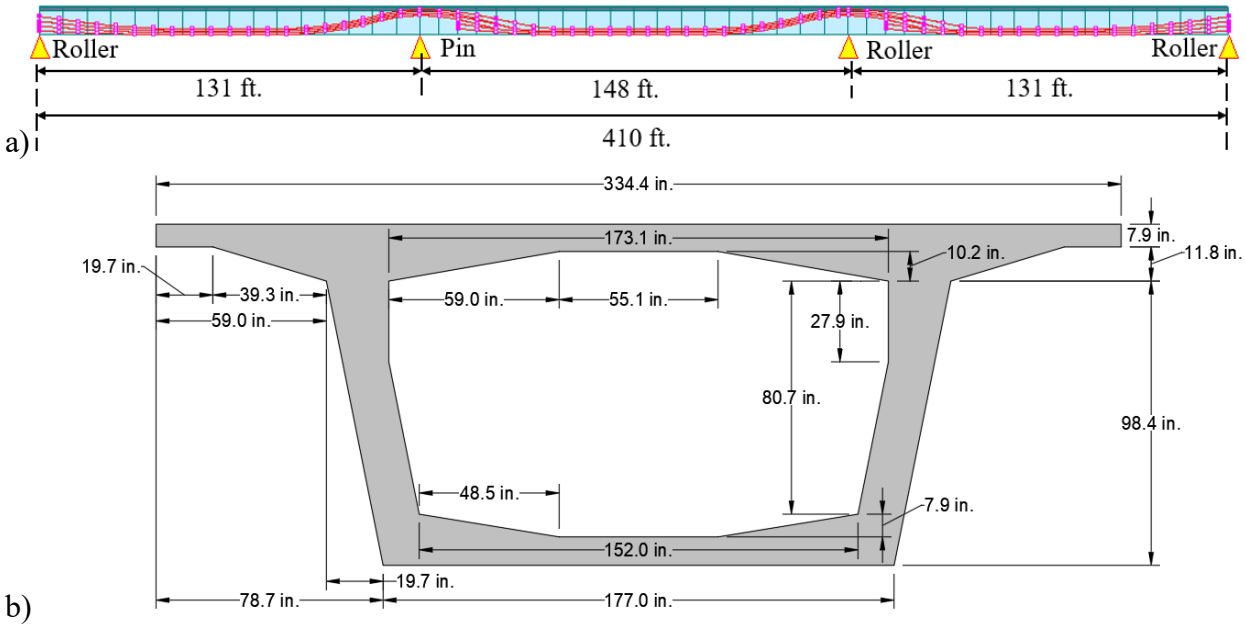

Figure 2-6 a) Elevation and b) Cross-Sectional Views of the Concrete Segmental Bridge Constructed with the Span-By-Span Method (Popok et al. 2024)

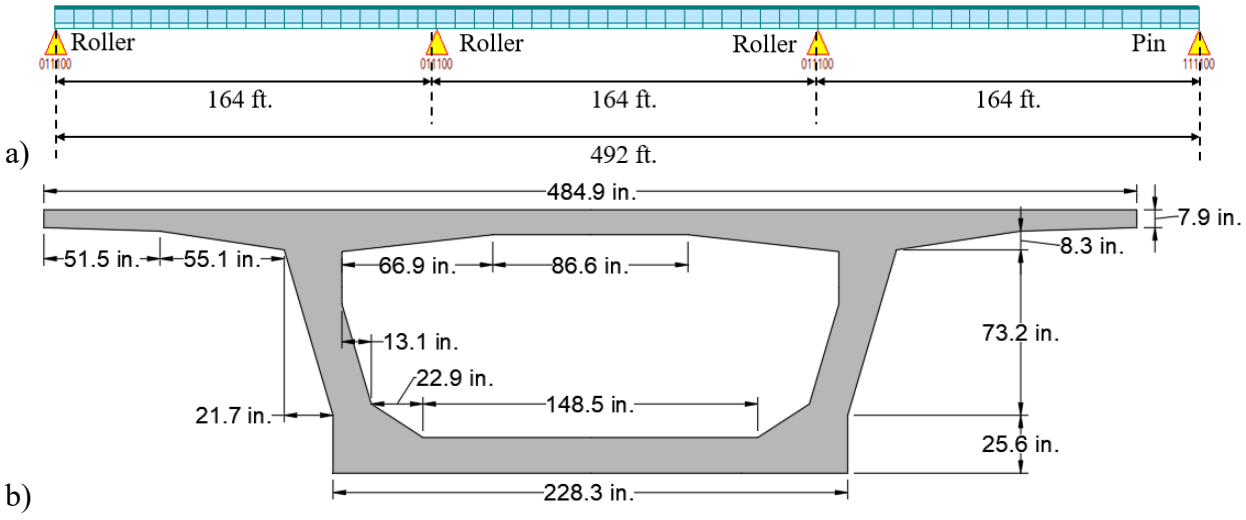

Figure 2-7 a) Elevation and b) Cross-Sectional Views of the Concrete Segmental Bridge Constructed with the Incremental Launching Method (Popok et al. 2024)

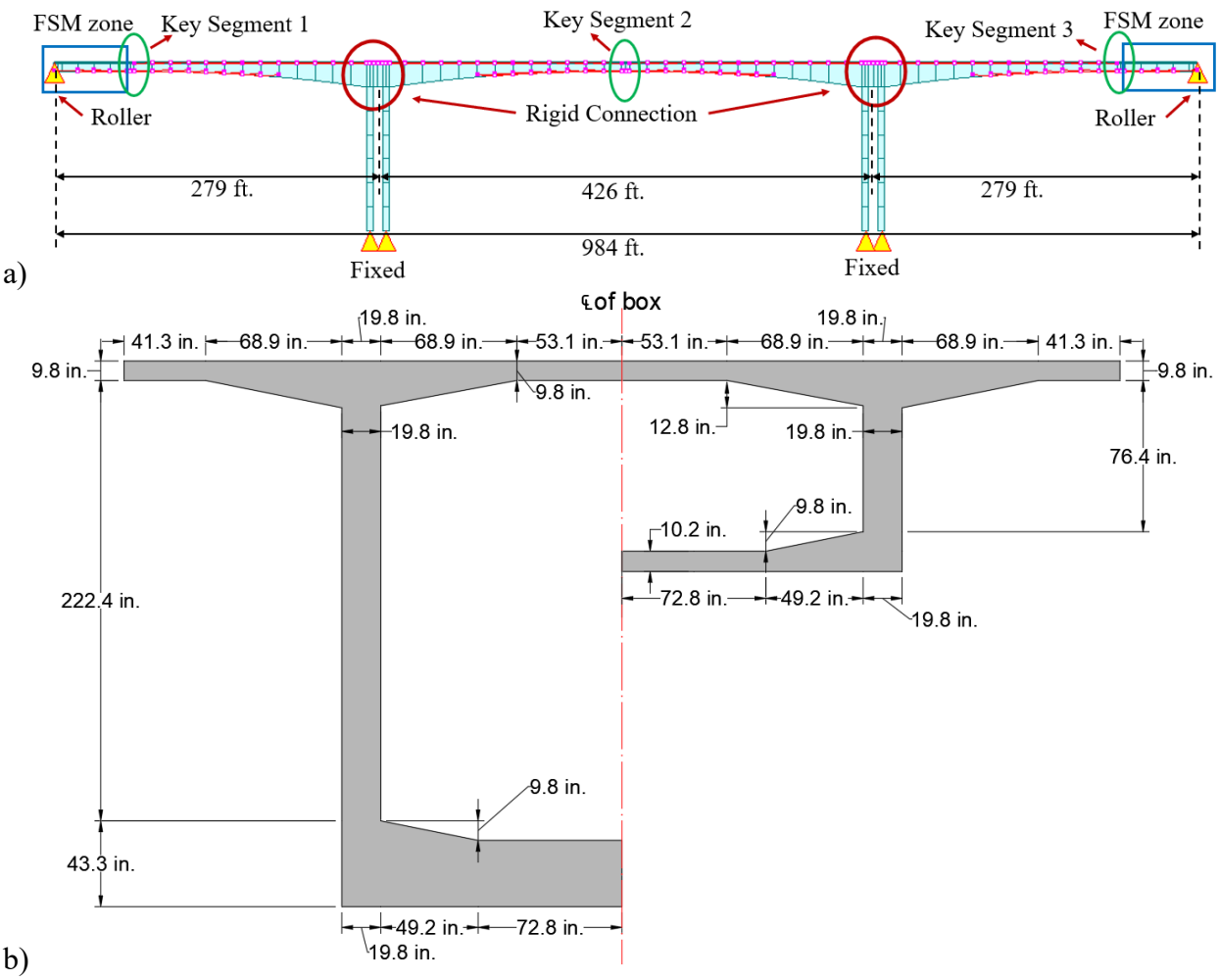

Figure 2-8 a) Elevation and b) Cross-Sectional Views of the Concrete Segmental Bridge Constructed by Balanced Cantilever Method (Popok et al. 2024)

Table 2-2 Characteristics of the Selected Bridges

Name/ Designation	**State**	**Bridge ID**	**Year Built**	**Max. Span Length** [ft]	**No. of Spans**	**Deck Width** [ft]	**Construction/ Erection Method**
Midas Example 1	N/A	N/A	N/A	148	3	27.9	Span-by-Span
Midas Example 2	N/A	N/A	N/A	426	3	42	Balanced Cantilever
Midas Example 3	N/A	N/A	N/A	164	3	40.4	Incremental Launching
N/A	Colorado	F-07-AL	1986	132	5	38	Span-by-Span
Foothills Bridge	Tennessee	5460214P	2013	180	5	36.8	Balanced Cantilever
Ernest Lyons Bridge	Florida	890150	2006	152	6	33	Span-by-Span
Garcon Point Bridge	Florida	580174	1999	225	8	43.1	Balanced Cantilever/Span-by-Span
Sunshine Skyway Bridge	Florida	150189	1986	135	6	42.75	Span-by-Span
Linn Cove Viaduct	North Carolina	5140182P	1983	180	8	34.3	Progressive Cantilever

2.3. Limit States for Segmental Bridges

2.3.1. Selection of Limit States

As a result of a comprehensive review of limit states pertinent to segmental bridges, and incorporating insights from segmental bridge experts, including those affiliated with ASBI and state transportation agencies, appropriate limit states were identified for the analysis for both service and strength levels. The selected limit states are as follows:

- Service limit states:
    - flexural tensile stress,

- principal tensile stress (combined flexural, shear, and torsional effects).

- Strength limit state:
  - flexural strength,
  - shear strength (from combined direct shear and torsion)

Joint behavior must be taken into account. Therefore, these limit states were evaluated at each joint.

2.3.2. Formulation of Limit State Functions

As outlined in Section 1.4.1.2, the limit state function is defined by Equation (1-2), which is:

$$g = R - Q = 0$$

The concept of R and Q as nominal values of resistance and load, respectively, and Q as a sum of load effects, was also introduced in Section 1.4.1.2. It is crucial to note that the resistance capacities and load effects considered in a limit state function vary and are specific to the limit states under consideration. Specifically, for service limit states, the load effects are flexural and shear stresses, while for strength limit states, they are bending moments and shear forces. As outlined in Section 1.4.2.2, the resistance for service limit states is defined as the allowable stress. The resistance for strength limit states is defined as the nominal bending moment strength, M_n, and shear force strength, V_n.

The limit state functions for each limit state considered in this study are further delineated. The load effects for each limit state are incorporated in accordance with AASHTO LRFD (2020).

- *Service Flexural Tensile Stress*

The components of the limit state function for this limit state are normal stresses, and the limit state function is defined as follows:

$$f_R - (f_{DC} + f_{DW} + f_{PS} + f_{CRSH} + f_{TU} + f_{TG} + f_{LL}) = 0 \quad (2\text{-}1)$$

The load effects in this equation are normal stresses due to the specified load components, which are defined as:

$$f = \frac{F}{A} + \frac{My}{I} \quad (2\text{-}2)$$

where F is an axial force acting at the cross section, A is a cross-sectional area, M is a bending moment acting at the cross section, y is a distance from the neutral axis of the cross section to the location where the normal stress is being determined, and I is a moment of inertia of the cross-sectional area about the neutral axis.

- *Service Principal Tensile Stress*

The components of the limit state function for this limit state are shear stresses, and the limit state function is defined as follows:

$$v_R - (v_{DC} + v_{DW} + v_{PS} + v_{CRSH} + v_{TU} + v_{LL}) = 0 \quad (2\text{-}3)$$

The load effects in this equation are shear stresses due to the specified load components due to the transverse shear force, v_v, combined with shear from torsion in the web, v_t, which are defined as:

$$v = v_v + v_t \quad (2\text{-}4)$$

$$v_v = \frac{VQ_y}{It_w} \quad (2\text{-}5)$$

$$v_t = \frac{T}{2A_0 \cdot 0.5t_w} \tag{2-6}$$

where V is a shear force acting at the cross section, Q_y is a first moment of area of section above the centroidal axis, t_w is a total web width perpendicular to median slope of web, at centroidal axis, T is a torque acting at the cross section, and A_0 is a torsional area (total area enclosed by the median line of the exterior webs and slabs of the box section).

The allowable shear stress, v_R, is the shear stress corresponding to the allowable principal tensile stress, $f_{1,R}$, as illustrated on the Mohr's circle with radius R_R in Figure 2-9. To express these relationships mathematically, v_R can be determined using the following equations:

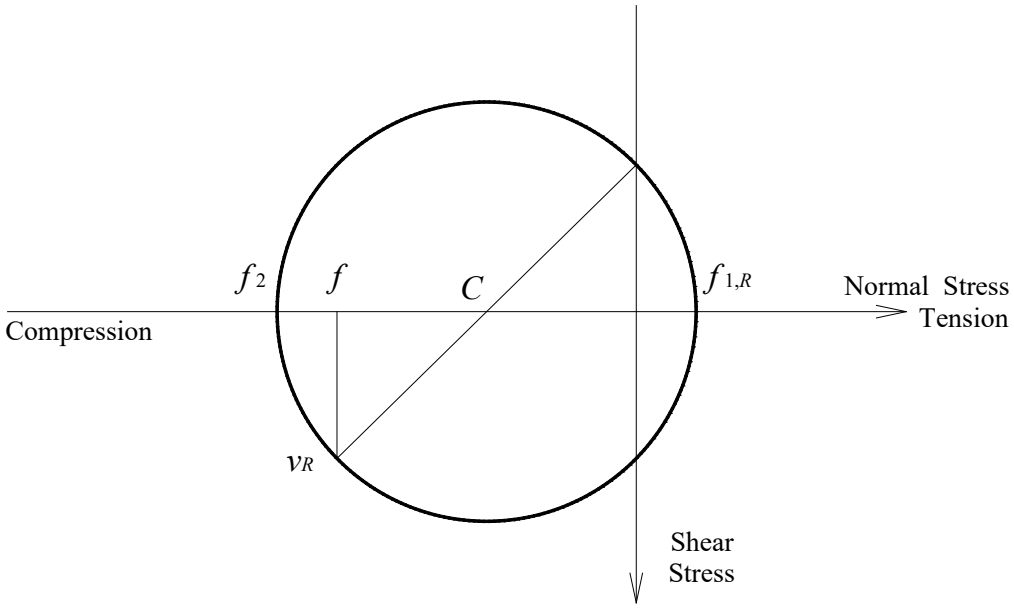

Figure 2-9 Mohr's Circle for Allowable Principal Tensile and Shear Stresses

$$R_R = f_{1,R} - \frac{f}{2} \tag{2-7}$$

$$v_R = \sqrt{R_R^2 - \left(\frac{f}{2}\right)^2} \tag{2-8}$$

where f is the normal stress due to prestressing.

- *Flexural Strength*

The components of the limit state function for this limit state are bending moments and capacity, and the limit state function is defined as follows:

$$M_n - (M_{DC} + M_{DW} + M_{PS} + M_{CRSH} + M_{LL}) = 0 \quad (2\text{-}9)$$

The load effects in this equation are bending moments due to the specified load components.

- *Shear Strength*

The components of the limit state function for this limit state are shear forces and capacity, and the limit state function is defined as follows:

$$V_n - (V_{DC} + V_{DW} + V_{PS} + V_{CRSH} + V_{LL}) = 0 \quad (2\text{-}10)$$

The load effects in this equation are shear forces due to the specified load components.

The variations in load components across different limit states are predominantly attributed to the prestressing force component and temperature effects. In service limit states, the stresses induced by the primary prestressing force should be considered, as they contribute to the structural capacity. Conversely, for strength limit states, the primary prestressing force is integrated into the capacity, necessitating the inclusion of only the secondary prestressing force effects. These secondary effects pertain to the additional stresses and deformations induced in continuous bridges due to the restraining influence at intermediate supports and should be accounted for on the load side (Grouni and Nowak 1984; Nowak and Grouni 1983). Additionally, temperature effects are only applicable to the service limit states. Specifically, temperature gradients are relevant only to the service flexure limit state (AASHTO LRFD 2020, Corven Engineering 2004).

3. RELIABILITY ANALYSIS PROCEDURE

3.1. Determining the Reliability Index

For selected representative segmental bridges, the nominal load components for each bridge and limit state can be determined through finite-element modeling. Similarly, the nominal resistance values can also be established. The means and standard deviations of both loads and resistance can be calculated using the statistical parameters selected and developed as discussed in the next chapters. Consequently, with these statistical parameters, the reliability indices can be computed. These reliability indices can then be categorized by different limit states and presented in tabular form. Assuming that *R* (resistance) and *Q* (load) are independent variables, and that the sum of the load components and the resistance both follow a normal distribution, the reliability index can be calculated as follows (Cornell 1969):

$$\beta = \frac{m_R - m_Q}{\sqrt{\sigma_R^2 + \sigma_Q^2}} \tag{3-1}$$

where μ_R and μ_Q represent the mean values of the resistance and load components, respectively, and σ_R and σ_Q denote their standard deviations.

3.2. Reliability Index Calculation for Considered Limit States

Considering the various components of the limit state function for the different limit states and the load components integrated within each function, Equation (3-1) can be expanded for each specified limit state taking into account corresponding limit state functions (Section 2.1.2). This expansion is discussed further in the subsequent discussion.

- *Service Flexural Tensile Stress*

The elements of the limit state function for this limit state involve normal flexural stresses, and the reliability index is determined as follows:

$$\beta = \frac{\mu_{fR} - \mu_{fDC} - \mu_{fDW} - \mu_{fPS} - \mu_{fCRSH} - \mu_{fTU} - \mu_{fTG} - \mu_{fLL}}{\sqrt{\sigma_{fR}^2 + \sigma_{fDC}^2 + \sigma_{fDW}^2 + \sigma_{fPS}^2 + \sigma_{fCRSH}^2 + \sigma_{fTU}^2 + \sigma_{fTG}^2 + \sigma_{fLL}^2}} \quad (3\text{-}2)$$

- *Service Principal Tensile Stress*

The elements of the limit state function for this limit state involve shear stresses, and the reliability index is calculated as follows:

$$\beta = \frac{\mu_{vR} - \mu_{vDC} - \mu_{vDW} - \mu_{vPS} - \mu_{vCRSH} - \mu_{vTU} - \mu_{vLL}}{\sqrt{\sigma_{vR}^2 + \sigma_{vDC}^2 + \sigma_{vDW}^2 + \sigma_{vPS}^2 + \sigma_{vCRSH}^2 + \sigma_{vTU}^2 + \sigma_{vLL}^2}} \quad (3\text{-}3)$$

- *Flexural Strength*

The elements of the limit state function for this limit state involve bending moments and capacity, and the reliability index is determined as follows:

$$\beta = \frac{\mu_{Mn} - \mu_{MDC} - \mu_{MDW} - \mu_{MPS} - \mu_{MCRSH} - \mu_{MLL}}{\sqrt{\sigma_{Mn}^2 + \sigma_{MDC}^2 + \sigma_{MDW}^2 + \sigma_{MPS}^2 + \sigma_{MCRSH}^2 + \sigma_{MLL}^2}} \quad (3\text{-}4)$$

- *Shear Strength*

The elements of the limit state function for this limit state involve shear forces and capacity, and the reliability index is calculated as follows:

$$\beta = \frac{\mu_{Vn} - \mu_{VDC} - \mu_{VDW} - \mu_{VPS} - \mu_{VCRSH} - \mu_{VLL}}{\sqrt{\sigma_{Vn}^2 + \sigma_{VDC}^2 + \sigma_{VDW}^2 + \sigma_{VPS}^2 + \sigma_{VCRSH}^2 + \sigma_{VLL}^2}} \quad (3\text{-}5)$$

3.3. Resistance Models for Strength Limit States

Particular emphasis should be placed on determining the statistical parameters for resistance in strength limit states. The resistance of a structural component for these limit states, R, is treated as a random variable with different types of uncertainty. It is useful to express R as the product of the nominal value R_n and three factors, as illustrated in equation

$$R = R_n MFP \tag{3-6}$$

where R_n is the nominal (design) resistance value, M is the materials factor representing material properties, F is the fabrication factor representing the component's dimensions and geometry, and P is the professional factor representing the approximations in structural analysis and idealized mathematical models for predicting load-carrying capacity.

The statistical parameters for M, F, and P are explored in Chapter 5. In this study, cumulative distribution functions for the structural types considered were generated using the Monte Carlo technique, as described further in Section 3.3.3. The mean values of resistance (μ) and standard deviation (σ) were determined, and the bias factor (λ) and coefficient of variation (COV) were calculated for bridges from the selected representative segmental bridge database. For the purposes of reliability analysis, variables are typically expressed in terms of the bias factor (λ) and the coefficient of variation (COV) of normal distributions. In this dissertation, the bias factor (λ) denotes the ratio of the mean value to the nominal value, while the coefficient of variation (COV) represents the ratio of the standard deviation to the mean value (Equation (3-7)). The coefficient of variation (COV) quantifies the relative dispersion of the data. Subscripts are added to these statistical parameters to indicate the specific variable they pertain to. For instance, λ_R and COV_R refer to the parameters for the resistance of structural components (R).

$$\lambda_x = \frac{mean}{nominal} = \frac{\mu_x}{X} \tag{3-7}$$

$$COV_x = \frac{\sigma_x}{\mu_x}$$

3.3.1. Flexural Strength Provisions

In accordance with the AASHTO LRFD (2020) Article 5.6.3.2.2, the nominal flexural strength for flanged sections, M_n, reasonably assuming the neutral axis is in the flange, can be estimated as follows:

$$M_n = A_{ps} f_{ps} \left(d_p - \frac{a}{2}\right) + A_s f_s \left(d_s - \frac{a}{2}\right) - A'_s f'_s \left(d'_s - \frac{a}{2}\right) \tag{3-8}$$

in which

$$a = c\beta_1 \tag{3-9}$$

$$\beta_1 = \begin{array}{ll} 0.85 & if\ f'_c \le 4\ ksi \\ 0.85 - 0.05(f'_c - 4) & if\ 4\ ksi < f'_c < 8\ ksi \\ 0.65 & if\ f'_c \ge 8\ ksi \end{array} \tag{3-10}$$

where:

A_{ps} = area of prestressing steel

f_{ps} = average stress in prestressing steel at nominal bending resistance

d_p = distance from extreme compression fiber to the centroid of prestressing tendons

A_s = area of nonprestressed tension reinforcement

f_s = stress in the nonprestressed tension reinforcement at nominal flexural resistance

d_s = distance from extreme compression fiber to the centroid of nonprestressed tensile reinforcement

A'_s = area of compression reinforcement

f'_s = stress in the nonprestressed compression reinforcement at nominal flexural resistance

d'_s = distance from extreme compression fiber to the centroid of compression reinforcement

c = distance from the extreme compression fiber to the neutral axis

β_1 = stress block factor

f'_c = specified concrete compressive strength.

Equation (3-8) specifically applies to the typical scenario for the segmental bridge cross sections where the compressive stress block maintains a constant width throughout its depth. Since prestressing steel lacks a clearly defined yield point or plateau, design calculations for f_{ps} are approximate. A design value for f_{ps} can be determined through a strain compatibility analysis and an assumed stress-strain relationship for the prestressing reinforcement. Alternatively, under common conditions, the design value for f_{ps} for components with bonded prestressing tendons, applicable to the selected representative bridges, can be calculated using the approximate expression provided in AASHTO LRFD (2020) Article 5.6.3.1.1:

$$f_{ps} = f_{pu}\left(1 - k\frac{c}{d_p}\right) \tag{3-11}$$

in which

$$k = 2\left(1.04 - \frac{f_{py}}{f_{pu}}\right) \tag{3-12}$$

For low relaxation strand, $k = 0.28$.

$$c = \frac{A_{ps}f_{pu}}{0.85f'_c\beta_1 b + kA_{ps}\frac{f_{pu}}{d_p}} \tag{3-13}$$

where:

f_{pu} = specified tensile strength of prestressing steel

f_{py} = yield strength of prestressing steel

b = width of the compression face of the member. For a flange section in compression, the effective width of the flange.

For the representative bridges in this study, nonprestressed reinforcement is typically not used for flexural strength. Therefore, Equation (3-8) can be simplified as follows:

$$M_n = A_{ps} f_{ps} \left(d_p - \frac{a}{2} \right) \tag{3-14}$$

3.3.2. Shear Strength Provisions

In regions where it is reasonable to assume that plane sections remain plane after loading, components may be designed for shear according to AASHTO LRFD (2020) Article 5.7.3.3. The nominal shear strength, V_n, can be estimated as follows:

$$V_n = V_c + V_s + V_p \leq 0.25 f_c' b_v d_v \tag{3-15}$$

in which

$$V_c = 0.0316 \beta \lambda \sqrt{f_c'} b_v d_v \tag{3-16}$$

$$V_s = \frac{A_v f_y d_v (\cot\theta + \cot\alpha) \sin\alpha}{s} \lambda_{duct} \tag{3-17}$$

$$\lambda_{duct} = 1 - \delta \left(\frac{\phi_{duct}}{b_w} \right)^2 \tag{3-18}$$

where:

V_p = component of prestressing force in the direction of the shear force; positive if resisting the applied shear

b_v = effective web width taken as the minimum web width within the depth d_v

d_v = effective shear depth

β = factor indicating ability of diagonally cracked concrete to transmit tension and shear

λ = concrete density modification factor

A_v = area of transverse reinforcement within a distance s

f_y = yield strength of the nonprestressed reinforcement

θ = angle of inclination of diagonal compressive stresses

α = angle of inclination of transverse reinforcement to longitudinal axis

s = spacing of transverse reinforcement measured in a direction parallel to the longitudinal reinforcement

λ_{duct} = shear strength reduction factor accounting for the reduction in the shear resistance provided by transverse reinforcement due to the presence of a grouted post-tensioning duct. Taken as 1.0 for ungrouted post-tensioning ducts and with a reduced web or flange width to account for the presence of ungrouted duct

δ = duct diameter correction factor, taken as 2.0 for grouted ducts

ϕ_{duct} = diameter of post-tensioning duct present in the girder web within depth d_v

b_w = gross width of web, not reduced for the presence of post-tensioning ducts.

Instead of following the provisions of Article 5.7.3, segmental post-tensioned concrete box girder bridges can be designed for shear using the guidelines specified in AASHTO LRFD (2020) Article 5.12.5.3.8c. The nominal shear strength, V_n, can be estimated as follows:

$$V_n = V_c + V_s \leq 0.379\lambda\sqrt{f_c'}b_v d \tag{3-19}$$

in which

$$V_c = 0.0632K\lambda\sqrt{f_c'}b_v d \tag{3-20}$$

$$V_s = \frac{A_v f_y d}{s} \tag{3-21}$$

$$K = \sqrt{1 + \frac{f_{pc}}{0.0632\lambda\sqrt{f_c'}}} \leq 2.0 \tag{3-22}$$

where:

d = $0.8h$ or the distance from the extreme compression fiber to the centroid of the prestressing reinforcement, whichever is greater

f_{pc} = unfactored compressive stress in concrete after prestress losses have occurred either at the centroid of the cross section resisting transient loads or at the junction of the web and flange where the centroid lies in the flange.

The shear resistances of the segments in the selected representative bridges in this study are calculated based on the AASHTO LRFD (2020) Article 5.12.5.3.8c alternative shear design procedure for segmental bridges, as it is specifically developed and targeted for segmental bridges.

3.3.3. Statistical Parameters of Resistance by Monte Carlo Simulation

Monte Carlo simulation and linear regression are employed to develop the resistance parameters of the representative segmental bridges by integrating the random variables. The Monte Carlo simulation method numerically simulates outcomes without extensive physical testing. Statistical parameters, with specific probability distributions essential for determining the flexural and shear strength of concrete components, are derived from prior test results and available recommendations. This data is then used to generate numerical samples. Nowak and Collins (2013) provide a detailed explanation of the Monte Carlo technique in reliability analysis. The statistical parameters of resistance are determined by applying linear regression to the resistance statistical distribution.

The algorithm used in this study to determine the statistical parameters for the flexural strength resistance of the representative segmental bridges involves the following steps. The procedure to determine R_n is as described in Section 3.3.1 (Equation (3-7) through Equation (3-9)):

1. Calculate $R_n = A_{ps,n} f_{ps,n} \left(d_{p,n} - \frac{a_n}{2} \right)$ using nominal values.
2. Randomly generate values for each variable required to determine the flexural strength.
3. Compute $R = A_{ps} f_{ps} \left(d_p - \frac{a}{2} \right) P$ using the randomly generated values.
4. Calculate the ratio R/R_n and record the result.
5. Repeat steps 2–4 until a sufficient number of R/R_n values have been simulated. The number of simulations was 1×10^6 in all cases.
6. Plot the cumulative distribution function of R/R_n on a normal probability scale.
7. Fit a straight line to the distribution using linear regression.
8. Determine λ_R and COV_R based on the intercept and slope of the fitted line.

A similar methodology to the one described above was utilized to determine the statistical parameters for the shear strength resistance of the representative segmental bridges. This involved the specific procedure for assessing shear resistance instead as detailed in Section 3.3.2 (Equation (3-18) through Equation (3-21)).

4. DEVELOPMENT OF STATISTICAL MODELS FOR LOADS

4.1. Considered Statistical Parameters and Load Components for Reliability Analysis

The statistical parameters for permanent loads were derived from existing literature. Certain parameters were adjusted using engineering judgment, while others were refined based on the analysis results from a selected representative segmental bridge database, as discussed further.

The load components considered in this study include:

- Dead loads: structural components and nonstructural attachments (*DC*), and wearing surfaces and utilities (*DW*)
- Superimposed deformations: creep (*CR*), shrinkage (*SH*), and temperature effects (uniform temperature, *TU*, and thermal gradient, *TG*)
- Prestressing effects: both primary and secondary (*PS*)
- Live load (*LL*)

The development of statistical models for these loads is elaborated upon in the subsequent sections of this chapter.

4.2. Statistical Models for Dead Loads and Superimposed Deformations

As referenced in Section 1.4.2.1, Nowak (1999) made significant contributions to the calibration of the AASHTO LRFD Bridge Design Specifications. The statistical parameters for dead load were directly adopted from this document and are presented in Table 4-1. For the dead load of the wearing surface (*DW*), the nominal asphalt thickness is assumed to be equal to the mean value, which is 3.5 inches. Consequently, the bias factor is calculated as $\lambda_{DW} = \mu_{DW}/DW_n$ = 3.5 in./3.5 in. = 1.0.

Table 4-1 Statistical Parameters of Dead Load (Nowak 1999)

Component	Bias Factor, λ	Coefficient of Variation (*COV*)
Cast-in-place members (DC)	1.05	0.10
Factory-made members (DC)	1.03	0.08
Asphalt	3.5 in.*	0.25

* Mean thickness

As detailed in Section 1.4.3, it is crucial to account for superimposed deformations such as creep, shrinkage, and temperature effects in the design and load rating of segmental bridges. The statistical parameters for these deformations were derived from the calibration studies of the Ontario Bridge Design Code (Grouni and Nowak 1984; Nowak and Grouni 1983). These studies established the statistical parameters for strain-related effects of creep (*CR*) and shrinkage (*SH*) with λ = 0.90 and *COV* = 0.20, and for temperature effect (*TU*) with λ = 1.00 and *COV* = 0.25. However, current practice observations suggest slightly adjusted values, with λ = 1.00 and *COV* = 0.15 for all three effects (*CR, SH*, and *TU*). These values have been adopted in the present study for these effects.

4.3. Statistical Models for Prestressing Effect

The studies on the Ontario Bridge Design Code (Grouni and Nowak 1984; Nowak and Grouni 1983) indicate that the effect of prestressing force can be considered the result of axial (longitudinal) force, primary moment due to the eccentricity of the prestressing force, and secondary effect of prestressing in continuous girders. The joint effect of these components is characterized by λ (mean-to-nominal) = 1.00 and *COV* = 0.05.

In the present study, an investigation was conducted to evaluate the nominal values of normal stress in concrete at the bottom fiber due to prestressing at the critical midspan sections of selected representative segmental bridges, obtained as a result of finite-element modeling. In

particular, Midas Civil software was utilized due to its specific design for bridge analysis. The Midas Civil tutorials (MIDAS 2021a; 2021b; 2021c) guided specific modeling choices. The software features a built-in database of bridge cross-section types and an automatic mesh generation function with appropriate mesh sizes, which was employed in this study. Time-dependent concrete material models were used, with material properties defined according to the CEB-FIP (1990) design code. Beam elements were used for the structures, and the location and properties of the tendons were specified in a dedicated section. Supports in translational directions were input longitudinally at span separation locations and transversely at two locations to support the segment box. The dead loads were defined as self-weight and superimposed dead load (barriers and asphalt pavement). The temperature load was defined according to AASHTO LRFD (2020) based on the corresponding temperature zone. The live load was defined as HL-93, also per AASHTO LRFD (2020). Construction stages were defined to account for the impact of the sequence of works conducted during construction.

The nominal values of normal stress were compared to the stress values in these sections required by the design according to AASHTO LRFD (2020). The required stress due to prestressing was determined using the design equation for the service flexure limit state. According to the FDOT table (Table 1-3) for allowable stresses in concrete bridges (Corven Engineering 2004), the stress limit for Type A joints without the minimum bonded auxiliary longitudinal reinforcement through the joints, whether internal or external prestressing (e.g., match-cast epoxy joints or unreinforced cast-in-place closures between precast segments or spliced girders), is zero tension ($f_R = 0$). Therefore, the design equation will be as follows:

$$\gamma_{DC}f_{DC} + \gamma_{DW}f_{DW} + \gamma_{PSpr}f_{PSpr} + \gamma_{PSsc}f_{PSsc} + \gamma_{CRSH}f_{CRSH} + \gamma_{TU}f_{TU} + \gamma_{TG}f_{TG} + \gamma_{LL}f_{LL} = 0 \quad (4\text{-}1)$$

According to AASHTO LRFD (2020), all load factors in this equation are 1.0, except for γ_{TG} and γ_{LL}. As detailed in Section 1.4.3.1, AASHTO LRFD (2020) mandates the evaluation of two load combinations involving temperature gradient (TG) and live load (LL) at service limit states: $\gamma_{LL}\ LL + 0.5TG$ and $1.0TG + 0LL$. Consequently, there are two cases of Equation (4-1) to consider, which are as follows:

$$f_{DC} + f_{DW} + f_{PSpr} + f_{PSsc} + f_{CRSH} + f_{TU} + 0.5f_{TG} + 0.8f_{LL} = 0 \quad (4\text{-}2)$$

$$f_{DC} + f_{DW} + f_{PSpr} + f_{PSsc} + f_{CRSH} + f_{TU} + f_{TG} = 0 \quad (4\text{-}3)$$

Both combinations were evaluated to determine the governing (maximum) required stress in concrete due to prestressing. The stress resulting from prestressing can be expressed as follows:

$$f_{PSpr} + f_{PSsc} = -f_{DC} - f_{DW} - f_{CRSH} - f_{TU} - \gamma_{TG}f_{TG} - \gamma_{LL}f_{LL} \quad (4\text{-}4)$$

Both primary and secondary effects in concrete due to prestressing are induced by the same prestressing force; therefore, variations in the amount of prestressing will influence both primary and secondary effects in the concrete. For instance, a reduction in prestressing stress will decrease the primary effect in concrete, which contributes to resistance (an undesirable outcome), but will also reduce the secondary effect, which contributes to the load (a desirable outcome). It is assumed that the ratio between primary and secondary effects in a specific section remains constant as the amount of prestressing changes. Therefore, we assume there is a fixed ratio of f_{PSsc}/f_{PSpr} in a section, and Equation (4-4) can be modified accordingly:

$$f_{PSpr}\left(1 + \frac{f_{PSsc}}{f_{PSpr}}\right) = -f_{DC} - f_{DW} - f_{CRSH} - f_{TU} - \gamma_{TG}f_{TG} - \gamma_{LL}f_{LL} \quad (4\text{-}5)$$

The ratio of f_{PSsc}/f_{PSpr} was determined using the nominal f_{PSsc} and f_{PSpr} values obtained from finite element modeling. Consequently, the required primary prestressing effect in concrete can be determined as follows:

$$f_{PSpr,req} = \frac{-f_{DC} - f_{DW} - f_{CRSH} - f_{TU} - \gamma_{TG} f_{TG} - \gamma_{LL} f_{LL}}{1 + \frac{f_{PSsc}}{f_{PSpr}}} \quad (4\text{-}6)$$

This can be demonstrated with an example of the bridge constructed using the incremental launching method (Midas Example 3, Table 2-2). The nominal primary prestressing stress at the critical midspan section, obtained from finite element modeling, is f_{PSpr} = -1600 psi (compression). The required prestressing was calculated using both combinations:

$$f_{PSpr,req1} = \frac{-860 - 148 - 0.04 - 0 - 0.5 \cdot 45 - 0.8 \cdot 270}{1 + \frac{36}{-1600}} = -1275\ psi$$

$$f_{PSpr,req2} = \frac{-860 - 148 - 0.04 - 0 - 1 \cdot 45}{1 + \frac{36}{-1600}} = -1077\ psi$$

The first combination governs, resulting in a required prestressing stress of $f_{PSpr,req}$ = -1275 psi in this section. This indicates that the section is overdesigned by a factor of -1600/-1275 = 1.25. A similar analysis was conducted for the nine remaining bridge structures in the representative bridge database (Table 2-2), revealing that, on average, the bridges were overdesigned by a factor of 1.25. The minimum overdesign factor for the investigated bridge structures is 1.0, the maximum is 1.6, and the median is 1.22.

This common overdesign of existing bridges provides additional structural reliability, which can be advantageous. Consequently, it was decided to leverage this additional reliability by increasing the bias factor for the prestressing effect (both primary and secondary, although increasing the secondary effect is not beneficial) to a value of λ_{PS} = 1.25.

4.4. Statistical Models for Live Load

4.4.1. Design Live Load

According to AASHTO LRFD (2020), the vehicular live load on bridge roadways or incidental structures, known as HL-93, includes a combination of:

- A design truck or design tandem, and
- A design lane load.

The axle and wheel weights and spacings for the design truck should follow the specifications in Figure 4-1. The design tandem includes two 25.0-kip axles spaced 4.0 feet apart, with a transverse wheel spacing of 6.0 feet. The design lane load is a 0.64 klf load uniformly distributed along the length and assumed to be uniformly distributed over a 10.0-foot width transversely.

For bridge spans of 25 feet or more, the controlling load combination consists of the design truck plus lane loading. To account for dynamic load allowance, *IM*, the static effects of the design truck should be increased by 33% (AASHTO LRFD 2020).

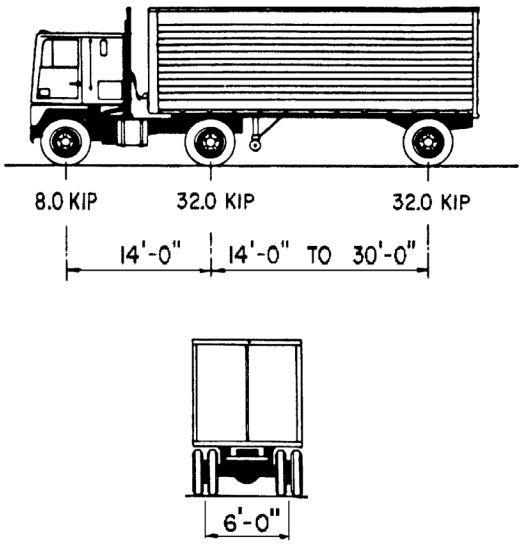

Figure 4-1 Characteristics of the Design Truck (AASHTO LRFD 2020)

4.4.2. Selection of Statistical Parameters

Previous studies have utilized available truck survey and traffic data to develop statistical models for live load. Notably, Nowak (1999) focused on strength limit states, which aim to prevent catastrophic failures that could result in significant damage or loss of life. A 75-year time frame is considered to encompass the entire lifespan of a bridge, ensuring its ability to withstand rare, extreme events (such as heavy traffic loads and natural disasters) that may occur during its service life. Consequently, statistical parameters for the maximum 75-year live load were derived for a range of span lengths up to 200 feet.

Live load effects are evaluated in terms of positive moments, negative moments (for continuous spans), and shear forces. For a single lane, the bias factors for the maximum 75-year live load effects are illustrated in Figure 4-2 for simple span moments, negative moments, and shear. The analysis of two-lane (or multilane) loading considers the simultaneous presence and distribution of truck loads to girders. For two-lane bridges, the bias factor for LRFD load per girder, λ_g, is shown in Figure 4-3. The coefficient of variation, *COV*, is 0.11 for spans over 30 feet and 0.14 for a 10-foot span (Nowak 1999).

The serviceability limit states necessitated the development of additional statistical parameters, encompassing not only maximum values but more frequencies of live load occurrence. Therefore, these maximum values were required for shorter time periods, such as a day, week, month, or year. Wassef et al. (2014) conducted a comprehensive study to derive statistical models for live load. They had access to a substantial amount of weigh-in-motion (WIM) truck data from two sources: NCHRP Project 12-76 (NCHRP Report 683) (Sivakumar, Ghosn, and Moses 2011) and FHWA files. Their analysis included the WIM database from NCHRP 12-76 and FHWA, comprising data from over 65 million vehicles. After filtering to remove errors, exclude skewed

heavy vehicle data from New York, and omit incompatible data from Indiana, they obtained a reliable dataset of approximately 35 million vehicles.

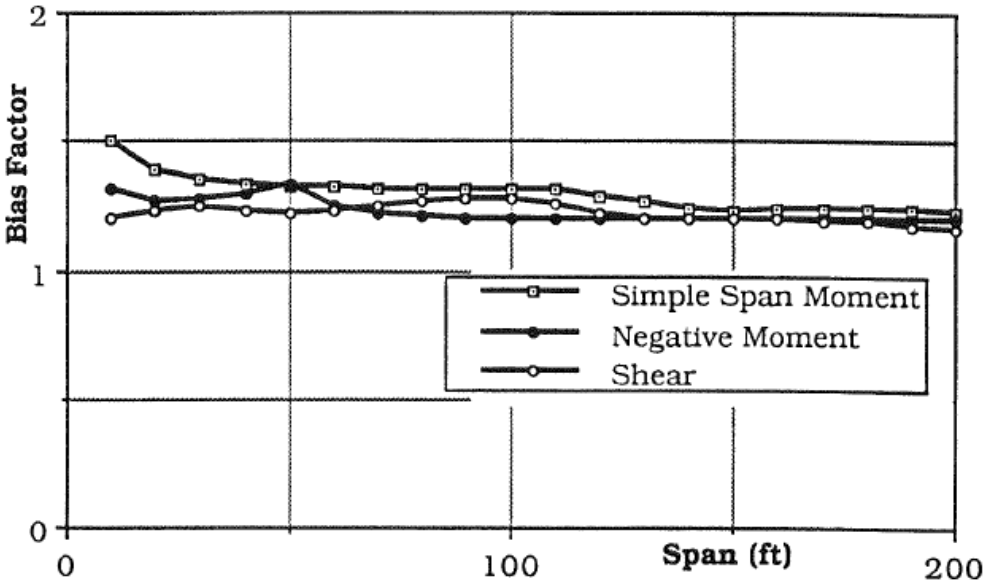

Figure 4-2 Bias Factor for the Maximum 75 Year Live Load Effects per Lane, LRFD Code (Nowak 1999)

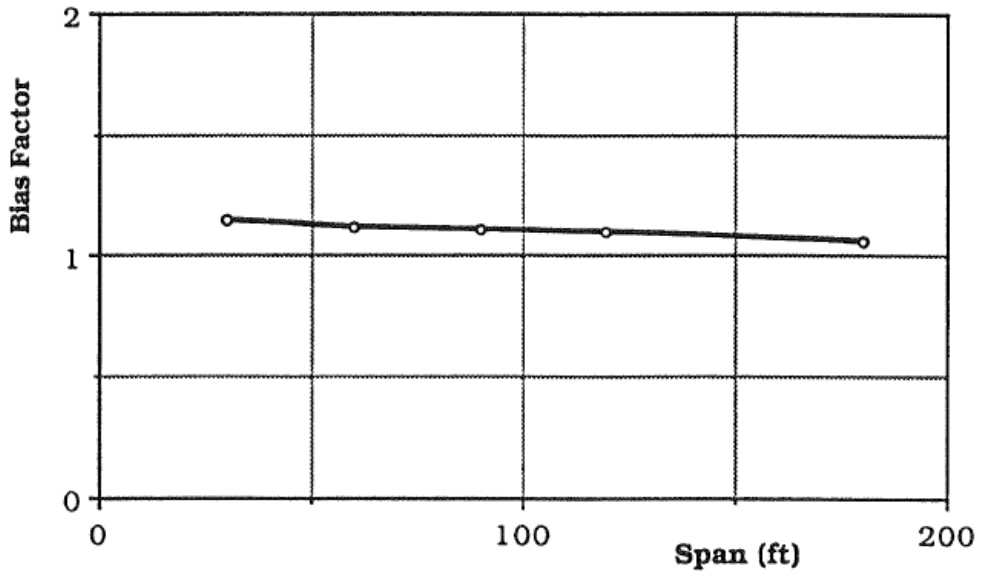

Figure 4-3 Bias Factor for the Maximum 75 Year Moment per Girder, LRFD Code (Nowak 1999)

The study analyzed data from 32 WIM stations, considering ADTT values of 500, 1000, 2500, 5000, and 10,000, and simple span lengths ranging from 30 to 300 feet. Live load effects were evaluated in terms of moments and reactions. The researchers determined the mean maximum load effects for various time periods, including 1 day, 2 weeks, 1 month, 2 months, 6 months, 1 year, 5 years, 50 years, 75 years, and 100 years. An example of the CDFs of mean maximum moment ratios (truck moment/HL-93 moment) for ADTT = 1000 and a span length of 120 feet is illustrated in Figure 4-4.

The mean of the mean maximum values of the considered WIM stations was considered the mean maximum national live load. The standard deviation of the mean maximum values was derived from the graphs, specifically the slope of the cumulative distribution function (CDF). The statistical parameters for maximum live load moments and reactions were calculated for all considered time periods, encompassing the various ADTTs and span lengths.

The AASHTO LRFD Specifications are based on an ADTT of 5000, consistent with strength limit states. Given that in the WIM database analyzed by Wassef et al. (2014), only 3 out of 32 WIM sites had an ADTT exceeding 5000, and only 1 site had an ADTT exceeding 8000, an ADTT of 5000 was used for the majority of the calibration in the Wassef et al. (2014) study and for the entire calibration in the present study. The statistical parameters for live load moments and reactions for an ADTT of 5000 are presented in Table 4-2 and Table 4-3.

The statistical parameters from Table 4-2 and Table 4-3 were utilized in the present study as follows. The statistical parameters for live load moments (Table 4-2) were applied to the flexural (service and strength) limit states, while the statistical parameters for live load reactions (Table 4-3) were applied to the web shear (service and strength) limit states. Additionally, since all the

bridges in the representative bridge database have span lengths exceeding 90 feet, only the statistical parameters for span lengths starting from 90 feet were used.

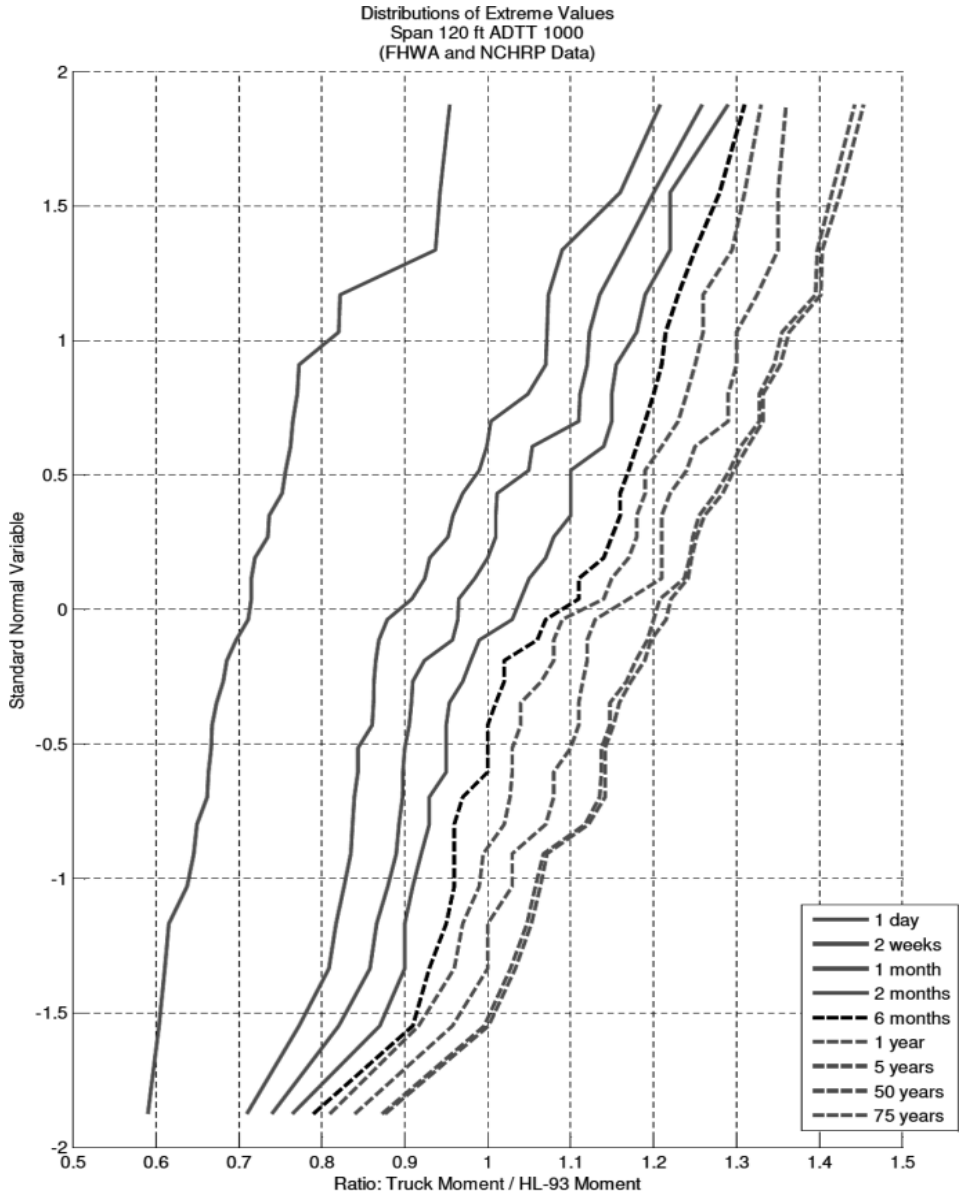

Figure 4-4 CDFs of Mean Maximum Moment Ratios for ADTT = 1000 and Span Length 120 ft (Wassef et al. 2014)

As previously mentioned, the maximum effects of live load over a 75-year period should be considered for strength limit states. Therefore, the statistical parameters corresponding to a 75-year return period were applied to the flexural and shear strength limit states.

Table 4-2 Statistical Parameters of Live Load Moments for ADTT 5000 (Adapted from Wassef et al. 2014)

Span Length	30 ft		60 ft		90 ft		120 ft		200 ft		300 ft		Note
	λ	*COV*	λ	*COV*	λ	*COV*	λ	*COV*	λ	*COV*	λ	*COV*	
1 Day	0.85	0.18	0.82	0.17	0.82	0.17	0.82	0.17	0.75	0.17	0.67	0.17	Used for arbitrary-point-in time live load
2 Weeks	0.98	0.17	1.00	0.17	1.00	0.16	1.04	0.13	0.96	0.14	0.88	0.14	
1 Month	1.04	0.15	1.03	0.18	1.12	0.11	1.11	0.09	0.99	0.14	0.93	0.14	
2 Months	1.07	0.15	1.07	0.17	1.15	0.10	1.14	0.10	1.02	0.14	0.96	0.14	
6 Months	1.11	0.14	1.11	0.14	1.19	0.08	1.17	0.09	1.04	0.15	1.00	0.15	
1 Year	1.14	0.12	1.14	0.14	1.21	0.09	1.19	0.09	1.07	0.15	1.02	0.15	Used for maximum live load for service limit states
5 Years	1.16	0.13	1.19	0.12	1.25	0.08	1.21	0.11	1.10	0.15	1.05	0.15	
50 Years	1.21	0.11	1.24	0.10	1.27	0.09	1.23	0.12	1.13	0.15	1.06	0.15	
75 Years	1.22	0.11	1.25	0.10	1.29	0.08	1.25	0.11	1.14	0.15	1.07	0.15	Used for maximum live load for strength limit states
100 Years	1.23	0.11	1.26	0.10	1.30	0.08	1.26	0.11	1.15	0.15	1.08	0.15	

Table 4-3 Statistical Parameters of Live Load Reactions for ADTT 5000 (Adapted from Wassef et al. 2014)

Span Length	30 ft		60 ft		90 ft		120 ft		200 ft		300 ft		Note
	λ	*COV*	λ	*COV*	λ	*COV*	λ	*COV*	λ	*COV*	λ	*COV*	
1 Day	1.05	0.12	0.94	0.11	0.96	0.13	0.94	0.13	0.84	0.14	0.74	0.14	Used for arbitrary-point-in time live load
2 Weeks	1.19	0.13	1.10	0.12	1.13	0.13	1.13	0.13	1.03	0.15	0.93	0.15	
1 Month	1.22	0.13	1.13	0.12	1.16	0.13	1.17	0.13	1.06	0.15	0.96	0.15	
2 Months	1.24	0.13	1.15	0.12	1.20	0.13	1.20	0.13	1.09	0.15	0.99	0.15	
6 Months	1.27	0.13	1.18	0.12	1.23	0.13	1.24	0.13	1.13	0.15	1.03	0.15	
1 Year	1.28	0.13	1.20	0.12	1.26	0.13	1.27	0.13	1.15	0.15	1.06	0.15	Used for maximum live load for service limit states
5 Years	1.32	0.13	1.25	0.12	1.30	0.12	1.30	0.13	1.19	0.15	1.09	0.15	
50 Years	1.36	0.13	1.29	0.12	1.35	0.12	1.35	0.13	1.23	0.15	1.14	0.15	
75 Years	1.37	0.12	1.30	0.12	1.36	0.12	1.36	0.13	1.24	0.15	1.15	0.15	Used for maximum live load for strength limit states
100 Years	1.38	0.12	1.31	0.12	1.37	0.12	1.37	0.13	1.25	0.15	1.15	0.15	

For the service limit states, a 1-year return period was utilized. This shorter time frame is employed to evaluate the bridge's performance under normal, everyday conditions, aiding in the assessment of cracking issues that impact the bridge's usability and comfort for daily traffic. By focusing on a typical year, the bridge's functionality and comfort for users can be ensured without requiring excessive maintenance. This return period was also chosen because the live load statistics in Wassef et al. (2014) were developed based on one year of reliable WIM data from various WIM sites.

When multiple variable load components are considered in a load combination, and one variable load component reaches an extreme value, the other variable load components are assumed to act at their average (arbitrary-point-in-time) values. This principle is known as Turkstra's rule (Nowak and Collins 2013). Therefore, when the live load is included in a load combination alongside other variable load components, and one of these components is at its maximum value, the live load component, according to Turkstra's rule, will be assumed to act at its average (arbitrary-point-in-time) value. For these arbitrary-point-in-time values, the statistical parameters with a return period of 1 day should be applied.

4.5. Statistical Models for Thermal Gradient

4.5.1. Background

Thermal gradient is a type of loading that requires thorough consideration. A thermal gradient describes the temperature variation over the course of a day across the depth of a bridge's superstructure. This temperature difference can cause different parts of the bridge to expand or contract at varying rates, leading to internal stresses. These stresses can impact the bridge's performance and durability, potentially causing issues like deck cracking, girder buckling, or

abutment spalling. The thermal gradient is often nonlinear, meaning the temperature change is not uniform across the depth of a bridge's superstructure. Instead, the temperature may vary more near the surface exposed to sunlight and less so deeper within the cross-section depth, creating complex stress patterns as different layers of the bridge expand and contract at different rates.

The primary factors influencing thermal gradient include solar radiation, ambient temperature variation, average wind speed, and blacktop thickness (Potgieter and Gamble 1983; Elbadry and Ghali 1983; Roberts-Wollman, Breen, and Cawrse 2002), as well as the orientation of the bridge to the sun (Priestley 1972). The climatic effects on thermal gradient are illustrated in Figure 4-5 (Thompson et al. 1998). The positive thermal gradient occurs when the top surface of the bridge is warmer than the reference point lower in the depth where the temperature remains constant. This typically happens during the day when the sun heats the bridge deck, causing the top to expand more than the lower depths, leading to upward bending, as discussed below. Conversely, a negative thermal gradient occurs when the top surface is cooler than the reference point, often at night when the bridge deck cools down faster than the lower depths. This results in the top contracting more than the lower depths.

The thermal gradient in concrete bridge structures was investigated in New Zealand by Priestley (1978). He explored the prediction of temperature by presenting the Fourier conductivity equation, which governs the thermal response of an isotropic solid with a boundary in contact with air, subjected to variations in ambient temperature and radiation. Priestley (1978) demonstrated that for most bridge sections, transverse heat flow is insignificant, allowing the Fourier conductivity equation to be simplified to a one-dimensional form. This equation can be solved using a two-dimensional finite element representation of the bridge section or the finite difference technique.

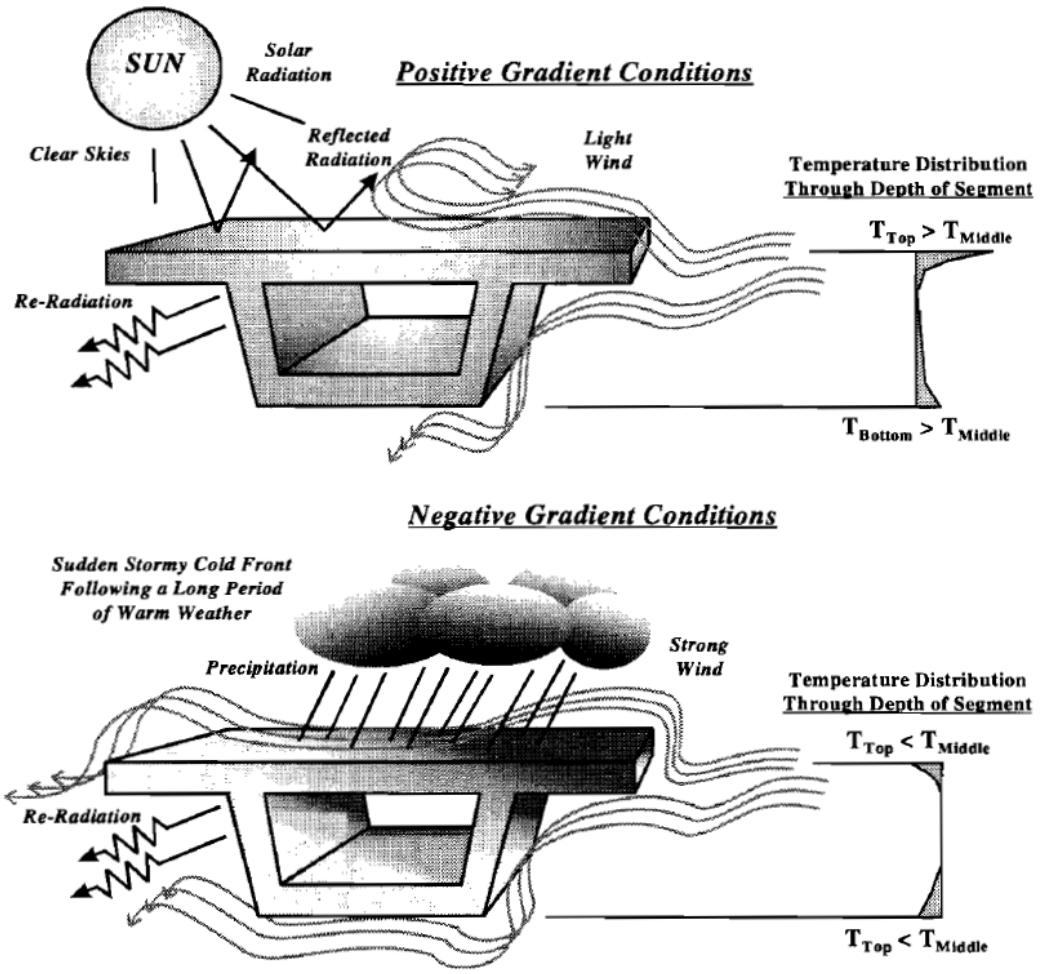

Figure 4-5 Climatic effects on thermal gradients (Thompson et al. 1998)

Priestley (1978) also provided a detailed description of stress prediction for simply supported and continuous segmental bridges. Figure 4-6 illustrates a typical schematic of the vertical temperature gradient that occurs in a bridge cross section over the course of a day. This temperature change induces strains. For completely unrestrained expansion at all heights, the free strain profile would be as follows:

$$\varepsilon_f = \alpha t_{(y)} \tag{4-7}$$

where α is the linear coefficient of thermal expansion.

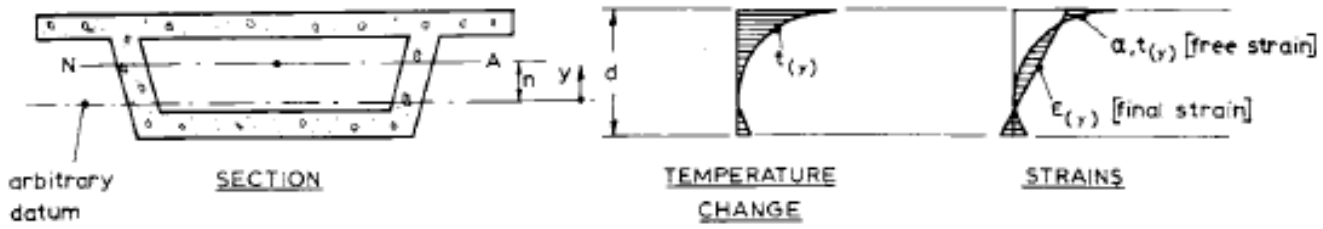

Figure 4-6 Vertical Distribution of Temperature Change and Longitudinal Thermal Strain (Priestley 1978)

However, the Navier-Bernoulli hypothesis, which states that plane sections remain plane, still applies in regions unaffected by geometric or loading discontinuities. Therefore, the final strain profile $\varepsilon_{(y)}$ (Figure 4-6) must be linear. The shaded area in Figure 4-6, representing the difference between the unrestrained strain $\alpha t_{(y)}$ and the final strain $\varepsilon_{(y)}$, suggests restraint stresses equal to (Priestley 1978):

$$f_{(y)} = E\left(\varepsilon_{(y)} - \alpha t_{(y)}\right) \tag{4-8}$$

where E is the concrete modulus of elasticity.

For simply supported bridges, each span is assumed to be "cut" at each internal support, allowing it to hog upwards under the thermal curvature, ψ. However, for continuous bridges, the hogging curvature is restrained by internal supports. The restraint moments at the supports are illustrated in Figure 4-7 for a three-span bridge. These restraint moments, M, are applied to each end of each span to eliminate incompatible rotations (Priestley 1978). For prismatic sections, the restraint moments for each span are equal to:

$$M = -EI\psi \tag{4-9}$$

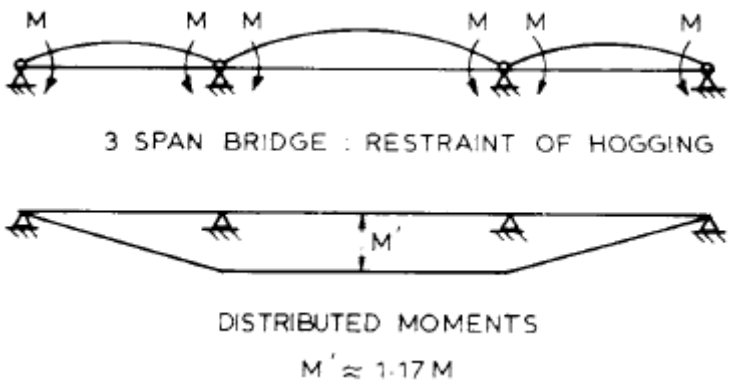

Figure 4-7 Continuity Moments from Thermal Loads (Priestley 1978)

The moments restrained at the ends can be released. Consequently, the final distributed moments, denoted as *M'*, will be as illustrated in Figure 4-7 and are roughly equal to $M' = 1.17\,M$ (Priestley 1978). The stresses induced by M' will be

$$f_{(r)} = \frac{M'y}{I} \tag{4-10}$$

The total thermal stresses resulting from the vertical thermal gradient are a combination of stresses caused by the gradient's nonlinearity (Equation (4-8)) and continuity stresses (Equation (4-10)), as shown in Figure 4-8 (Priestley 1978). Specifically,

$$f = f_{(y)} + f_{(r)} = E\left(\varepsilon_{(y)} - \alpha t_{(y)}\right) + \frac{M'y}{I} \tag{4-11}$$

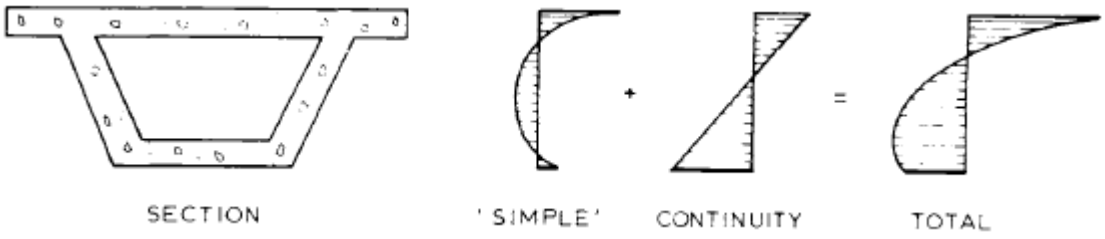

Figure 4-8 Vertical Thermal Stress Distribution, Continuous Bridge (Priestley 1978)

The total service load stress distribution at midspan, resulting from the typical combination of prestress, dead load, live load, and temperature, is illustrated in Figure 4-9. The final stress distribution might show excessive compression stress at the deck level or tension stress at the soffit. The former is unlikely to cause issues, even if the compression stress significantly exceeds the maximum codified value, because the large thermal component is strain-induced, and ultimate compressive strains are much larger than design strain levels. However, excessive tension at the bottom slab (soffit) could lead to cracking and subsequent serviceability problems (Priestley 1978).

Figure 4-9 Service Load Stresses Including Thermal Stress (Priestley 1978)

The New Zealand design thermal gradient, depicted in Figure 4-10, consists of two parts: a fifth power temperature decrease from a maximum temperature (which varies based on the blacktop thickness) at the concrete deck surface to zero at a depth of 1200 mm (47.2 in.), and a linear temperature increase over the bottom 200 mm (7.9 in.) of the section. The cracking induced by thermal gradients reduces the flexural rigidity. Thermal forces at service loads are more significant than their contribution to structural strength. (Priestley 1978).

The first design thermal gradient in the United States was developed in NCHRP Report 276 (Imbsen et al. 1985), as illustrated in Figure 4-11, and was first introduced in the design code in AASHTO Guide Specifications (1989). The temperatures T_1, T_2, and T_3 vary across different thermal zones in the US. Subsequently, Shushkewich (1998) provided a comparison of both positive and negative design thermal gradients as outlined in AASHTO (1989; 1994; 1999), as illustrated in Figure 4-12. The design positive vertical temperature gradient in concrete

superstructures, as specified in the most recent AASHTO LRFD (2020) Specifications, is illustrated in Figure 4-13.

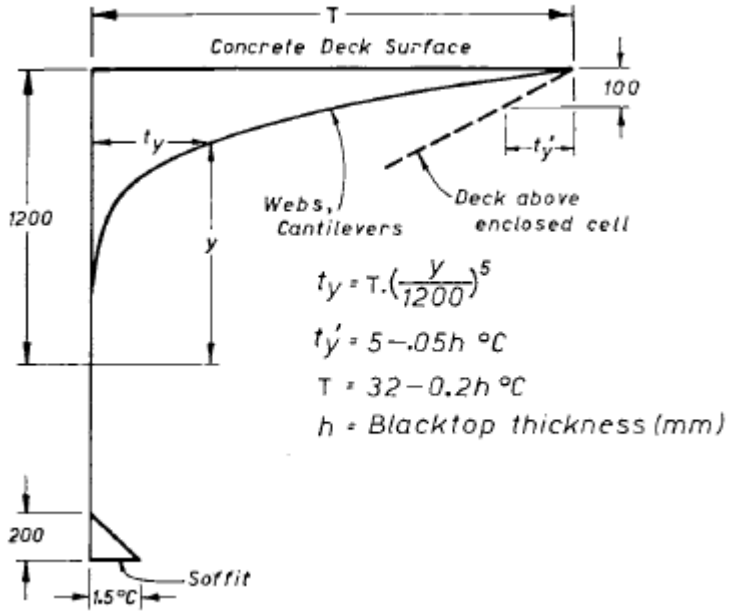

Figure 4-10 New Zealand Design Thermal Gradient (Priestley 1978)

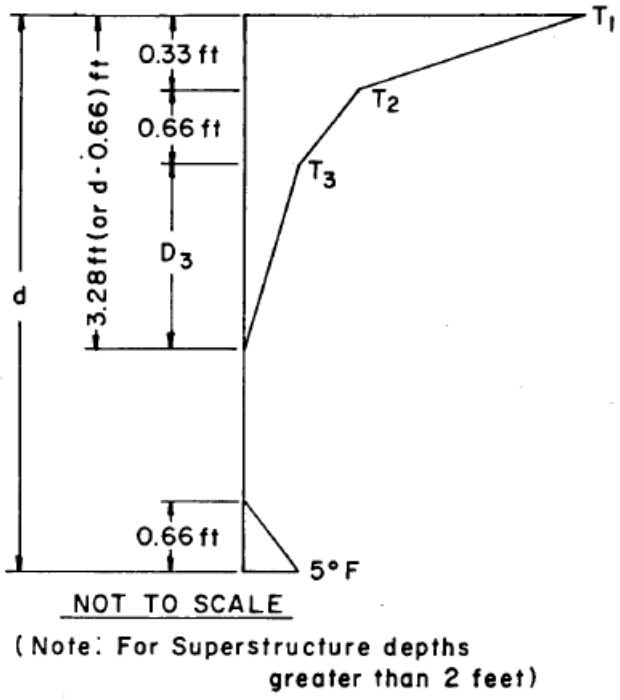

Figure 4-11 Positive Vertical Temperature Gradient within Superstructure Concrete (Imbsen et al. 1985)

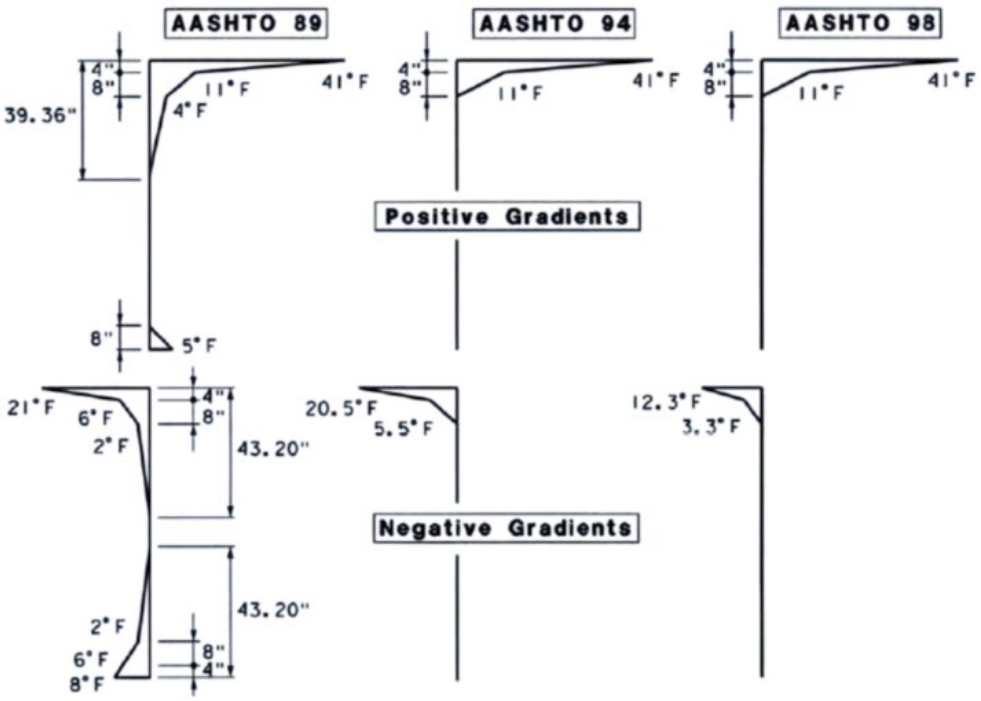

Figure 4-12 Comparison of Design Thermal Gradients (Shushkewich 1998)

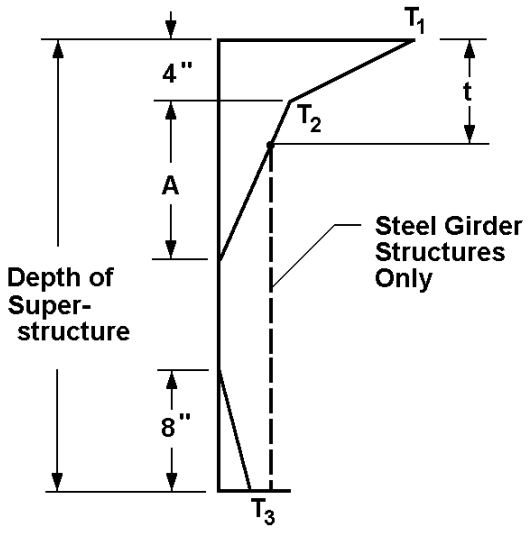

Figure 4-13 Positive Vertical Temperature Gradient in Concrete and Steel Superstructures (AASHTO LRFD 2020)

4.5.2. Thermal Gradient Data and Experiments

Given the challenges associated with thermal gradients and its effect on segmental bridges, as discussed above, there have been efforts to collect thermal gradient data to better understand the typical thermal gradient distribution and enhance the design gradient.

Initially, Potgieter and Gamble (1983) conducted field measurements on the Kishwaukee River Bridge, a continuous five-span segmental box girder bridge with blacktop covering located south of Rockford, Illinois. Data was collected on July 8th and 9th, 1982. The measured thermal gradients were compared to calculated values, as illustrated in Figure 4-14 for the section, close to midspan, and the temperature distribution along the depth is shown in Figure 4-15. The investigation showed that the shape of the New Zealand gradient matched the measured thermal gradients, but the top surface magnitude did not.

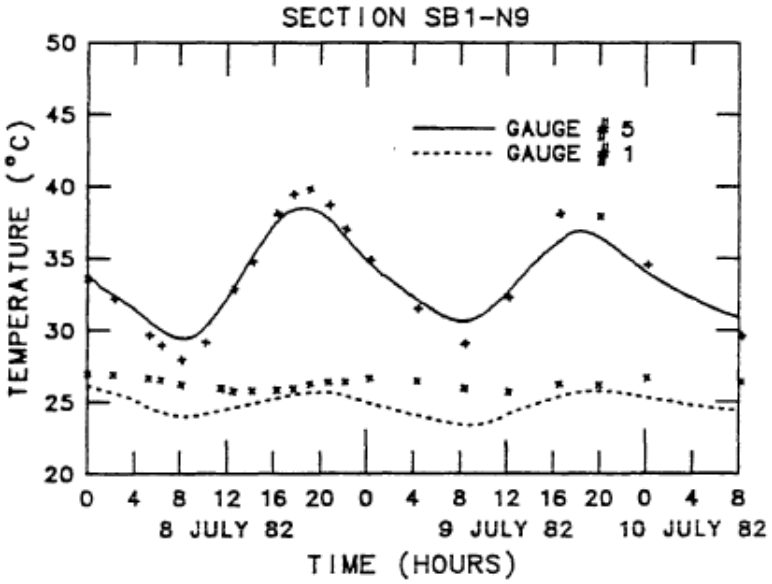

Figure 4-14 Comparison of Measured and Calculated Temperature Variations in center of Top and Bottom Flanges of Section (Potgieter and Gamble 1983)

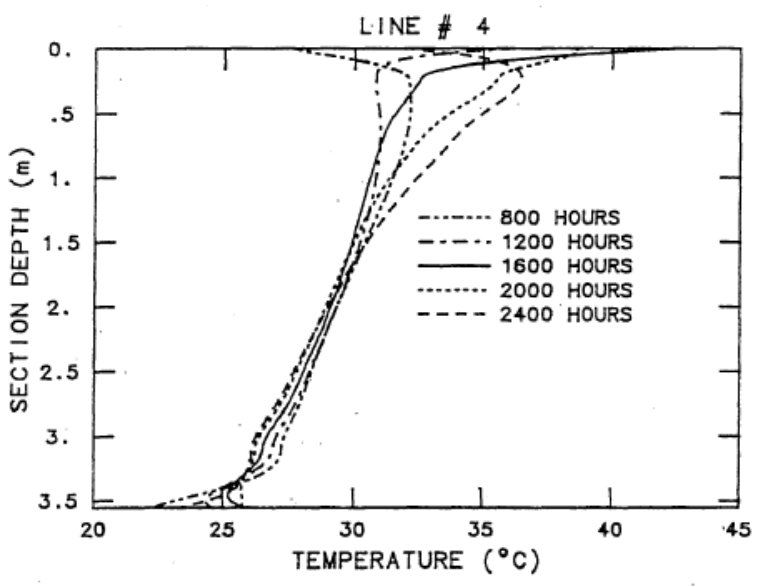

Figure 4-15 Temperature Distributions at Different Times of 8 June 1982 for the Center of Segment (Potgieter and Gamble 1983)

Cooke, Priestley, and Thurston (1984) conducted an experimental investigation involving the thermal loading of T-beam and box-girder beam models at approximately one-sixth scale. The authors compared experimental and theoretical deflections, as illustrated in Figure 4-16. Although this study did not involve measuring temperatures in full-scale structures and was conducted on a small scale, it provided valuable insights into the influence of thermal loading on deflections.

Shushkewich (1998) collected thermal gradient data for the North Halawa Valley Viaduct, a cast-in-place concrete box girder bridge in Hawaii, over a period from late 1994 through 1998. The thermocouple readings for the top of a midspan section in 1995 are shown in Figure 4-17, and the temperature distribution across the section depth on July 1, 1995, when the maximum concrete deck temperature occurred, is illustrated in Figure 4-18. Positive and negative thermal gradients were found to align well with the AASHTO (1999) proposals.

Thompson et al. (1998) gathered thermal gradient data for the Ramp P structure, a curved precast segmental concrete box girder bridge on US 183 in Austin, Texas, between November

1996 and July 1997. The maximum measured positive and negative gradients, which occurred in March of 1997, are shown in Figure 4-19. Thermal gradients were measured with and without a 50-mm (2-in.) blacktop covering. The measured gradients were generally lower than those specified in AASHTO LRFD (1994). However, it was noted that additional data were required for a robust statistical comparison.

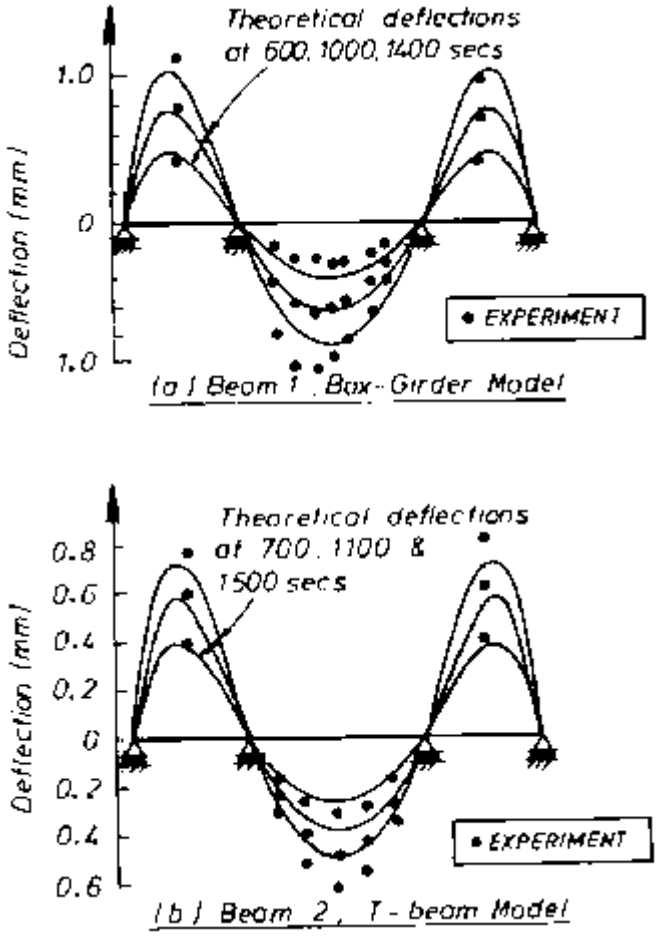

Figure 4-16 Experimental and Theoretical Deflection Profiles for Beams (Cooke, Priestley, and Thurston 1984)

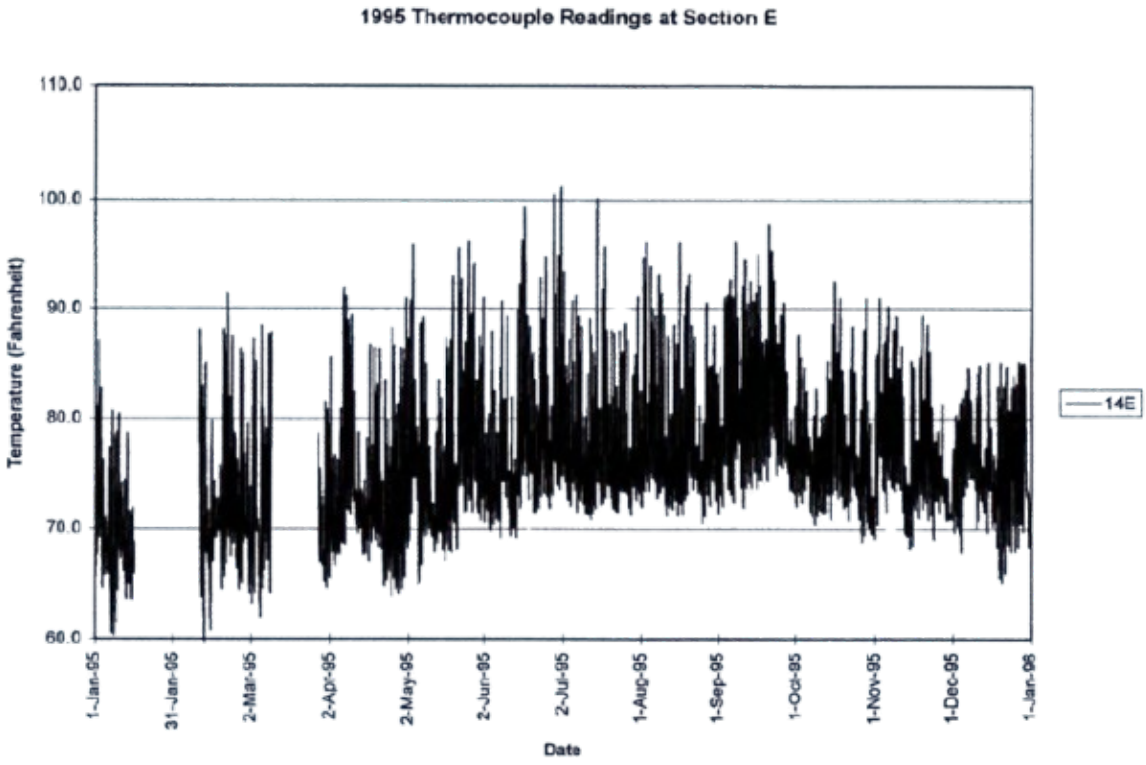

Figure 4-17 1995 Thermocouple Readings (Shushkewich 1998)

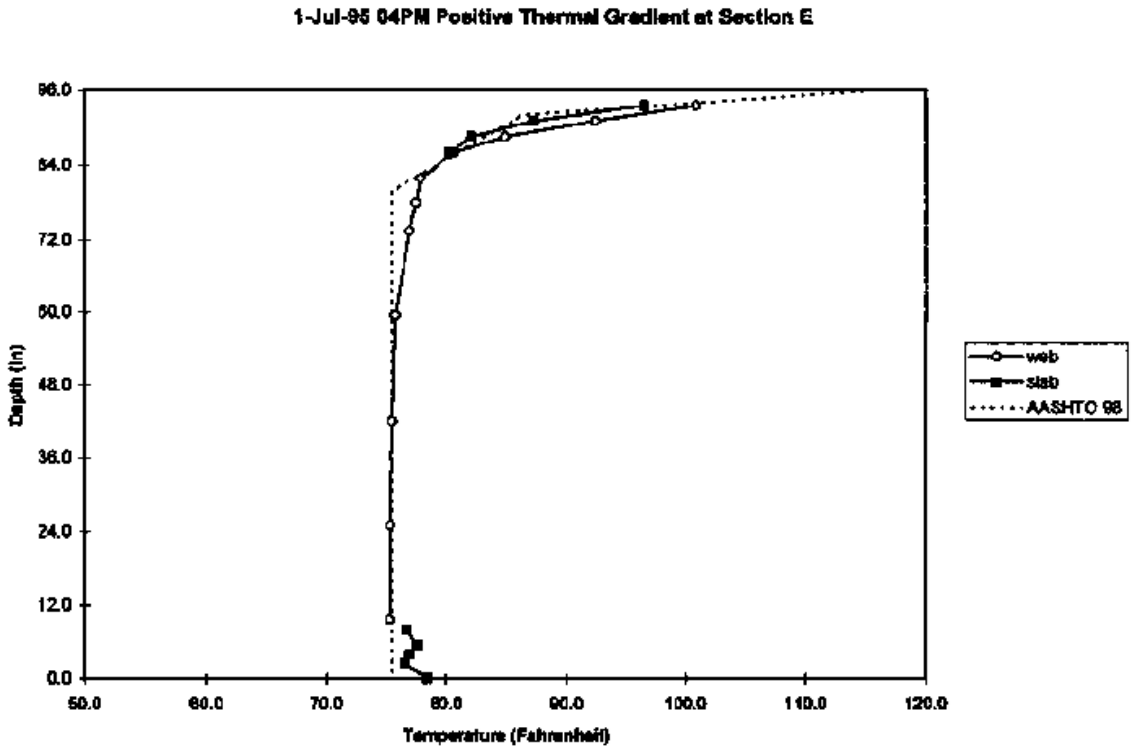

Figure 4-18 July 1, 1995, Temperature Distribution (Shushkewich 1998)

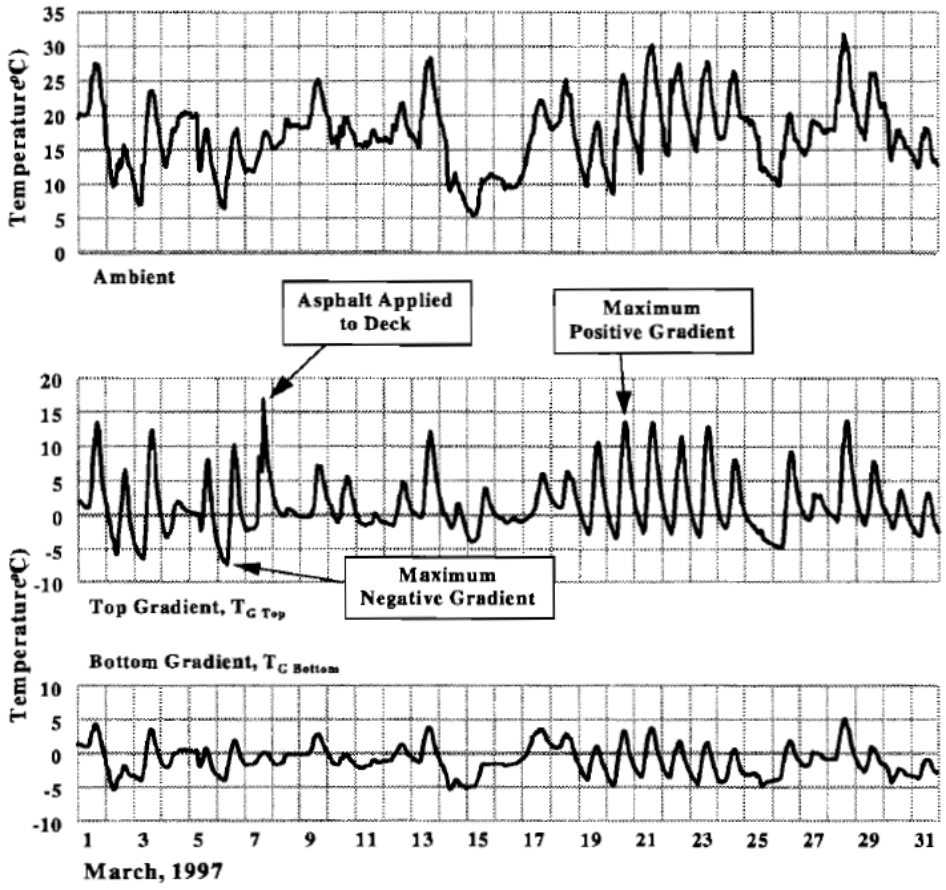

Figure 4-19 Measured Thermal Gradients for the Month of March 1997 (Thompson et al. 1998)

Roberts-Wollman, Breen, and Cawrse (2002) gathered thermal gradient data for the San Antonio "Y" precast segmental concrete box girders in Texas from July 1992 through November 1994. The maximum daily positive temperature differences are illustrated in Figure 4-20 where they are compared with the design gradient magnitudes (AASHTO 1994; 1999), and the maximum recorded positive temperature gradients across the section depth are shown in Figure 4-21. The authors concluded that typical positive gradients could be approximated using a fifth-order curve, similar to the one presented by Priestley (1978). They also mentioned that the positive and negative design gradients in AASHTO LRFD (1994) were conservative.

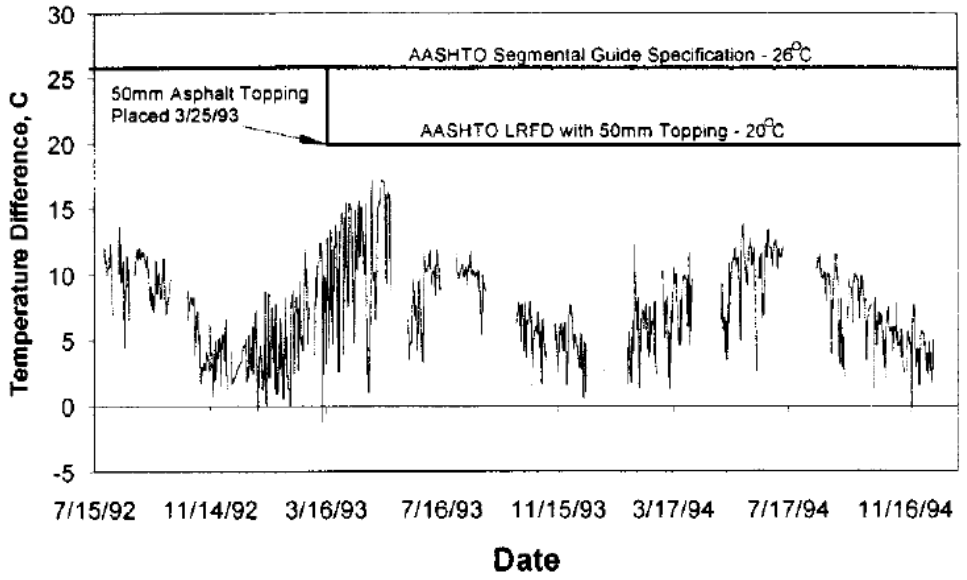

Figure 4-20 Maximum Daily Positive Temperature Differences

(Roberts-Wollman, Breen, and Cawrse 2002)

Hedegaard, French, and Shield (2013) collected thermal gradient data for the I-35W St. Anthony Falls Bridge, a posttensioned concrete box girder structure in Minneapolis, Minnesota, over the course of 3 years from September 1, 2008, to October 26, 2011. The measured positive and negative gradient magnitudes are illustrated in Figure 4-22, where they are compared with the design magnitudes at the depth of the thermistors. The considered design thermal gradients are the AASHTO LRFD (2010) gradient in Zone 2 (top surface gradient temperature equal to 25.6°C (46°F)) and the Priestley fifth-order gradient (Priestley 1978), scaled to the same top surface gradient temperature (Priestley-Z2). Since top surface temperature measurements could not be taken, comparisons between measured and design gradient magnitudes had to use the design gradient value at a depth of 50 mm (2 in.) below the deck's top surface, where the topmost thermistor was positioned.

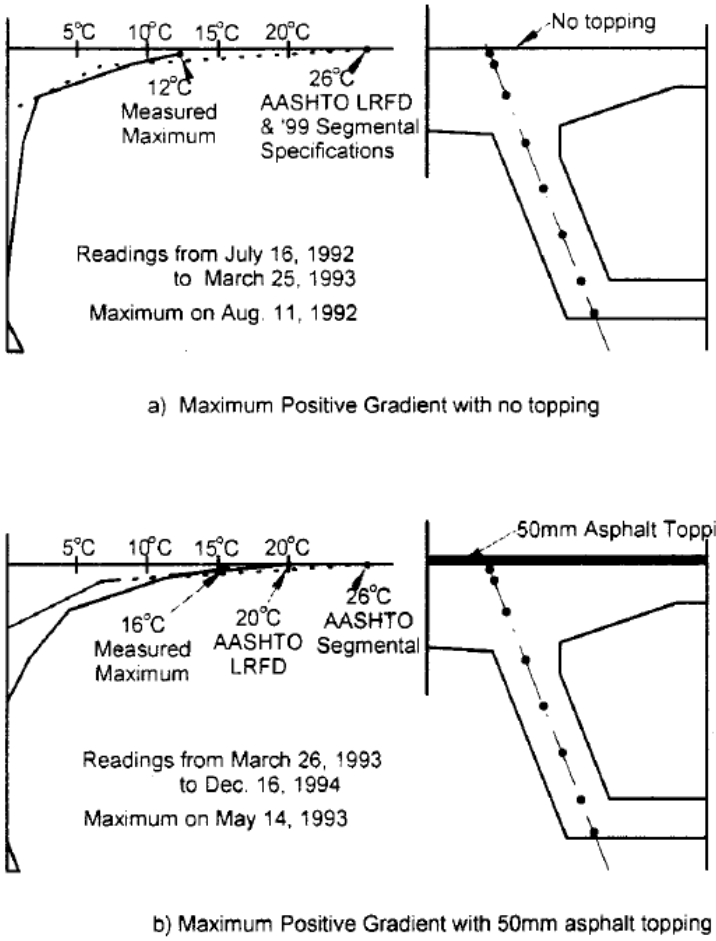

Figure 4-21 Maximum Recorded Positive Temperature Gradients

(Roberts-Wollman, Breen, and Cawrse 2002)

Figure 4-23 shows the five highest measured positive gradients compared to the two previously mentioned designed gradients. The thermal gradient shapes through the section depth closely resembled the fifth-order curve from the New Zealand Code (Priestley 1978). The highest measured top surface gradient temperatures aligned best with the top surface temperature specified in AASHTO LRFD (2010) for solar radiation Zone 2 (Hedegaard, French, and Shield 2013).

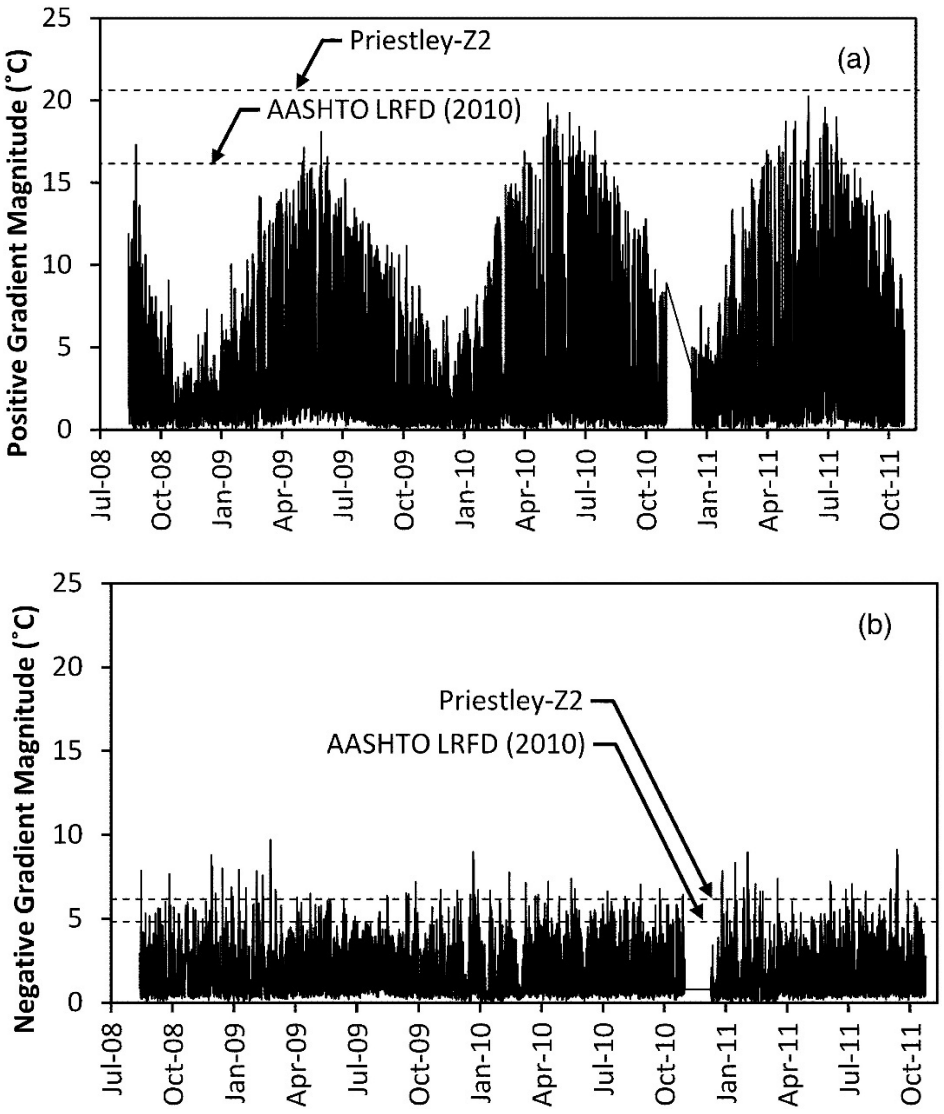

Figure 4-22 Measured (a) Positive and (b) Negative Gradient Magnitudes: Design Gradient Magnitudes Considered at a Depth of 50 mm (2 in.) below the Deck Surface for Comparison against Measured Gradients (Hedegaard, French, and Shield 2013)

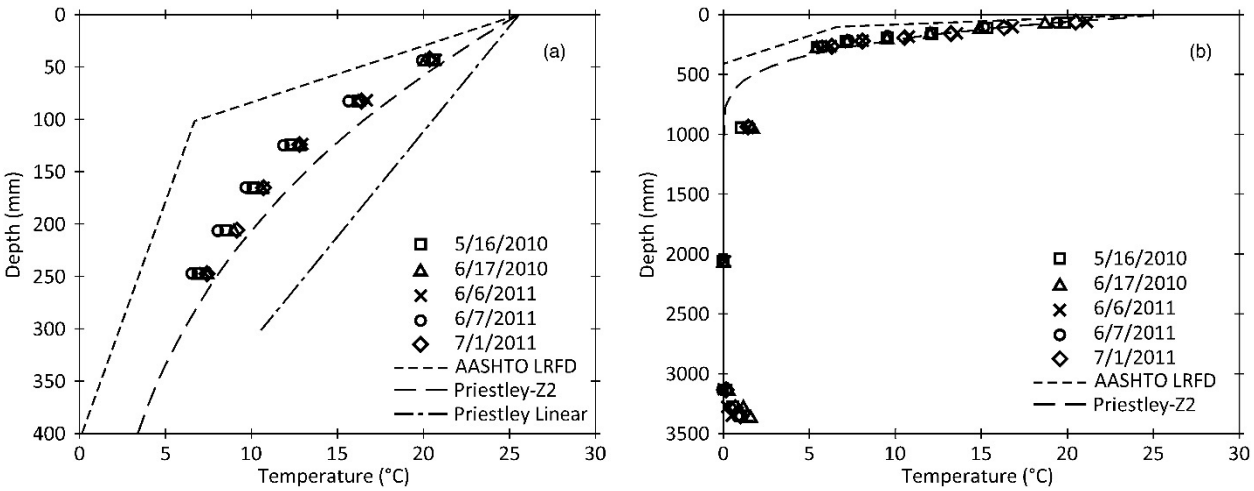

Figure 4-23 Maximum Measured Positive Gradients at Midspan Location Compared with Design Gradients through (a) Centerline of Exterior Box, Top Flange Only, and (b) along Centerline of West Web of Exterior Box (Hedegaard, French, and Shield 2013)

The highest measured positive thermal gradients caused greater experimentally derived longitudinal stresses than those observed during truck load testing (Hedegaard et al. 2013). Placing eight trucks with a total weight of 1,770 kN (398 kips) at the midspan of the internal span resulted in an experimentally derived longitudinal stress of 1.8 MPa (260 psi) in the bottom flange. This stress level was surpassed for all the maximum positive gradients considered, with experimentally derived longitudinal stresses in the bottom flange ranging from 3.1 MPa (450 psi) to 4.7 MPa (680 psi) (Hedegaard, French, and Shield 2013). This highlights the critical need to properly account for thermal gradients.

As shown in Figure 4-22, the highest thermal gradient values occur during the summer period. The peak daily positive gradients consistently occurred between 2:00 and 4:00 p.m. Central Standard Time (CST) (Hedegaard, French, and Shield 2013). This is because the significant factors influencing thermal gradients, such as solar radiation and ambient temperature variation (as

discussed before), are most pronounced during the summer period and the specified afternoon hours.

The consistent occurrence of the highest daily positive gradients between 2:00 and 4:00 p.m. CST suggests a possible correlation between live load during rush hour and maximum thermal gradient effects (Hedegaard, French, and Shield 2013). However, it is recommended to investigate this correlation further to determine if the current load factors for the combination of live load and thermal gradient ($\gamma_{LL}\ LL + 0.5TG$ and $1.0TG + 0LL$) are adequate and, if necessary, perform the calibration to refine them.

Maguire, Roberts-Wollmann, and Cousins (2018) measured thermal gradients on the Varina-Enon Bridge, which carries Interstate 295 over the James River near Richmond, Virginia, from August 2012 to January 2014. The bridge features separate northbound and southbound structures with continuous segmental box-girder approaches and a cable-stayed main span. Figure 4-24 shows the measured temperature gradient near the midspan, which had the expected shape but was less severe than AASHTO LRFD (2010) design positive thermal gradient.

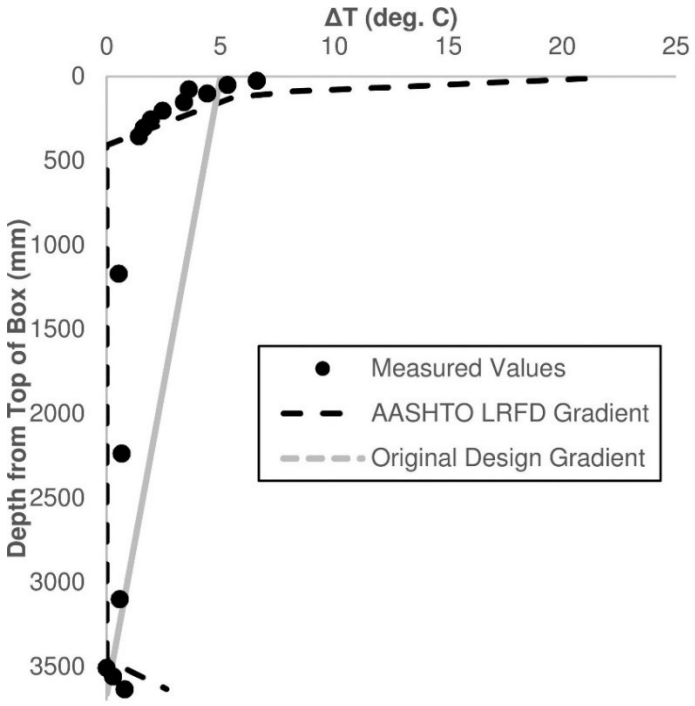

Figure 4-24 Measured Thermal Gradient on the Varina-Enon Bridge

(Maguire, Roberts-Wollmann, and Cousins 2018)

4.5.3. Derivation of Statistical Parameters for Thermal Gradient

The derivation of the statistical parameters for the present study was based on the data from Hedegaard, French, and Shield (2013), as their published work provided the comprehensive range of measured positive thermal gradients over the entire measurement period from September 2008 through October 2011 (Figure 4-22a).

As shown of Figure 4-22a, the AASHTO LRFD design thermal gradient value at the top measured location is 16.2°C. This value was used as a nominal value for the derivation.

To derive the statistical parameters, the data from Figure 4-22a was read to capture the maximum and minimum thermal gradient values for each month from September 2008 through October 2011, totaling 38 months.

The statistical parameters were derived for the entire dataset of data (arbitrary-point-in-time) and for the maximum data within a 1-year period. The specifics of these statistical considerations were discussed in Section 4.4.2. The 1-year maximum period was selected to align with the same maximum period considered for the live load at service limit states, where the thermal gradient is a significant load component and should be considered.

To derive the 1-year maximum statistical parameters, the highest thermal gradient values from 2008 to 2011 were utilized. As previously mentioned, these maximum values typically occur during the summer period; therefore, the four maximum values specifically occurred in September 2008, June 2009, May 2010, and June 2011, and they are 17.3°C, 18.1°C, 19.8°C, and 20.3°C, respectively. The average of these values was calculated to be

$$\mu_{TG,max} = 18.9°C$$

The standard deviation was calculated to be

$$\sigma_{TG,max} = 1.2°C$$

Applying Equation (3-7), the bias factor and coefficient of variation were determined as follows:

$$\lambda_{TG,max} = \frac{\mu_{TG,max}}{TG} = \frac{18.9°C}{16.2°C} = 1.15$$

$$COV_{TG,max} = \frac{\sigma_{TG,max}}{\mu_{TG,max}} = \frac{1.2°C}{18.9°C} = 0.06$$

These statistical parameters are to be used when a load combination with maximum thermal gradient (*TG*) and average live load (*LL*) is applied in accordance with Turkstra's Rule (Section 4.4.2).

To derive the arbitrary-point-in-time statistical parameters, the average values for each month in the dataset were first estimated by calculating the mean of the maximum and minimum

values for each month. Subsequently, an average value from all the 38 data points was calculated to be

$$\mu_{TG,arb} = 9.5°C$$

The standard deviation was calculated to be

$$\sigma_{TG,arb} = 3.3°C$$

Applying Equation (3-7), the bias factor and coefficient of variation were determined as follows:

$$\lambda_{TG,arb} = \frac{\mu_{TG,arb}}{TG} = \frac{9.5°C}{16.2°C} = 0.55$$

$$COV_{TG,arb} = \frac{\sigma_{TG,arb}}{\mu_{TG,arb}} = \frac{3.3°C}{9.5°C} = 0.35$$

These statistical parameters are to be used when a load combination with average thermal gradient (*TG*) and maximum live load (*LL*) is applied in accordance with Turkstra's Rule.

Both sets of calculated statistical parameters are logical. The average of the 1-year maximum values is expected to be higher than the average of all data points, as the former represents the peak values. The four maximum thermal gradient values occurring during the summer period exhibit low variation, resulting in a smaller variation compared to the entire dataset. Consequently, the variation within the entire dataset is significantly larger than that of the few considered 1-year maximum values.

4.5.4. Summary

Table 4-4 contains all the statistical parameters for loads used in the present study.

Table 4-4 Statistical Parameters for Loads

Load Component	λ	***COV***	**Source/Reasoning**
DC (CIP)	1.05	0.10	Nowak (1999)
DC (Precast)	1.03	0.08	
DW	1.00 (3.5 in./3.5 in.)	0.25	
CR, SH, TU	1.00	0.15	Grouni and Nowak (1984), engineering judgment
PS, PS_{sc}	1.25	0.05	Grouni and Nowak (1984), modified based on the present study
TG (arbitrary-point-in-time)	0.55	0.35	Derived in present study based on data from (Hedegaard et al. 2013)
TG (1-year maximum)	1.15	0.06	

5. DEVELOPMENT OF STATISTICAL MODELS FOR RESISTANCE

As mentioned in Section 2.1.2, different parameters represent resistance in service and strength limit states. For service limit states, these parameters are allowable flexural and shear stresses, while for strength limit states, they are the bending moment and shear force capacities. Allowable stresses are more straightforward to incorporate into the reliability analysis than moment and shear capacities, as the former involve only one parameter, whereas the latter require comprehensive procedures involving multiple parameters representing material and fabrication factors, as well as a professional factor, as described in Section 3.3. The selection and development of statistical models for the various parameters involved in resistance for the considered service and strength limit states, and their integration using Monte Carlo simulation for strength limit states, are further detailed in the following sections of this chapter.

5.1. Service Limit States

5.1.1. Service Flexure Limit State

In Section 1.1, two main types of joints between segments are identified: Type A, which uses epoxy, and Type B, which are dry joints without epoxy (Corven Engineering 2004). All the bridges in the representative bridge database have Type A joints that use epoxy. As mentioned in Section 4.3, the stress limit for Type A joints without the minimum bonded auxiliary longitudinal reinforcement through the jointsis zero tension ($f_R = 0$). Similarly, according to AASHTO LRFD (2020) Table 5.9.2.3.2b-1, which lists tensile stress limits in prestressed concrete at the service limit state after losses (Table 1-2), the limit for longitudinal stresses through joints in the precompressed tensile zone without the minimum bonded auxiliary reinforcement is also zero tension. This modifies Equation (2-1) as follows:

$$0 - (f_{DC} + f_{DW} + f_{PS} + f_{CRSH} + f_{TU} + f_{TG} + f_{LL}) = 0 \quad (5\text{-}1)$$

The allowable normal flexural stress of $f_R = 0$ determines the point of decompression, which is transition from compression to tension at an extreme fiber, with no variation in this transition. Consequently, the parameter $f_R = 0$ is deterministic, with $\mu = 0$ and $\sigma = 0$.

5.1.2. Service Principal Tension Limit State

AASHTO LRFD (2020) Article 5.9.2.3.3 specifies the allowable principal tensile stress as $f_{PT,R} = 0.110\sqrt{f_c'}$ ksi. This stress is related to cracking stress, which exhibits variation, unlike decompression stress. Therefore, the statistical parameters of cracking stress should be utilized. Nowak and Grouni (1983) and Grouni and Nowak (1984) in their studies related to the calibration of the Ontario Bridge Design Code specify the mean cracking stress for prestressed concrete as μ = 700 psi (0.7 ksi or 4.83 MPa), using high-strength concrete, and the coefficient of variation *COV* = 20% (0.20). The principal tensile stress limit is significantly lower than the uniaxial cracking stress due to the biaxial tension-compression state. Studies by Belarbi (1991) and Yu et al. (2019) (Figure 5-1 and Figure 5-2) indicate that the measured tensile cracking stress (with compressive stress in the perpendicular direction) is approximately $3.75\sqrt{f_c'}$ psi ($0.1185\sqrt{f_c'}$ ksi), which was used as the mean value, μ, for the allowable principal tensile stress for the present study. Thus, the bias factor is $\lambda = 3.75\sqrt{f_c'}$ psi / $3.5\sqrt{f_c'}$ psi = 1.07, and the coefficient of variation was used as *COV* = 0.20.

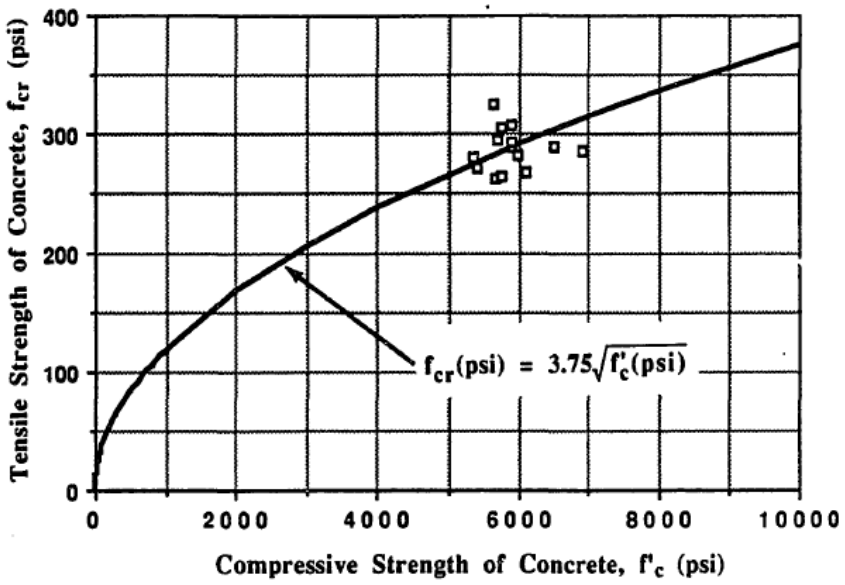

Figure 5-1 Cracking Stress versus Cylinder Compressive Strength (Belarbi 1991)

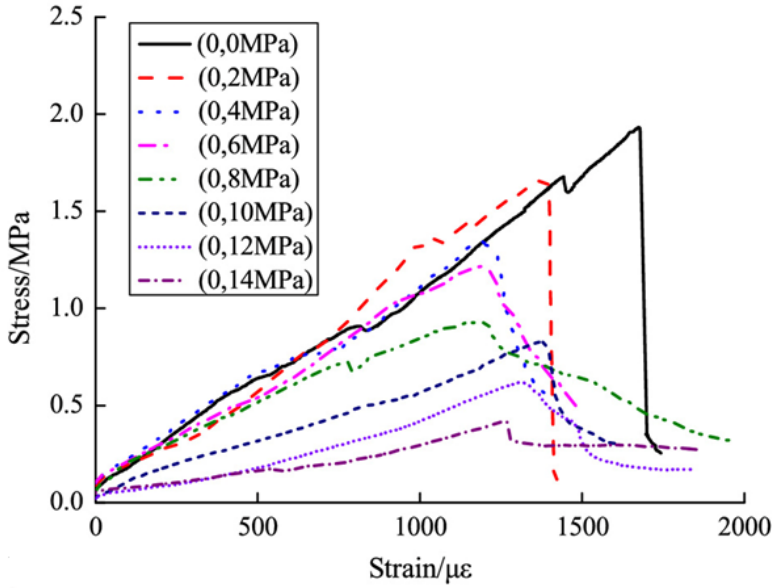

Figure 5-2 Principal Tensile Stress-Strain Curves of C30 (f'_c = 30 MPa = 4350 psi) Concrete under Biaxial Tension-Compression (Yu et al. 2019)

5.2. Strength Limit States

5.2.1. Flexural Strength Limit State

The nominal bending moment capacity (M_n) is a complex parameter determined by following the procedure outlined in Section 3.3.1. To develop statistical models for the nominal moment capacity, a procedure such as a Monte Carlo simulation, described in Section 3.3.3, is required. This simulation involves randomly generating values for each variable necessary to determine the flexural strength. Consequently, the statistical parameters for each variable must be established.

The material factor, M, is a statistical distribution that represents the uncertainty in material properties, specifically strength-related characteristics such as:

- f_{pu} = specified tensile strength of prestressing steel
- f'_c = specified concrete compressive strength.

The fabrication factor represents geometric and dimensional uncertainties in the fabrication of structures (Nowak and Collins 2013). The variables involved in the procedure to determine M_n representing the fabrication factor, F, are:

- A_{ps} = area of prestressing steel
- b = width of the compression face of the member
- d_p = distance from extreme compression fiber to the centroid of prestressing tendons

Additionally, a professional factor, P, is involved in the Monte Carlo simulation procedure. The professional factor, P, is a random variable that represents the uncertainty in the analytical model used to predict strength. P is defined as the ratio of the test-determined capacity (which reflects actual in-situ performance) to the analytically predicted capacity (based on the mathematical model used in design) using measured material properties and dimensions rather than nominal values.

The following subsections detail the selection of statistical models for the aforementioned parameters, as available in the literature, and the development of updated statistical parameters for the fabrication factor.

5.2.1.1. Statistical Models Available in the Literature

Past statistical analyses of materials for reinforced concrete construction were based on the relevant datasets available at the time.

Ellingwood et al. (1980) utilized the dataset of material and geometric properties for steel reinforcing bars and prestressing strands that were available in the 1970s. The fabrication factors adapted from this study are summarized in Table 5-1.

Table 5-1 Fabrication Factors (Adapted from Ellingwood et al. (1980))

Fabrication Factor	λ_F	COV_F
b_w	1.01	0.04
d (for beams)	0.99	0.04
d (for slabs)	0.92	0.12
A_s	1.00	0.015
A_v	1.00	0.015
s	1.00	0.04

In 2005, Nowak et al. (2005) conducted a reliability-based calibration of the ACI 318 Building Design Code strength reduction (resistance) factors, aligning them with the load and load combination factors specified by the ASCE 7 Standard (ASCE/SEI 7 2002). This study was sponsored by the Portland Cement Association (PCA) and co-sponsored by the Precast/Prestressed Concrete Institute (PCI). The research involved developing extensive sets of statistical parameters based on material test data for concrete, reinforcing steel, and prestressing steel, provided by the industry through the National Ready Mixed Concrete Association (NRMCA) between 2001 and

2004. Most of the data available at that time were representative of cast-in-place (CIP) concrete construction. The parameters λ_F and COV_F denote the fabrication factor representing the uncertainty in dimensions and location of reinforcing bars and prestressing strands in a section.

Nowak et al. (2005) determined test results for 28-day compressive strength using standard 6 in. x 12 in. cylinders, analyzed for the following types of concrete:

- Cast-in-place ready mixed concrete with specified strengths ranging from 3,000 to 6,500 psi (11,098 samples),
- Plant-cast concrete with specified strengths ranging from 5,000 to 6,500 psi (1,174 samples),
- Plant-cast concrete with specified strengths ranging from 7,000 to 12,000 psi (2,052 samples), and
- Lightweight concrete with specified strengths ranging from 3,000 to 5,000 psi (550 samples).

The resulting statistical parameters for all concrete compressive strengths recommended by Nowak et al. (2005) are shown in Table 5-2. It is important to note that the results in Table 5-2 represent the average for all types of concrete and concrete production operations considered in that study. The parameters λ_M and COV_M denote the material factor representing the uncertainty in the compressive strength of concrete.

The available data for prestressing steel came from test data on the breaking strength of prestressing strands, provided by the industry in a study sponsored by the Portland Cement Association (PCA) and co-sponsored by the Precast/Prestressed Concrete Institute (PCI), as reported by Nowak et al. (2005). For strands with a specified breaking strength of 270 ksi (47,668 samples), the included strand sizes (nominal diameter) were: 3/8 in. (54 samples), 7/16 in. (16

samples), 1/2 in. (33,570 samples), and 0.6 in. (14,028 samples). The recommended statistical parameters for the breaking strength of Grade 270 prestressing strands, according to Nowak et al. (2005) are $\lambda = 1.03$ and $COV = 0.015$.

The professional factor, P, used in previous reliability-based calibrations and related research has largely been based on the work of MacGregor, Mirza, and Ellingwood (1983) and Ellingwood et al. (1980), which primarily focused on cast-in-place concrete members. A study by Mirza, Kikuchi, and MacGregor (1980) on prestressed concrete beams has also been used as a reference for defining P in subsequent reliability research efforts.

Table 5-2 Statistical Parameters for Compressive Strength (Including Both Cast-in-Place and Plant-Cast Concrete) from Nowak et al. (2005)

f'_c (psi)	λ_M	COV_M
3,000	1.31	0.170
3,500	1.27	0.160
4,000	1.24	0.150
4,500	1.21	0.140
5,000	1.19	0.135
5,500	1.17	0.130
6,000	1.15	0.125
6,500	1.14	0.120
7,000	1.13	0.115
8,000	1.11	0.110
9,000	1.10	0.110
10,000	1.09	0.110
12,000	1.08	0.110

Mirza, Kikuchi, and MacGregor (1980) conducted a study on the flexural strength of bonded strands in prestressed concrete beams with the goal of suggesting resistance factors. As

part of this study, several relevant statistical parameters were analyzed, including the professional factor. Mirza, Kikuchi, and MacGregor (1980) selected 33 simply supported, prestressed concrete beams with concrete compressive strengths ranging from 2,500 to 8,500 psi from previously reported studies. These beams had either rectangular or I-shaped cross sections. All prestressed reinforcement was bonded, and most of the beams were post-tensioned. The beams failed in flexure after the prestressed reinforcement yielded.

The ultimate flexural strength predicted by strain compatibility analysis was compared with test results. The ratios of test to theoretically calculated strength ranged from 0.93 to 1.17, with an average value of 1.01 and a coefficient of variation of 0.054. After accounting for variability due to testing errors and the material and geometric properties affecting ultimate flexural strength, the coefficient of variation for P was estimated to be $COV_P = 0.035$. Mirza, Kikuchi, and MacGregor (1980) chose to use a normal distribution with $\lambda_P = 1.0$ and $COV_P = 0.035$ for the professional factor.

Ellingwood et al. (1980), referencing a preprint by Mirza, Kikuchi, and MacGregor (1980), used a normal distribution with $\lambda_P = 1.01$ and $COV_P = 0.046$ for the professional factor in all calculations involving the variability of the flexural strength of beams, combined axial load, and moment capacity of columns, including precast, prestressed components.

Nowak (1999), who conducted a reliability-based calibration for the AASHTO LRFD involving the analysis of prestressed concrete bridge girders, specified the statistical parameters for the professional factor for these structures as $\lambda_P = 1.01$ and $COV_P = 0.06$. Rakoczy and Nowak (2013) performed a sensitivity analysis focused on the reliability of prestressed concrete girder bridges. They assumed, as supported by previous studies, that the professional factor followed a normal distribution with a bias factor of $\lambda_P = 1.01$ and coefficient of variation of $COV_P = 0.06$.

5.2.1.2. Updated Statistical Models for the Fabrication Factor

As noted earlier, the statistical data for geometrical uncertainty, which has been used in previous calibrations, is as detailed in Table 5-1 and reflects the characteristics of cast-in-place concrete construction.

There are several advantageous factors associated with the fabrication of precast, prestressed concrete bridge components, including segments in segmental bridges, that reflect the improved control of dimensions and reinforcement location for this type of construction and thus contribute to the enhancement of the fabrication statistical parameters compared to cast-in-place concrete construction. In particular, the uncertainty in the cross-sectional properties of structural elements is closely linked to the tolerances maintained during concrete production and construction. The key tolerance categories affecting the fabrication factor include the tolerances of placement of prestressed reinforcement and the tolerances in cross-sectional dimensions.

In another research study (Popok et al. 2021), a comparative analysis of tolerances between cast-in-place, nonprestressed and precast, prestressed building components, such as double-tee beams and hollow-core slabs, was conducted. Table 5-3 shows the comparative ratios of dimensional tolerances for width (b), depth (h), and reinforcement position between cast-in-place and precast concrete components.

In all instances, the ratio is less than or equal to 1.0, indicating that the tolerances for precast, prestressed concrete products are equal to or tighter than those for cast-in-place concrete members. Specifically, tolerances for reinforcement placement are more stringent for components with an overall depth greater than 8 inches. Consequently, the dimensions of precast, prestressed concrete structural components are anticipated to exhibit less dimensional variation (relative to the specified values) compared to cast-in-place concrete construction. Therefore, the coefficients of

variation for width (b), depth (h), and reinforcement position (d) are expected to be lower than those reported for cast-in-place concrete construction. These considerations are fully applicable to precast, prestressed segmental bridge structures as well.

Table 5-3 Ratios between Dimensional Tolerances—Precast, Prestressed to Cast-In-Place, Nonprestressed Concrete Components (Popok et al. 2021)

Parameter	**Ratio of Tolerances (Precast/CIP)**			
	Double-Tee Beam		**Hollow-Core Slab**	
	Positive	Negative	Positive	Negative
Width (b) > 36 in.	1/4[1]	1/3[1]	NA[2]	NA[2]
Depth (h)	1/2	2/3	NA[3]	1
Reinforcement (vertical) position				
$h \leq 8$ in.	NA[4]	NA[4]	1	1
$8 < h \leq 12$ in.	NA[4]	NA[4]	2/3	2/3
$h > 12$ in.	1/2	1/2	1/2	1/2

[1] There are no double-tee beams with b < 36 in.
[2] There is no width tolerance for cast-in-place concrete slabs.
[3] There is no positive thickness tolerance for cast-in-place concrete slabs.
[4] There are no double-tee beams in this size category.

The bias factor for d of $\lambda_F = 0.99$ for beams, as shown in Table 5-1, is typical for cast-in-place construction. This value is derived from negative-moment-critical sections of structural members, where top bars might be displaced due to workers walking over the reinforcement mat during concrete placement. In contrast, precast, prestressed plants use heavy-duty steel forms continuously supported on casting beds, with strand locations precisely secured by casting bed hardware, end abutments, and the significant tension force in the strand itself. These factors contribute to better control of cross-sectional dimensions and the placement of both nonprestressed and prestressed flexural reinforcement compared to cast-in-place concrete construction. Additionally, reinforcement is better protected during concrete placement in precast plants,

eliminating concerns such as workers walking on the reinforcement. Therefore, it is reasonable to assume that the bias factor for d in precast, prestressed concrete members is very close to $\lambda_F = 1.0$.

Flexural strength is highly sensitive to d. The coefficient of variation (COV) for d of 0.04 for beams, as reported in Table 5-1 is typical for cast-in-place concrete construction. However, the COV for d in precast, prestressed members is likely much smaller due to two main reasons: (a) workers do not walk on the placed reinforcement, and (b) the stricter tolerances permitted in plant-cast production.

Consequently, it is anticipated that the statistical parameters for the fabrication factor of precast, prestressed concrete structural components, including segmental bridge structures, will demonstrate better control over cross-sectional dimensions and reinforcement placement compared to those used in reliability-based code calibrations for cast-in-place concrete. This results in a bias factor closer to 1.0 and a lower coefficient of variation. Therefore, this study assumes a coefficient of variation COV_F of 0.02, corresponding to the tolerances for strand positioning in fully precast, prestressed components. For factory-topped components, d_p is mainly influenced by the strand position since the overall depth is tightly controlled. Thus, a COV_F of 0.02 is deemed appropriate for the segmental bridge components, considered in this study. This choice aligns with the presented tolerance ratios and mirrors a similar decision by Mirza, Kikuchi, and MacGregor (1980), who "arbitrarily" selected a standard deviation for the depth of prestressing steel to be half that of nonprestressed reinforcing steel.

The same advantages of precast, prestressed concrete construction—such as the absence of worker interference and stricter tolerances in plant-cast production—apply to the coefficient of variation of the component width, b. Therefore, this study assumes the coefficient of variation for

precast, prestressed segmental bridge construction to be half that of cast-in-place construction, with a COV_F of 0.02.

5.2.1.3. Summary

Considering the parameters previously available in the literature, along with the fabrication statistical parameters refined in this study as previously described, all the statistical parameters used in the Monte Carlo simulation procedure to derive the statistical models for the nominal flexural capacity, M_n, are presented in Table 5-4. The variables are also categorized in the table based on whether they represent a material, fabrication, or professional factor.

Table 5-4 Statistical Parameters Used to Derive the Statistical Models for the Nominal Flexural Capacity, M_n

Variable	Factor Type	λ	COV	Source/Reasoning
f_{pu}	M	1.03	0.015	Nowak et al. (2005)
f'_c (for f'_c = 7 ksi)		1.13	0.115	
A_{ps}	F	1.00	0.015	Ellingwood et al. (1980)
b		1.00	0.02	Ellingwood et al. (1980), Popok et al. (2021)
d_p		1.00	0.02	
P	P	1.01	0.06	Nowak (1999), Rakoczy and Nowak (2013)

5.2.2. Shear Strength Limit State

Similar to the nominal flexural strength, the nominal shear strength (V_n) is also a complex parameter determined by following the procedure outlined in Section 3.3.2. To develop statistical models for the nominal shear strength, a Monte Carlo simulation is required. Consequently, the statistical parameters for each variable, for which values need to be randomly generated, must be established.

The parameters involved in determining the nominal shear strength procedure, which represent the material factor, *M*, are:

- f_{pc} = unfactored compressive stress in concrete after prestress losses have occurred either at the centroid of the cross section resisting transient loads or at the junction of the web and flange where the centroid lies in the flange
- f'_c = specified concrete compressive strength
- f_y = yield strength of the nonprestressed (transverse) reinforcement

The parameters representing the fabrication factor, *F*, are:

- A_v = area of transverse reinforcement within a distance *s*
- s = spacing of transverse reinforcement measured in a direction parallel to the longitudinal reinforcement
- b = width of the compression face of the member
- d_p = distance from extreme compression fiber to the centroid of prestressing tendons

Additionally, a professional factor, *P,* is incorporated into the Monte Carlo simulation process.

The following subsections describe the selection of statistical models for the parameters mentioned earlier, based on available literature, and the development of updated statistical parameters for the yield strength f_y of the reinforcing bars used for transverse reinforcement in the representative segmental bridges.

5.2.2.1. Statistical Models Available in the Literature

The statistical parameters representing the material factor have previously been addressed, except for the yield strength f_y of the reinforcing bars, which will be discussed further.

Regarding the unfactored compressive stress in concrete after prestress losses at the centroid of the cross section resisting transient loads, f_{pc}, the primary source of this compressive stress is assumed to be the compression due to the prestressing force. The development of the statistical models for the prestressing effect was discussed in Section 4.3.

The considered fabrication statistical parameters are based on the study by Ellingwood et al. (1980). The parameters specified in this study are provided in Table 5-1. The statistical parameters for the width of the compression face of the member, b, and the distance from the extreme compression fiber to the centroid of prestressing tendons, d_p, have been updated as described in Section 5.2.1.2.

For the professional factor, P, Nowak (1999) specified the statistical parameters for the shear capacity of prestressed concrete bridge girders as $\lambda_P = 1.075$ and $COV_P = 0.10$. These statistical models, however, employed a different method to determine shear strength than the one used in this study.

As mentioned in Section 3.3.2, the alternative shear design procedure for segmental bridges (AASHTO LRFD 2020 Article 5.12.5.3.8c) is utilized in the present study. This procedure aligns with the method for determining shear strength for prestressed concrete members in ACI 318-19 (2019). Ju et al. (2023) compared the shear strength of test specimens with the shear strengths calculated using this detailed ACI 318-19 (2019) method (Figure 5-3). The figure indicates that the average V_{test}/V_{calc}, which is the bias factor, λ_P, is 1.36, and COV_P = 22.4% (0.224). These parameters are used in the present study.

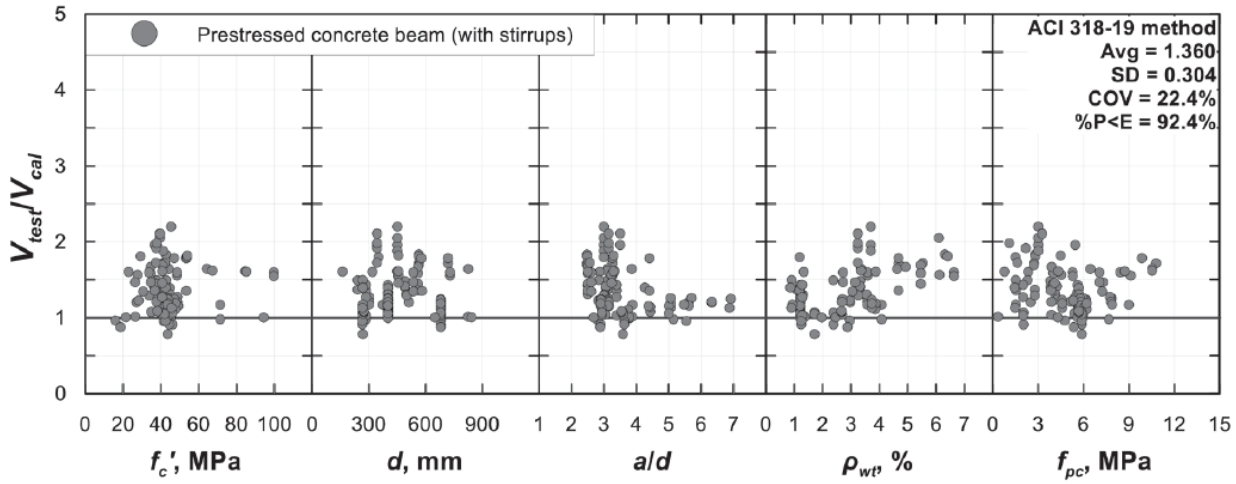

Figure 5-3 Comparison of the Shear Strength of Test Specimens with Shear Reinforcement with the Shear Strengths Calculated Using the ACI 318-19 (2019) Detailed Method (Ju et al. 2023)

5.2.2.2. Updated Statistical Parameters for Yield Strength (f_y) of Reinforcing Bars

The updated statistical parameters for the yield strength of reinforcing bars have been derived in the present study for the bar sizes No. 3 through No. 14, for steel grades 40, 75, 60, 80, and 100, and for the American Society for Testing and Materials ASTM A615 and ASTM A706 specifications, using the mill database provided by the Concrete Reinforcing Steel Institute (CRSI 2019), which contains data from 2009 through 2019.

The available bias factors derived in previous research are greater than 1.0, and their decrease (becoming closer to 1.0) is expected from the manufacturer's point of view (continuous improvement of their manufacturing process). However, from the structural reliability point of view, the decrease is undesirable as the yield strength of the steel is a part of structural resistance. It may significantly affect the limit states sensitive to steel yield strength. For the coefficients of variation, their decrease is both expected from the manufacturer's point of view and desirable from the structural reliability point of view.

ASTM A706 is a specification preferred in seismic-prone areas. Therefore, the statistical parameters for this specification are expected to be improved compared to the standard specification ASTM A615.

The statistical models for the yield strength of steel reinforcing bars have previously been derived and presented at different times. Ellingwood et al. (1980), Nowak and Szerszen (2003), Nowak et al. (2005), and Nowak, Rakoczy, and Szeliga (2012) presented the results in the form of bias factors, λ, and coefficients of variation, *COV*, for the different bar sizes for Grade 60 steel. Mander and Matamoros (2019) presented the statistical models in the form of mean values, μ, standard deviations, σ, and coefficients of variation, *COV*, for various bar sizes (ASTM A615 specification and Grade 60 steel), and mean values, μ, and coefficients of variation, *COV*, for various steel grades (ASTM A615 and ASTM A706 specifications). Mander and Matamoros (2019) also compared the mean values of the yield strength with the steel dataset available from 1997.

The CRSI Mill Database considered in this study includes more than 950,000 test results for steel bars fabricated according to different specifications, for various grades, bar sizes, and from different mills across the U.S.

Specifically, the database contains the following important variables and their categories/ranges:

- *Mill:* 33 mills across the U.S.
- *Rolling date:* 2009 to 2019
- *Bar size:* from No. 3 to No. 18
- *Specification:* ASTM A615, ASTM A706, dual A615/A706, and ASTM A1035
- *Grade:* 40, 60, 75, 80, and 100

- *Measured yield strength:* range from 40,000 psi to 100,000 psi for the majority of data
- *Method to determine yield strength:* 0.0035 EUL (extension under load), 0.2% offset, actual curve, and not indicated
- *Tensile (ultimate) strength*: range from 52,000 psi to 130,000 psi for the majority of data
- *Elongation at fracture*: range from 1.6% to 36%
- *Bar types*: different types of straight and coiled

Figure B-1 through Figure B-5 in Appendix B show histograms of the most important variables considered in this research. In Figure B-1 and Figure B-2, the *x*-axis represents the yield and tensile strength values intervals, respectively. In Figure B-3 through Figure B-5, the *x*-axis represents the categories of bar sizes, specifications, and steel grades, respectively. The *y*-axis in Figure B-1 through Figure B-5 describes the number of times the values occurred within the intervals or categories.

The data distributions shown above indicate that the prevailing reinforcing bar categories are as follows:

- yield strength of 62–74 ksi;
- tensile strength of 98–110 ksi;
- bar sizes No. 4, 5, and 6;
- specification ASTM A615;
- Grade 60 steel.

The preliminary exploratory analysis of the data indicated outliers in the yield strength values for Grade 60 bar tests for multiple bar sizes from the mill labeled Mill 304 in 2010. A possible reason for this is mistakenly mislabeling the records for Grade 40 steel as Grade 60 steel. Conversely, outliers were found in the yield strength values for Grade 40 that possibly were for

Grade 60 steel. Also, an overstrength data issue occurred in several mills for two years: 2010 and 2011. This was assumed to be a result of poor data validation processes during that period. Therefore, the data for 2009–2011 were considered unreliable, and only the range of 2012–2019 was considered for further analysis. The results of this preliminary exploratory analysis were taken into account in the present research; thus, the final sample size is 801,007 test results.

To perform the derivation, the data were first grouped by the variables relevant for the analysis. Thus, the obtained statistical parameters may be reasonably compared within the time range covered by the new dataset and corresponding previously available statistical parameters. Hence, in total, the number of sets of statistical parameters (bias factors, λ, and coefficients of variation, *COV*) for the yield strength of steel were determined for eight years (2012–2019) within each bar size (No. 3 to No. 14) for five steel grades (Grade 40, Grade 60, Grade 75, Grade 80, Grade 100) and two ASTM specifications (A615 and A706).

The obtained test data were plotted on the normal probability paper. Normal probability paper is designed to make a normally distributed variable's cumulative distribution function (CDF) appear as a straight line (Nowak and Collins 2013). It allows for an objective evaluation of the most important statistical parameters and type of distribution function. The horizontal axis represents the considered variable (in this research, steel yield strength). The vertical axis is the inverse normal probability scale, representing the distance from the mean value in terms of standard deviations. The vertical coordinate of CDF corresponds to a certain probability of exceeding the specific value.

The procedure to plot data on the normal probability paper is as follows (Nowak and Collins 2013):

1. Arrange the simulated values of Y in increasing order;

2. Associate with each value a cumulative probability, p_i, equal to:

$$p_i = \frac{i}{N+1} \tag{5-2}$$

3. For each p_i, determine the standard normal variable, z, which is the inverse of a cumulative probability: $z_i = \Phi^{-1}(p_i)$.

4. Plot the coordinates of the values vs. corresponding z_i.

An example of the CDF plotted for each considered group to derive a single set of statistical parameters (bias factors, λ, and coefficients of variation, COV) is shown on the instance of the ASTM A615 Grade 60 Bar Size No. 3 (the year 2012) group (Figure 5-4).

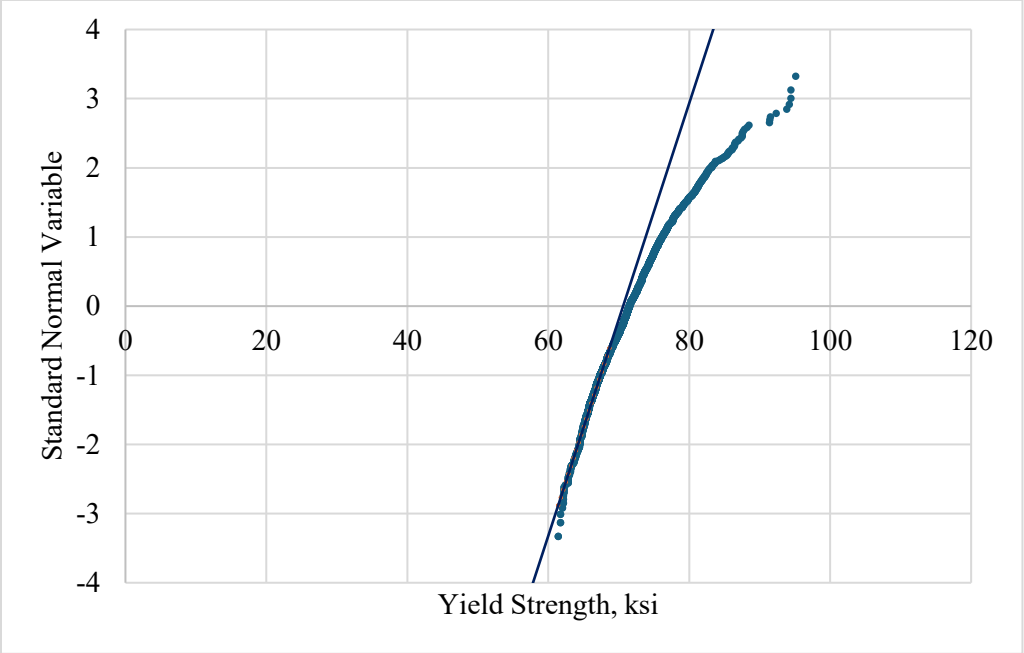

Figure 5-4 CDF for the ASTM A615 Grade 60 Bar Size No. 3 (2012) Group

For reliability analysis purposes, the lower tail of the data's cumulative distribution functions (CDF) is the most important. The yield strength of reinforcing bars represents part of the structural resistance; therefore, considering its lower data values is critical for identifying cases where demand exceeds resistance. Therefore, a single set of statistical parameters (λ and COV) for each considered group was determined for a normal distribution fitted to the lower tail of the CDF.

The normal type of distribution is assumed to be reasonable because it has been used for years in statistical derivation. Based on the engineering judgment and the experience of deriving statistical parameters from the available data, the lowest 25% of the data values were used for determining λ and *COV* for most of the data. For some cases with a smaller number of samples, the lowest 50% and 100% of the data were used accordingly to capture an adequate number of representative data.

To demonstrate the process on the example shown on Figure 5-4, the normal distribution was fitted to the lower tail of the normal probability plot (lowest 25%) of the test data, and the statistical parameters of λ = 1.18, *COV* = 0.05 were derived for this group of data. Similarly, the statistical parameters were derived for all years for ASTM A615 specification, Grade 60 steel, bar sizes No. 3 to No. 5, which are summarized in Table 5-5.

Table 5-5 shows that the ranges of the statistical parameters for the bar size No. 3 are λ = 1.15-1.20, *COV* = 0.04-0.05, for the bar size No. 4 are λ = 1.12-1.15, *COV* = 0.04, and for the bar size No. 5 are λ = 1.12-1.14, *COV* = 0.03-0.04. The number of tested samples is proportional to the total production; therefore, it can be concluded that bar sizes No. 4 and 5 are more commonly used in practice than bar size No. 3.

Based on the whole set of the derived statistical parameters, the graphs showing the evolution of the statistical parameters for every steel grade for each specification have been generated. The horizontal axis shows the years from 2012 to 2019, and the vertical axis shows the statistical parameter values (bias factor or coefficient of variation). The three different sizes of markers were used on graphs to reflect the different amounts of data used to generate them (large size is >300 samples, medium size is 100 to 300 samples, and small size is <100 samples).

Table 5-5 Statistical Parameters for ASTM A615 Grade 60 Steel (Bar Sizes No. 3 to No. 5)

Grade	Bar Size	Year	Count	λ	*COV*
Grade 60	3	2012	2,270	1.18	0.05
		2013	2,696	1.20	0.05
		2014	2,446	1.17	0.04
		2015	2,344	1.17	0.04
		2016	2,445	1.17	0.04
		2017	3,053	1.17	0.04
		2018	3,809	1.15	0.04
		2019	3,359	1.16	0.04
	4	2012	14,097	1.14	0.04
		2013	14,320	1.15	0.04
		2014	15,995	1.15	0.04
		2015	15,017	1.14	0.04
		2016	15,755	1.14	0.04
		2017	15,860	1.14	0.04
		2018	19,249	1.12	0.04
		2019	14,884	1.13	0.04
	5	2012	17,216	1.13	0.03
		2013	18,295	1.13	0.04
		2014	19,720	1.13	0.03
		2015	18,456	1.13	0.04
		2016	20,736	1.14	0.04
		2017	19,702	1.13	0.04
		2018	22,326	1.12	0.03
		2019	17,922	1.13	0.03

The presence of the clear ascending or descending trend was determined by the adequacy of *R*-squared values for the graphs. The *R*-squared values are displayed for the cases when they are adequate (the adequacy criterion is assumed as $R^2 \geq 0.5$). The bar size groups representing the change in each bar size over time for every grade were considered in this analysis. However, only the bar size groups that contained enough data to derive statistical parameters were used (51 groups in total).

The graphs showing the evolution trends of the bias factor, λ, are presented in Figure C-1 through Figure C-17 in Appendix C, and the graphs showing the evolution trends of coefficient of variation, *COV*, are presented in Figure C-18 through Figure C-34. The three different sizes of markers were used on graphs to reflect the different amounts of data used to generate them (large size is >300 samples, medium size is 100 to 300 samples, and small size is <100 samples).

The analysis of the evolution of all data indicated that the majority of data do not show a clear evolution trend of increasing (desirable from the structural reliability point of view) or decreasing the bias factor, λ, over time. Also, the majority of data do not show a clear evolution trend of increasing or decreasing (desirable from the structural reliability point of view) the coefficient of variation, *COV,* over time.

The weighted mean values of the statistical parameters of all years for each bar size for the ASTM A615 and ASTM A706 specifications are summarized in Table 5-6 and Table 5-7. The ASTM A706 specification contains data only for Grades 60 and 80 steel, which were used to conduct a comparative analysis. The blue arrows in Table 5-6, Table 5-7, and Table 5-11 indicate desirable changes in statistical parameters (in Table 5-6 and Table 5-7, this represents an improvement of the statistical parameters for ASTM A706 specification over those for ASTM A615 specification), while the red arrows indicate undesirable changes.

It can be observed that the statistical parameters for none of the bar sizes fully meet the expectations for the improved statistical parameters for ASTM A706 specification over those for ASTM A615 specification. According to these expectations, the bias factors for ASTM A706 specification should be greater than those for ASTM A615 specification, and the *COV*s for ASTM A706 should be lower. For Grade 60 steel, in most of the bar sizes, the bias factors for ASTM

A706 are greater; however, the *COV*s are also greater. For Grade 80 steel, in most of the bar sizes, the *COV*s for ASTM A706 are lower; however, the bias factors are also lower.

The derived statistical parameters for ASTM A615 Grades 40, 75, and 100 are listed in Table 5-8, Table 5-9, and Table 5-10.

Table 5-6 Statistical Parameters for the ASTM A615 and ASTM A706 Specifications (Grade 60 Steel)

Bar size	**No. of samples**		**Bias factor λ**		***COV***	
	A615	**A706**	**A615**	**A706**	**A615**	**A706**
No. 3	22,422	577	1.17	1.13 ↓	0.04	0.05 ↑
No. 4	125,177	12,232	1.14	1.14	0.04	0.05 ↑
No. 5	154,373	19,578	1.13	1.14 ↑	0.04	0.04
No. 6	98,465	15,026	1.13	1.17 ↑	0.04	0.05 ↑
No. 7	39,638	6,955	1.14	1.18 ↑	0.04	0.05 ↑
No. 8	48,821	6,945	1.14	1.17 ↑	0.04	0.05 ↑
No. 9	32,496	5,913	1.14	1.18 ↑	0.04	0.05 ↑
No. 10	22,360	4,633	1.17	1.17	0.04	0.04
No. 11	28,908	6,759	1.16	1.18 ↑	0.04	0.05 ↑
No. 14	1,911	1,116	1.18	1.14 ↓	0.04	0.04

Table 5-7 Statistical Parameters for the ASTM A615 and ASTM A706 Specifications (Grade 80 Steel)

Bar size	**No. of samples**		**Bias factor λ**		***COV***	
	A615	**A706**	**A615**	**A706**	**A615**	**A706**
No. 3	7	No data	1.07	-	0.03	-
No. 4	128	121	1.12	1.10 ↓	0.04	0.04
No. 5	557	302	1.14	1.10 ↓	0.06	0.04 ↓
No. 6	390	183	1.14	1.12 ↓	0.06	0.04 ↓
No. 7	252	133	1.16	1.12 ↓	0.07	0.04 ↓
No. 8	340	263	1.14	1.10 ↓	0.07	0.04 ↓
No. 9	547	231	1.14	1.10 ↓	0.05	0.04 ↓
No. 10	454	283	1.13	1.10 ↓	0.05	0.05
No. 11	1234	773	1.11	1.10 ↓	0.04	0.04
No. 14	31	128	1.10	1.09 ↓	0.07	0.04 ↓

Table 5-8 Statistical Parameters for ASTM A615 Specification (Grade 40 Steel)

Bar size	No. of samples	Bias factor λ	*COV*
No. 3	5,757	1.34	0.07
No. 4	16,738	1.26	0.07
No. 5	4,602	1.33	0.09
No. 6	3,623	1.29	0.04

Table 5-9 Statistical Parameters for ASTM A615 Specification (Grade 75 Steel)

Bar size	No. of samples	Bias factor λ	*COV*
No. 4	262	1.17	0.07
No. 5	870	1.16	0.05
No. 6	1,554	1.13	0.05
No. 7	1,905	1.13	0.05
No. 8	3,072	1.12	0.04
No. 9	3,700	1.12	0.04
No. 10	4,669	1.09	0.04
No. 11	10,404	1.10	0.04
No. 14	606	1.11	0.05

Table 5-10 Statistical Parameters for ASTM A615 Specification (Grade 100 Steel)

Bar size	No. of samples	Bias factor λ	*COV*
No. 4	9	1.06	0.02
No. 5	36	1.07	0.05
No. 6	12	1.04	0.02
No. 7	13	1.06	0.04
No. 8	28	1.08	0.04
No. 9	7	1.04	0.03
No. 10	24	1.07	0.04
No. 11	146	1.07	0.04
No. 14	18	1.09	0.07

The weighted mean values of the statistical parameters of all years for each bar size (Grade 60 Steel) for the ASTM A615 specification vs. previously available statistical parameters (2001-04) for the same grade (Nowak et al. 2005; Nowak, Rakoczy, and Szeliga 2012) are summarized in Table 5-11.

The results show that the statistical parameters for none of the bar sizes fully meet the improvement expectations, according to which the updated bias factors are greater compared to the previously available ones and the updated *COV*s are lower. For most of the bar sizes, the updated bias factors are greater; however, the *COV*s are also greater.

Table 5-11 Statistical Parameters for ASTM A615 Grade 60 Steel (Updated) vs. Previously Available Statistical Parameters

Bar size	**No. of samples**		**Bias factor λ**		***COV***	
	Previous	**Updated**	**Previous**	**Updated**	**Previous**	**Updated**
No. 3	864	22,422	1.18	1.17 ↓	0.04	0.04
No. 4	2,685	125,177	1.13	1.14 ↑	0.03	0.04 ↑
No. 5	3,722	154,373	1.12	1.13 ↑	0.02	0.04 ↑
No. 6	1,455	98,465	1.12	1.13 ↑	0.02	0.04 ↑
No. 7	1,607	39,638	1.14	1.14	0.03	0.04 ↑
No. 8	1,446	48,821	1.13	1.14 ↑	0.025	0.04 ↑
No. 9	1,573	32,496	1.14	1.14	0.02	0.04 ↑
No. 10	1,089	22,360	1.13	1.17 ↑	0.02	0.04 ↑
No. 11	1,316	28,908	1.13	1.16 ↑	0.02	0.04 ↑
No. 14	12	1,911	1.14	1.18 ↑	0.02	0.04 ↑

Therefore, the statistical parameters for reinforcing steel have changed over time, and the updated parameters are listed in Table 5-6, Table 5-7, Table 5-8, Table 5-9, and Table 5-10, and are recommended for further use. The parameters are recommended specifically to the considered specifications, which was unavailable in past research before this contribution. Another study by Aguilar et al. (2024) provided and utilized a portion of these statistical results in the calibration of the shear strength reduction (resistance) factor.

For the present reliability analysis study, the statistical parameters for the yield strength of the transverse reinforcement, f_y, in the segmental bridge cross sections were used such as the updated parameters in Table 5-11 for the corresponding bar sizes No. 3, No. 4, and No. 5.

5.2.2.3. Summary

Considering the parameters previously available in the literature, along with the updated statistical parameters for the yield strength of the transverse reinforcing bars, f_y, as previously described, all the statistical parameters used in the Monte Carlo simulation procedure to derive the statistical models for the nominal shear capacity, V_n, are presented in Table 5-12. The variables are also categorized in the table based on whether they represent a material, fabrication, or professional factor.

Table 5-12 Statistical Parameters Used to Derive the Statistical Models for the Nominal Shear Capacity, V_n

Variable	**Factor Type**	λ	***COV***	**Source/Reasoning**
f_{pc}	*M*	1.25	0.05	Grouni and Nowak (1984), modified based on the present study
f'_c (7 ksi)		1.13	0.115	Nowak et al. (2005)
f_y (bar size 5, Grade 60)		1.13	0.04	Derivation from CRSI Mill Database – result of the present study, Aguilar et al. (2024)
A_v	*F*	1.00	0.015	Ellingwood et al. (1980)
s		1.00	0.04	
b		1.00	0.02	Ellingwood et al. (1980), updated in the present study
d_p		1.00	0.02	
P	*P*	1.36	0.224	Ju et al. (2023)

6. RELIABILITY-BASED CALIBRATION RESULTS

6.1. Application of Reliability Analysis

The reliability analysis procedure described in Chapter 3, utilizing the statistical parameters of load and resistance components developed in Chapter 4 and Chapter 5, was applied to the set of representative bridges described in Section 2.2.

The nominal load and resistance components were determined through finite-element modeling, including the use of Midas Civil software. For the strength limit states, λ_R and COV_R were determined using the Monte Carlo simulation. With all nominal values, bias factors, and coefficients of variation established, the mean values and standard deviations were determined using Equation (4-1) as follows:

$$\lambda_x = \frac{mean}{nominal} = \frac{\mu_x}{X}$$

$$COV_x = \frac{\sigma_x}{\mu_x}$$

$$\rightarrow \ \mu_x = X \cdot \lambda$$

$$\sigma_x = \mu_x \cdot COV_x$$

Then, all the computed mean values and standard deviations of load and resistance components were used in Equation (3-1), repeated below for convenience, to compute the reliability indices. This equation is expanded for the considered limit states into the equations described in Section 3.2, which will also be repeated in the following sections for convenience.

$$\beta = \frac{m_R - m_Q}{\sqrt{\sigma_R^2 + \sigma_Q^2}} \tag{3-1}$$

The reliability indices were computed at the locations of segment joints along the entire bridge length in both the top and bottom fibers. Subsequently, the minimum (most critical) reliability indices, β_{min}, along the length of the bridge were determined.

The following sections present the results of the reliability analysis in the form of reliability indices computed for a set of representative bridges across all four considered limit states.

6.1.1. Service Flexure Limit State

Equation (3-2) was used to determine the reliability indices for the service flexure limit state, as follows:

$$\beta = \frac{\mu_{fR} - \mu_{fDC} - \mu_{fDW} - \mu_{fPS} - \mu_{fCRSH} - \mu_{fTU} - \mu_{fTG} - \mu_{fLL}}{\sqrt{\sigma_{fR}^2 + \sigma_{fDC}^2 + \sigma_{fDW}^2 + \sigma_{fPS}^2 + \sigma_{fCRSH}^2 + \sigma_{fTU}^2 + \sigma_{fTG}^2 + \sigma_{fLL}^2}}$$

The reliability indices for this limit state were computed at the locations of segment joints in both the top and bottom fibers along the bridge length. The values of β_{min} for the top and bottom fibers in the considered representative bridges are presented in Table 6-1.

Figure 6-1 illustrates the critical locations (with β_{min}) for the service flexure limit state for the three Midas examples, representative of the three main construction methods. As is known, the critical location for maximum normal flexural stress for the bottom fiber is typically in the midspan region. Therefore, this is the corresponding location of β_{min} in the bottom fiber for bridges with constant depth throughout their length. For the top fiber, the critical location for maximum normal flexural stress in bridges with constant depth is typically at the internal support regions due to the continuity effect. However, the exact location depends on the balance of dead and live load stresses and the prestressing, which are the major contributing components.

Table 6-1 Computed Minimum Reliability Indices in the Representative Bridges (Service Flexure Limit State)

Designation/Name	**β_{min} in Bottom Fiber**	**β_{min} in Top Fiber**
Midas Example 1 (Span-by-Span)	1.95	5.01
Midas Example 2 (Balanced Cant.)	2.32	2.87
Midas Example 3 (Incremental Launching)	4.44	6.35
F-07-AL, CO (Span-by-Span)	0.59	5.34
Ernest Lyons Bridge (Span-by-Span)	3.30	5.00
Garcon Point Bridge - Main Unit (Balanced Cant.)	4.01	3.85
Garcon Point Bridge - Typical Unit (Span-by-Span)	4.58	5.58
Sunshine Skyway Bridge (Span-by-Span)	1.54	4.35
Foothills Bridge (Balanced Cant.)	0.99	3.95
Linn Cove Viaduct (Progressive Cant.)	6.47	6.56

For instance, in Midas Example 1 (span-by-span) bridge, the critical location of β_{min} at the bottom fiber is at midspan of an internal span (segment 27). For the top fiber, the critical location is near the internal support but not exactly at it (segment 40) (Figure 6-1), because at this location, the compressive stress due to prestressing does not balance the stresses from dead and live loads as significantly as it does at other locations. For balanced cantilever bridges, which typically have variable depth along their length, this depth variability may impact and modify these critical locations (Figure 6-1).

It can also be observed that the reliability indices in the top fiber are consistently much larger than those in the bottom fiber. This phenomenon can be explained by the effect of thermal gradient, where the stresses are always compressive at the top (Figure 4-8), regardless of the location along the bridge length, thereby positively contributing to the reliability indices.

Midas Example 1 (Span-by-Span)

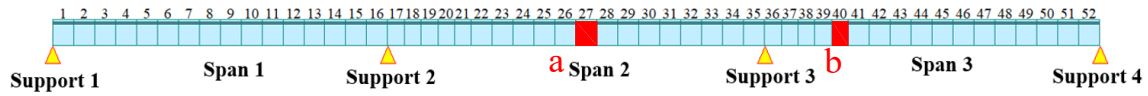

Midas Example 2 (Balanced Cantilever)

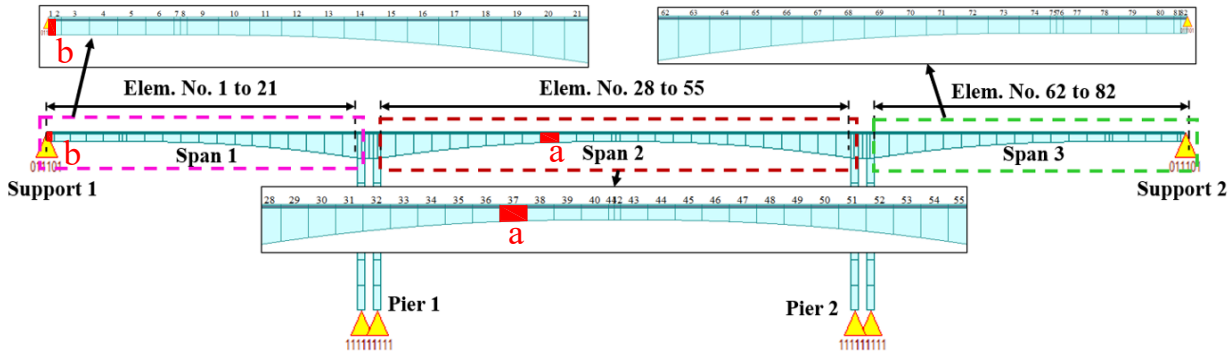

Midas Example 3 (Incremental Launching)

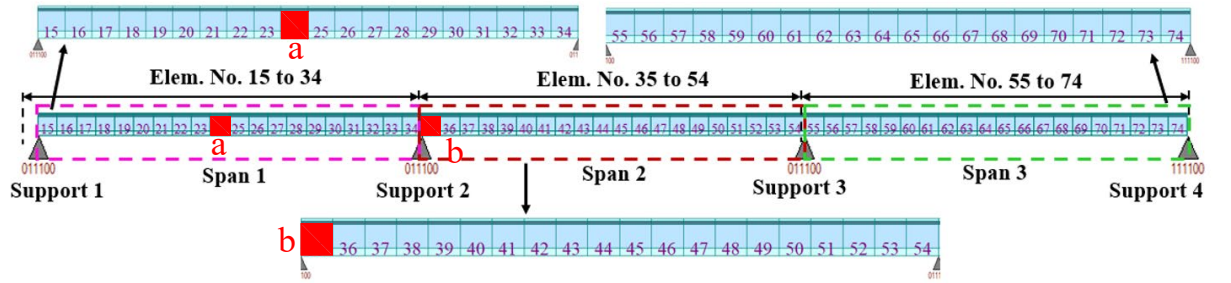

Figure 6-1 Locations of β_{min} in Midas Example Bridges for the Service Flexure Limit State: a) in the Bottom Fiber, b) in the Top Fiber

Concerning the thermal gradient, it was mentioned in Section 4.5.1 that the first design thermal gradient in the US was introduced in the AASHTO Guide Specifications (1989). Among the representative bridges, three were certainly built before this specification was introduced. Notably, two of these bridges (F-07-AL and Sunshine Skyway bridges built in 1986) exhibit lower than average reliability. This can be explained by the fact that the thermal gradient was not considered in their design, resulting in lower, albeit still satisfactory, reliability according to current standards.

6.1.2. Service Principal Tension Limit State

Equation (3-3) was used to determine the reliability indices for the service principal tension limit state, as follows:

$$\beta = \frac{\mu_{vR} - \mu_{vDC} - \mu_{vDW} - \mu_{vPS} - \mu_{vCRSH} - \mu_{vTU} - \mu_{vLL}}{\sqrt{\sigma_{vR}^2 + \sigma_{vDC}^2 + \sigma_{vDW}^2 + \sigma_{vPS}^2 + \sigma_{vCRSH}^2 + \sigma_{vTU}^2 + \sigma_{vLL}^2}}$$

Current practice generally confirms that the service flexure limit state typically provides controlling rating factors compared to the principal tension limit state. Consequently, the service flexure limit state governs. Therefore, for this and the remaining limit states, a subset of the considered representative bridges is used for the reliability calculations. The computed values of $\beta_{\min}$ are presented in Table 6-2.

Figure 6-2 illustrates the critical locations (with $\beta_{\min}$) for the service principal tension limit state for the three Midas examples. The most critical locations for the principal tension stresses are at the supports. For instance, $\beta_{\min}$ for Midas Example 1 (span-by-span) is located at the internal support (segment 36) (Figure 6-2).

Table 6-2 Computed Minimum Reliability Indices in the Representative Bridges (Service Principal Tension Limit State)

Designation/Name	$\boldsymbol{\beta_{\min}}$
Midas Example 1 (Span-by-Span)	1.00
Midas Example 2 (Balanced Cantilever)	0.62
Midas Example 3 (Incremental Launching)	1.07
F-07-AL, CO (Span-by-Span)	1.08

Midas Example 1 (Span-by-Span)

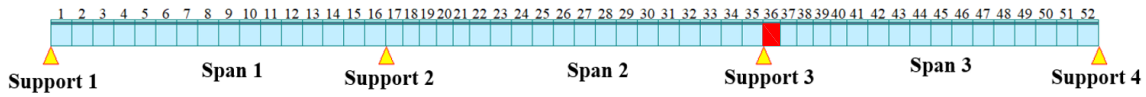

Midas Example 2 (Balanced Cantilever)

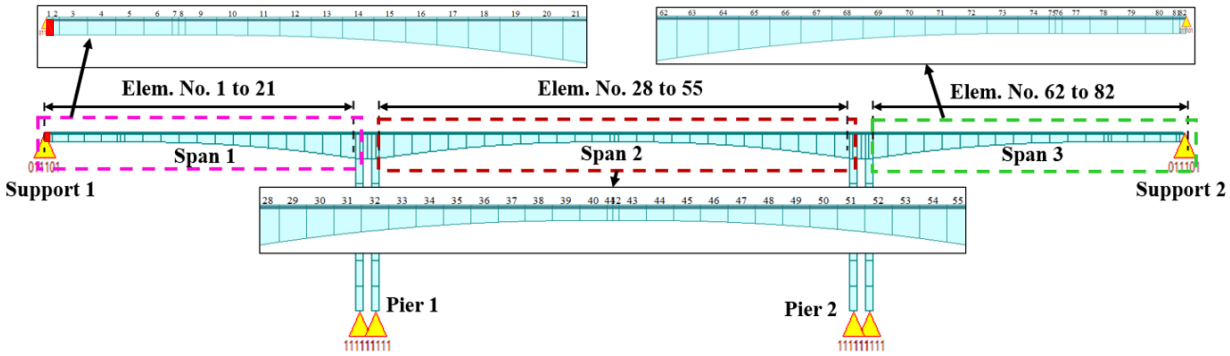

Midas Example 3 (Incremental Launching)

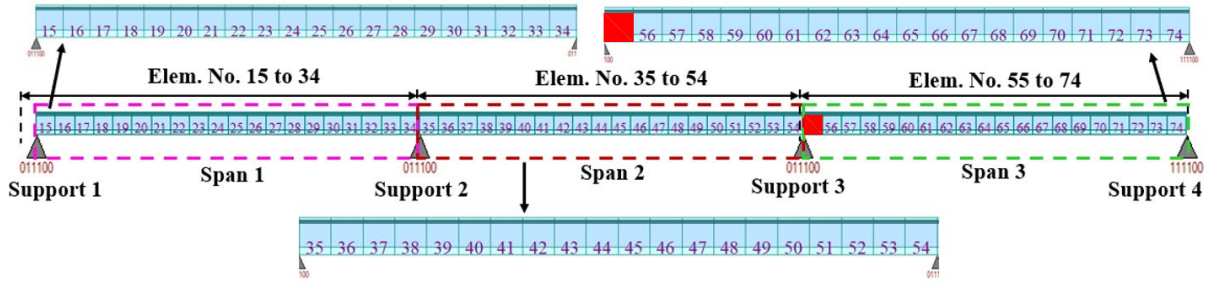

Figure 6-2 Locations of β_{min} in Midas Example Bridges for the Service Principal Tension Limit State

The results indicate that the reliability indices are within the range of those from the service flexure limit state. Given this, and the confirmation from current practice that the service flexure limit state governs, it will primarily be used for the following calibration. This also confirms that considering this subset of bridges is sufficient for the other limit states.

6.1.3. Flexural Strength Limit State

Equation (3-4) was used to determine the reliability indices for the flexural strength limit state, as follows:

$$\beta = \frac{\mu_{Mn} - \mu_{MDC} - \mu_{MDW} - \mu_{MPS} - \mu_{MCRSH} - \mu_{MLL}}{\sqrt{\sigma_{Mn}^2 + \sigma_{MDC}^2 + \sigma_{MDW}^2 + \sigma_{MPS}^2 + \sigma_{MCRSH}^2 + \sigma_{MLL}^2}}$$

The computed values of $\beta_{\min}$ for the considered representative bridges are presented in Table 6-3. Given that the objective of the present research is to conduct reliability-based calibration of load and resistance factors for the service limit state, this subset of representative bridges is deemed sufficient to perform the reliability analysis for the strength limit states.

Figure 6-3 illustrates the critical locations (with $\beta_{\min}$) for the flexural strength limit state for the three Midas examples. Depending on the location along the length of the bridge (proximity to supports or midspan), either positive or negative moments were analyzed. For instance, $\beta_{\min}$ for Midas Example 1 (span-by-span) and Example 2 (balanced cantilever) are located closer to the internal support (segment 21) and at the internal support (segment 60), respectively, both in the negative moment region (Figure 6-3). In contrast, for Example 3 (incremental launching) $\beta_{\min}$ is located in the midspan region (segment 23), which is a positive moment region) (Figure 6-3).

Table 6-3 Computed Minimum Reliability Indices in the Representative Bridges (Flexural Strength Limit State)

Designation/Name	$\boldsymbol{\beta_{\min}}$
Midas Example 1 (Span-by-Span)	4.00
Midas Example 2 (Balanced Cantilever)	8.69
Midas Example 3 (Incremental Launching)	7.88
F-07-AL, CO (Span-by-Span)	0.78

Midas Example 1 (Span-by-Span)

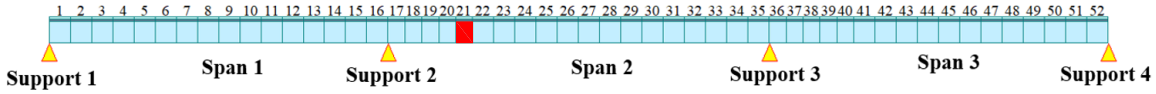

Midas Example 2 (Balanced Cantilever)

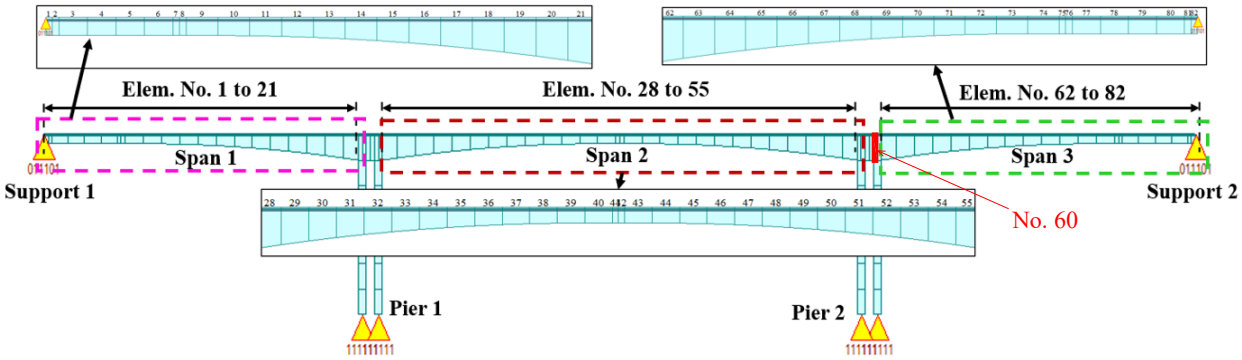

Midas Example 3 (Incremental Launching)

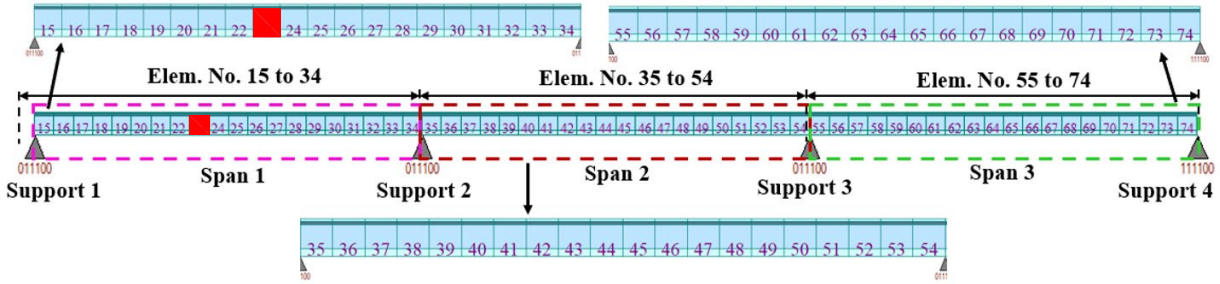

Figure 6-3 Locations of β_{min} in Midas Example Bridges for the Flexural Strength Limit State

6.1.4. Shear Strength Limit State

Equation (3-5) was used to determine the reliability indices for the shear strength limit state, as follows:

$$\beta = \frac{\mu_{Vn} - \mu_{VDC} - \mu_{VDW} - \mu_{VPS} - \mu_{VCRSH} - \mu_{VLL}}{\sqrt{\sigma_{Vn}^2 + \sigma_{VDC}^2 + \sigma_{VDW}^2 + \sigma_{VPS}^2 + \sigma_{VCRSH}^2 + \sigma_{VLL}^2}}$$

The computed values of β_{min} for the considered representative bridges are presented in Table 6-4. The results were computed for a single web (second column in Table 6-4). However, in the considered segmental bridge boxes, there are two webs resisting the shear force. This

redundancy allows for doubling the computed reliability indices for a cross section (third column in Table 6-4).

Table 6-4 Computed Minimum Reliability Indices in the Representative Bridges (Shear Strength Limit State)

Designation/Name	β_{min} **(one web)**	β_{min}
Midas Example 1 (Span-by-Span)	4.31	8.62
Midas Example 2 (Balanced Cantilever)	3.14	6.28
Midas Example 3 (Incremental Launching)	2.92	5.84
F-07-AL, CO (Span-by-Span)	5.37	10.7

Figure 6-4 illustrates the critical locations (with β_{min}) for the shear strength limit state for the three Midas examples. The most critical locations for the shear forces are near the supports. For instance, β_{min} for Midas Example 1 (span-by-span) and Example 3 (incremental launching) are located at the internal supports (segments 36 and 55, respectively) (Figure 6-4). β_{min} for Example 2 (balanced cantilever) is located near the support but not exactly at it, likely due to the impact of cross-sectional depth variability.

Midas Example 1 (Span-by-Span)

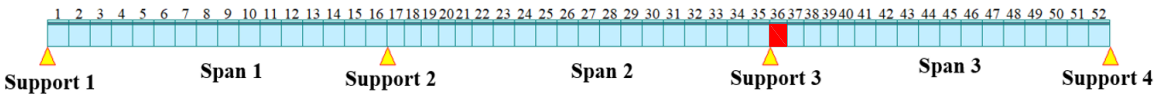

Midas Example 2 (Balanced Cantilever)

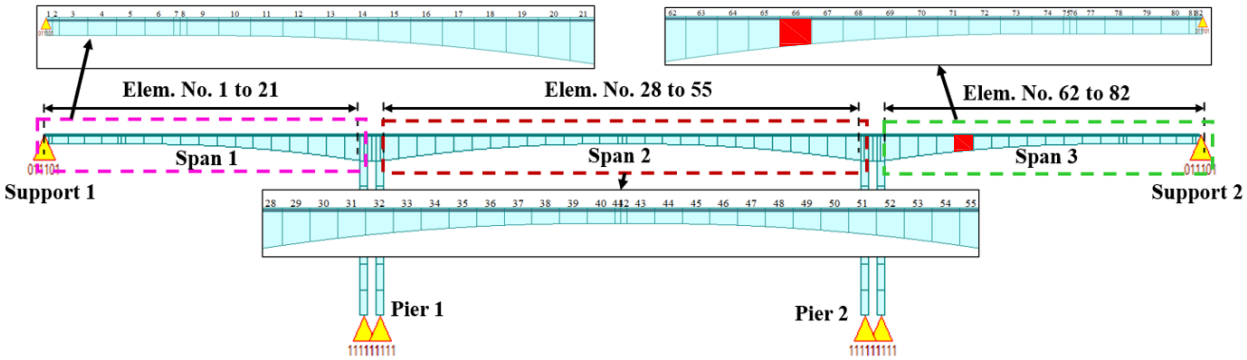

Midas Example 3 (Incremental Launching)

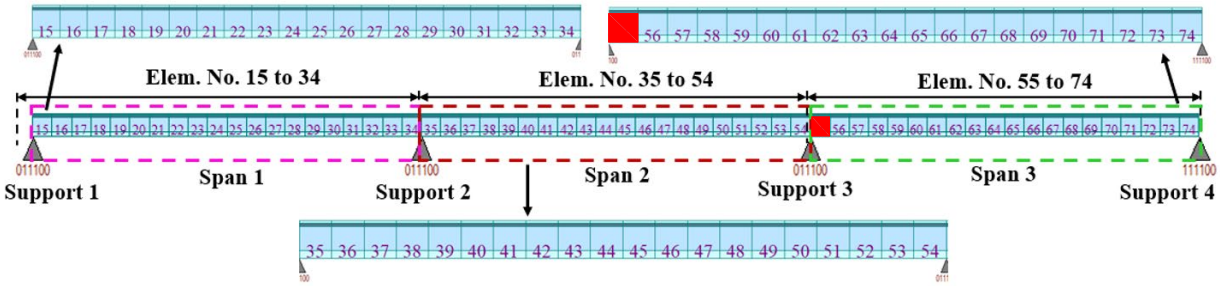

Figure 6-4 Locations of β_{min} in Midas Example Bridges for the Shear Strength Limit State

6.2. Selection of the Target Reliability Indices

The obtained reliability results serve as the basis for selecting the target reliability indices, β_T. The selection criteria for the target reliability index are as follows (Nowak and Collins 2013):

1. *Consequences of exceeding the limit state.*

The consequences of exceeding the limit state differ significantly between the service and strength limit states. Exceeding the strength limit states results in ultimate structural failure, whereas exceeding the service limit states pertains to reduced durability (e.g., due to cracking), which may worsen service conditions but not lead to failure.

The consequences of exceeding the limit state are consistent for the design and both inventory and operating ratings.

2. Cost to reduce the probability of exceeding the limit state.

Generally, the higher the cost of exceeding the limit state, the larger the target reliability index, β_T, should be (Nowak and Collins 2013). The costs associated with exceeding strength limit states are significantly higher compared to service limit states. Consequently, a higher probability of exceeding the limit state is accepted for service limit states than for strength limit states. Similarly, a higher probability of exceeding the limit state is accepted for the operating rating compared to the design or inventory rating, and less cost is involved in maintaining the condition associated with the operating rating.

Therefore, the target reliability index, β_T, is:

- Lower for service limit states than for strength limit states.
- Lower for the operating rating than for the design or inventory rating.

The target reliability indices for different limit states were selected based on the results of the reliability analysis of the existing bridges, the aforementioned criteria, and the target reliability indices for other types of bridge structures. Discussions with industrial partners confirmed that the current practices have been successful and that it is safe to select these target values of reliability indices based on the reliability index values of existing bridges. The determined target reliability indices and corresponding probabilities of exceeding the limit state are presented in Table 6-5.

For the principal tension limit state, all computed reliability indices exceed 3.0. However, since this limit state pertains to the same group of the Service III limit state as service flexure, it is acceptable to maintain the same target reliability level as the service flexure limit state. This implies that while the reliability indices for this limit state may be high, it is not necessary for them

to be exceptionally high. Therefore, for design and inventory rating, a target reliability index β_T of 1.0 is sufficient for this limit state.

Table 6-5 Target Reliability Indices

Limit State		Design/Inventory Rating		Operating Rating	
		β_T	P_f	β_T	P_f
Service	Flexure	1.0	16%	0.0	50%
	Principal Tension	1.0	16%	0.0	50%
Strength	Flexure	3.5	0.02%	2.5	0.6%
	Shear in Web	3.5	0.02%	2.5	0.6%

For the flexural strength limit state, the minimum reliability index for the F-07-AL, CO bridge is lower than the target. This can be attributed to the bridge's large span-to-height ratio (22), lower concrete compressive strength (f'_c = 5,500 psi) for a prestressed concrete structure, and the fact that it was designed in the 1980s using outdated codes. It is acceptable for some bridges to have reliability indices below the target; this does not necessarily indicate failure. The target reliability index is intended as a benchmark for new designs and load ratings.

6.3. Derivation of Load and Resistance Factors

As previously discussed, the calibration, which involves the derivation of load and resistance factors, has been completed for the service flexure limit state.

6.3.1. Striped vs. Design Lane Considerations to Include Live Load

Consideration has been given to the use of striped lanes for the operating rating as prescribed in AASHTO MBE (2018) Article 6A.5.11. The benefit of using striped lanes is questionable because there are always the same or fewer striped lanes than designed lanes. Consequently, the same or

higher multiple presence factor (MPF), accounting for the multiple presence of live load, should be applied. Applying the higher MPF diminishes the advantage of considering striped lanes. Additionally, allowing engineers to choose between striped or designed lanes introduces subjectivity. Therefore, the recommendation is to only use design lanes for design and both inventory and operating rating levels.

6.3.2. Proposed Load and Resistance Factors

The first row of Table 6-5 is targeted for the calibration, with determined target reliability indices set at β_T = 1.0 for design and inventory rating, and β_T = 0 for the operating rating. As a result of the calibration and considerations regarding striped versus designed lanes, the new load factors required for designing bridge cross sections to achieve the target reliability levels, assuming a resistance factor ϕ = 1.0, were determined as indicated in Table 6-6. For example, γ_{LL} for the operating rating was selected as 0.65, ensuring that the structure designed with this live load factor (and a resistance factor of ϕ = 1.0) achieves a reliability index corresponding to β_T = 0. The table presents both current practices and proposed provisions.

Table 6-6 Current and Proposed Design and Load Rating Provisions on Service III Limit State

	Number of Live Load Lanes (Current / Proposed)	**Target β (1-Year Return Period)**	**Live Load Factors for Service III, γ_{LL}** (Current / Proposed)
Design/ Inventory	Design Lanes / Design Lanes	β_T = 1.0	0.8 / **0.8**
Operating	Striped Lanes / Design Lanes	β_T = 0	0.8 / **0.65**

6.4. Verification of Load and Resistance Factors

To verify the derived statistical parameters, the same representative bridge database was used. The existing stress due to prestressing, f_{PSpr}, in critical sections was replaced with the required design stress, $f_{PSpr,req}$. The required prestressing stress was determined as described in Section 4.3, ultimately leading to the Equation (4-7), as follows:

$$f_{PSpr,req} = \frac{-f_{DC} - f_{DW} - f_{CRSH} - f_{TU} - \gamma_{TG} f_{TG} - \gamma_{LL} f_{LL}}{1 + \frac{f_{PSsc}}{f_{PSpr}}}$$

In this equation, γ_{LL} was taken as 0.8 for the design and inventory rating, and as 0.65 for the operating rating (Table 6-6). The reliability indices were determined for the stresses in the bottom fiber at critical midspan sections, and the resulting reliability indices are presented in Table 6-7 and on the graphs (Figure 6-5). It can be observed that the obtained reliability indices for the design/inventory rating are slightly lower than the target (β_T = 1.0) for only three bridges. Similarly, for the operating rating, the obtained reliability indices are slightly lower than the target (β_T = 0), for only two bridges. Therefore, the obtained reliability indices generally align well with the target values.

Table 6-7 Computed Minimum Reliability Indices in the Representative Bridges with f_{PSpr} required by the Design (Service Flexure Limit State)

Designation/Name	β_{min}	
	γ_{LL} = 0.8 Design/Inventory Rating	**γ_{LL} = 0.65 Operating Rating**
Midas Example 1 (Span-by-Span)	1.13	0.72
Midas Example 2 (Balanced Cant.)	0.41	-0.07
Midas Example 3 (Incremental Launching)	1.64	1.24
F-07-AL, CO (Span-by-Span)	0.78	0.25
Ernest Lyons Bridge (Span-by-Span)	1.90	1.70
Garcon Point Bridge - Main Unit (Balanced Cant.)	1.33	0.92
Garcon Point Bridge - Typical Unit (Span-by-Span)	1.63	1.20
Sunshine Skyway Bridge (Span-by-Span)	1.20	0.92
Foothills Bridge (Balanced Cant.)	0.05	-0.84
Linn Cove Viaduct (Progressive Cant.)	1.97	1.90

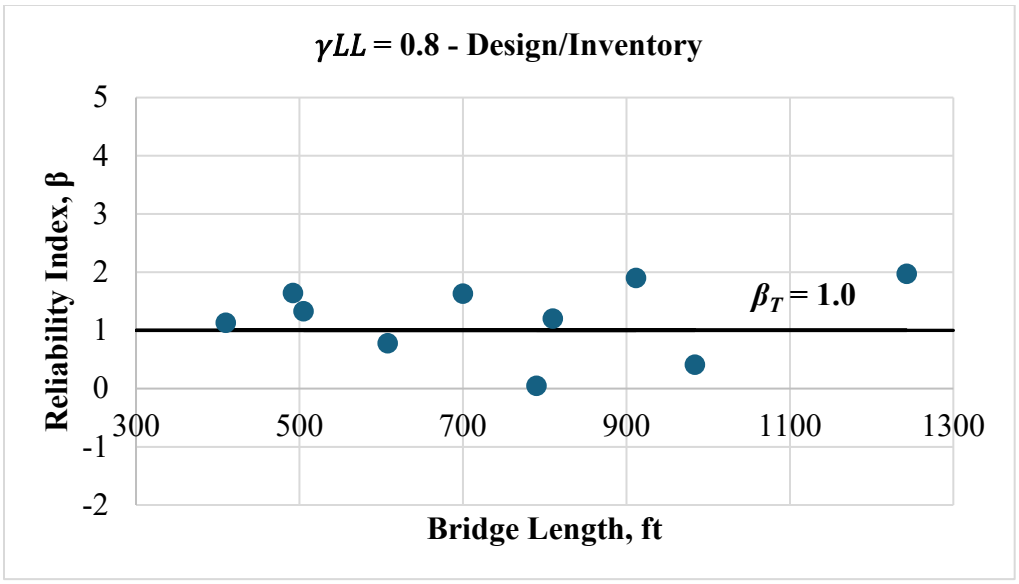

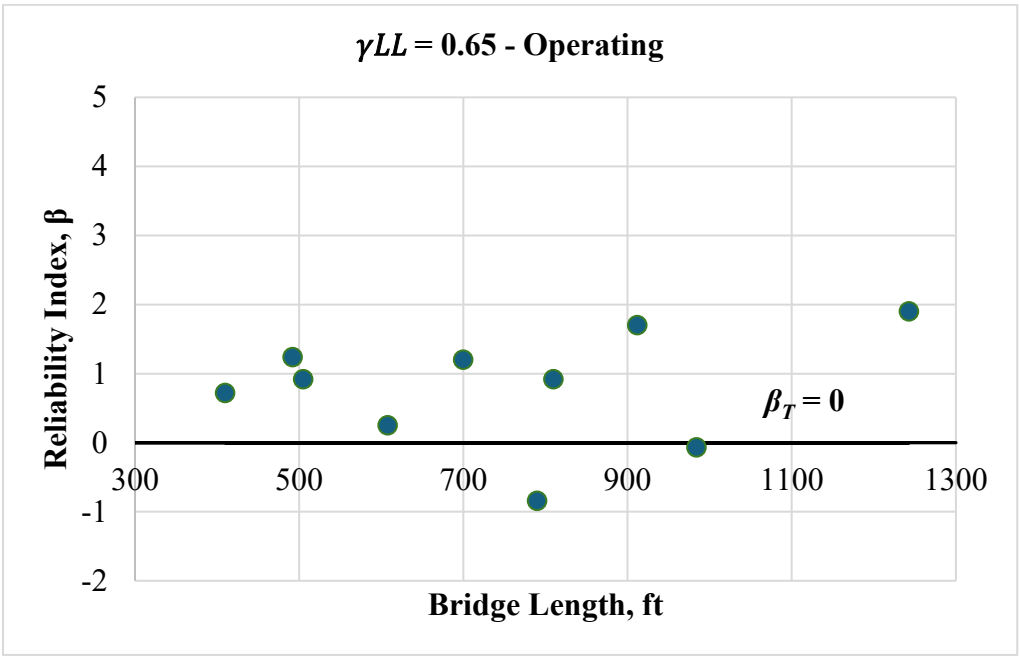

a)

Figure 6-5 Computed Minimum Reliability Indices in the Representative Bridges with f_{PSpr} required by the Design (Service Flexure Limit State): a) using γ_{LL} = 0.8 (design/inventory rating), b) using γ_{LL} = 0.65 (operating rating)

6.5. Effect of the Proposed Methodology on the Rating Factor

In addition to the proposed methodology presented in Table 6-6, refined multiple presence factors were proposed upon the completion of the NCHRP 12-123 project (Popok et al. 2024). The updated multiple presence factors, derived from recent WIM data, remain the same as those listed in AASHTO LRFD (2020) for one and two loaded lanes, but are lower for three and four loaded lanes. Table 6-8 and Table 6-9 provide a comparison between the current multiple presence factors in AASHTO LRFD (2020) and those proposed by Popok et al. (2024).

Table 6-8 Current Multiple Presence Factors (AASHTO LRFD 2020)

Number of Loaded Lanes	***m*-factor**
1	1.20
2	1.00
3	0.85
4 or more	0.65

Table 6-9 Multiple Presence Factors Proposed in Popok et al. (2024)

Number of Loaded Lanes	***m*-factor**
1	1.20
2	1.00
3	0.75
4 or more	0.60

In this section, the calculation of rating factors is demonstrated using both current and proposed methodologies, applied to the selected representative bridges.

The Ernest Lyons bridge has three design lanes and two striped lanes. The rating factor at the critical section for the service flexure limit state for this bridge is determined as follows:

$$RF = \frac{C - \gamma_{DC}DC - \gamma_{DW}DW - \gamma_{EL}EL - \gamma_{PS}PS - \gamma_{PSloss}PS_{loss} - \gamma_{CR}CR - \gamma_{TG}TG}{n \cdot m \cdot \gamma_{LL}LL}$$

where *n* is the number of loaded lanes, and *m* is the multiple presence factor.

For the inventory rating, the difference between the current and proposed methodologies lies solely in the multiple presence factor. For three lanes loaded, this factor is 0.85 under the current methodology and 0.75 under the proposed methodology. Consequently, the rating factors using the current and proposed methodology are calculated as follows (the values of the flexural stresses are in ksf):

$$RF_{inv,cur} = \frac{0 - 181.4 - 0.5 - 4.2 + 259.6 - 12.4 + 2.4 - 0.5 \cdot 13.45}{3 \cdot 0.85 \cdot 0.8 \cdot 22.1} = 1.26$$

$$RF_{inv,prop} = \frac{0 - 181.4 - 0.5 - 4.2 + 259.6 - 12.4 + 2.4 - 0.5 \cdot 13.45}{3 \cdot 0.75 \cdot 0.8 \cdot 22.1} = 1.43$$

Therefore, the rating factor calculated using the proposed methodology is 12% higher than that calculated using the current methodology.

For the operating rating, the difference would also be in using design lanes rather than striped lanes, and with a live load factor of γ_{LL} = 0.65. Additionally, Popok et al. (2024) proposed not to include the thermal gradient effect for the operating rating based on the same considerations from Corven Engineering (2004). Consequently, the rating factors using the current and proposed methodology are calculated as follows:

$$RF_{oper,cur} = \frac{0 - 181.4 - 0.5 - 4.2 + 259.6 - 12.4 + 2.4 - 0 \cdot 13.45}{2 \cdot 1 \cdot 0.8 \cdot 22.1} = 1.80$$

$$RF_{oper,prop} = \frac{0 - 181.4 - 0.5 - 4.2 + 259.6 - 12.4 + 2.4 - 0 \cdot 13.45}{3 \cdot 0.75 \cdot 0.65 \cdot 22.1} = 1.96$$

Therefore, the rating factor calculated using the proposed methodology is 9% higher than that calculated using the current methodology.

Since the changes in the proposed methodology only reflect a live load multiplier in the denominator of the rating factor equation, the percentage increases in the rating factor (12% for inventory rating and 9% for operating rating) will be applicable to all bridges with three design lanes and two striped lanes.

Another common scenario involves bridges with two design lanes and two striped lanes, such as the Foothills Bridge and Linn Cove Viaduct. In this case, there will be no change in inventory level rating factors between the current and proposed methodologies. The increase in the operating rating will correspond to the decrease in the live load factors from the current (0.8) to the proposed (0.65) methodologies, resulting in a 19% increase.

7. CONCLUSIONS AND RECOMMENDATIONS

7.1. Conclusions

In this research, reliability-based calibration was applied to determine load and resistance factors for the design and load rating of segmental bridges. A statistical analysis of segmental bridges was performed to select representative bridges. The relevant limit states were identified, and the corresponding limit state functions were formulated. The reliability analysis procedure was selected including the specifics to determine the statistical parameters of resistance for strength limit states. Statistical models of load and resistance were developed, including the estimation of statistical parameters for thermal gradient from the *TG* data for a single location, the fabrication factor for the flexural strength limit state, and the yield stress of reinforcing bars used as transverse reinforcement for the shear strength limit state. Reliability analysis was carried out for the selected representative bridges for all considered limit states. Target reliability indices were established. The load and resistance factors for the service limit state were calibrated and verified. The effect of the proposed changes on the rating factors was determined.

Based on data, assumptions, and analyses described, this study resulted in the following conclusions:

1. The live load factor varies depending on the limit state and the target reliability index. The HL-93 live load is suitable for both the design and load rating of segmental bridges.
2. For the Service III limit state, the recommended target reliability indices β_T and corresponding live load and resistance factors are as follows:
    - For the design and inventory rating, $\beta_T = 1.0$, with a corresponding live load factor of $\gamma_{LL} = 0.80$ and resistance factor of $\phi = 1.0$.

- For the operating rating, $\beta_T = 0$, with the corresponding live load factor $\gamma_{LL} = 0.65$ and resistance factor of $\phi = 1.0$.

3. The reduced live load factor substitutes striped lanes with design lanes in the operating rating of segmental bridges. Consequently, it is recommended to use design lanes for both the design and the inventory and operating ratings of segmental bridges.
4. For the strength limit states, the recommended target reliability indices β_T are:
    - For the design and inventory rating, $\beta_T = 3.5$.
    - For the operating rating, $\beta_T = 2.5$.
5. The effect of the changes in the proposed methodology of rating factors depends on the number of design and striped lanes. For common scenarios, the impact is as follows:
    - For bridges with three design lanes and two striped lanes, the rating factor increases by 12% for the inventory rating and by 9% for the operating rating.
    - For bridges with two design lanes and two striped lanes, there is no change in the rating factor for the inventory rating, while the operating rating factor increases by 19%.
6. The fabrication factor for precast, prestressed concrete components, including segmental bridge superstructure, indicates improved quality control over cross-sectional dimensions and reinforcement placement. Consequently, the bias factor, λ_F, is expected to be closer to 1.0, and a reduced coefficient of variation, COV_F, is expected compared to cast-in-place construction. Specifically, the following refined statistical parameters are recommended for the fabrication factor for the precast, prestressed concrete components: a bias factor of $\lambda = 1.00$ and a coefficient of variation of $COV = 0.02$ for both the width of the cross section, b, and the location of the prestressed reinforcement, d_p.

7. The statistical parameters for the yield strength of reinforcing steel, f_y, have changed over time, and the updated parameters listed in Table 5-6 through Table 5-10 are recommended for further use. The statistical parameters were derived for reinforing bars fabricated according to the ASTM A615 and ASTM A706 specifications.
8. The comparative analysis of the updated parameters with previously available (2001-04) statistical parameters for f_y for ASTM Grade 60 steel showed that the statistical parameters do not fully meet the improvement expectations for all of the bar sizes, according to which the updated bias factors are higher compared to the previously available bias factors and the updated coefficients of variation are lower. Particularly, for most of the bar sizes the updated bias factors are higher; however, the coefficients of variation are also higher.

7.2. Recommended Future Research

The results of this study have identified several areas that require further research. The following items are recommended for future investigation:

1. Thermal Gradient. The statistical parameters of thermal gradient require refinement. The analyses performed in this study were limited to temperature data from a single bridge location and orientation. Additionally, the updated load factor for thermal gradient, which is applied in combination with live load, needs to be calibrated using the reliability methods. This calibration should be based on a comprehensive analysis of available thermal gradient data and WIM data, as well as an investigation into the correlation between these load effects. Thermal gradient data may be highly area-specific; therefore, it is necessary to monitor different regions to gather this data.

2. Prestressing Effect in Service III Limit State. The resistance factor, ϕ_{PS}, needs to be calibrated to account for the lower reliability of the "post-2005" method for determining time-dependent prestress losses, known as "Refined Estimates of Time-Dependent Losses" in AASHTO LRFD.
3. Shear Strength Limit State: the resistance factor ϕ for the design of precast, prestressed concrete bridge structures may need refinement to account for the accuracy of as-built dimensions and reinforcement placement, as compared to cast-in-place construction.

REFERENCES

AASHTO. 1989. *Guide Specifications for Design and Construction of Segmental Concrete Bridges, 1st Edition*. Washington, DC: American Association of State Highway and Transportation Officials.

———. 1994. *AASHTO LRFD Bridge Design Specifications, 1st Ed.* Washington, DC: American Association of State Highway and Transportation Officials.

———. 1999. *Guide Specifications for Design and Construction of Segmental Concrete Bridges. 2nd Ed.* Washington, DC: American Association of State Highway and Transportation Officials.

———. 2002. *AASHTO HB-17 Standard Specifications for Highway Bridges, 17th Ed.* Washington, DC: American Association of State Highway and Transportation Officials.

———. 2010. *AASHTO LRFD Bridge Design Specifications, 5th Ed.* Washington, DC: American Association of State Highway and Transportation Officials.

———. 2018. *The Manual for Bridge Evaluation*. 3rd Edition. Washington, DC: American Association of State Highway and Transportation Officials.

———. 2020. *AASHTO LRFD Bridge Design Specifications, 9th Ed.* Washington, DC: American Association of State Highway and Transportation Officials.

ACI Committee 318. 2019. *Building Code Requirements for Structural Concrete (ACI 318-19) and Commentary (ACI 318R-19)*. Farmington Hills, MI: American Concrete Institute.

Aguilar, V., K. Popok, P. Hurtado, R. Barnes, and A. Nowak. 2024. "Reliability Evaluation of ACI 318 Strength Reduction Factor for One-Way Shear." https://www.eng.auburn.edu/files/centers/hrc/aci-crc2020p0040-final.pdf.

ASBI. 2024. “Segmental Bridge Database App.” https://asbi-assoc.org/resources/. Accessed November 29, 2024.

ASCE/SEI 7. 2002. *Minimum Design Loads for Buildings and Other Structures (ASCE/SEI 7-02)*. Reston, VA: ASCE.

ASTM International. 2002a. *ASTM A615/A615M-01b Standard Specification for Deformed and Plain Billet Steel Bars for Concrete Reinforcement*. West Conshohocken, PA: ASTM International.

———. 2002b. *ASTM A706/A706M-01 Standard Specification for Low-Alloy Steel Deformed and Plain Bars for Concrete Reinforcement*. West Conshohocken, PA: ASTM International.

Belarbi, A. 1991. *Stress-Strain Relationships of Reinforced Concrete in Biaxial Tension-Compression*. University of Houston. https://search.proquest.com/openview/a9817c6fa13cebc3979c31a1c16fdfaf/1?pq-origsite=gscholar&cbl=18750&diss=y.

Benjamin, J., and A. Cornell. 1970. *Probability, Statistics, and Decision for Civil Engineers*. New York: McGraw-Hill.

CEB-FIP. 1990. *CEB-FIP Model Code 1990: Design Code*. Lausanne, Switzerland: Thomas Telford.

CivilArc. 2024. “Box Girder.” https://civilarc.com/box-girder/. Accessed November 19. 2024.

Cooke, N., M. Priestley, and S. Thurston. 1984. “Analysis and Design of Partially Prestressed Concrete Bridges under Thermal Loading.” *PCI Journal* 29 (3): 94–114.

Cornell, C. 1969. “A Probability-Based Structural Code.” In *Journal Proceedings*, 66:974–85.

Corven Engineering, Inc. 2004. *New Directions for Florida Post-Tensioned Bridges*. Vol. 10 A: Load Rating Post-Tensioned Concrete Segmental Bridges. Tallahassee, FL.

CRSI. 2019. *Steel Mill Property Database Years 2010-2019*. Schaumburg, IL: Concrete Reinforcement and Steel Institute.

Datai Crane. 2024. "Segmental Launching Gantry Crane." https://www.dataicrane.com/products/Segmental-Launching-Gantry-Crane.html. Accessed November 19, 2024.

Elbadry, M., and A. Ghali. 1983. "Temperature Variations in Concrete Bridges." *Journal of Structural Engineering* 109 (10): 2355–74. https://doi.org/10.1061/(ASCE)0733-9445(1983)109:10(2355).

Ellingwood, B., T. Galambos, J. MacGregor, and A. Cornell. 1980. *Development of a Probability Based Load Criterion for American National Standard A58*. Vol. 13. Washington, DC: National Bureau of Standards, NBS Special Publication 577.

FHWA. 2024. "National Bridge Inventory (NBI)." https://www.fhwa.dot.gov/bridge/nbi.cfm.

Grouni, H., and A. Nowak. 1984. "Calibration of the Ontario Bridge Design Code 1983 Edition." *Canadian Journal of Civil Engineering* 11 (4): 760–70. https://doi.org/10.1139/l84-095.

Hart, G. 1982. "Uncertainty Analysis, Loads, and Safety in Structural Engineering." https://cir.nii.ac.jp/crid/1130282269001138432.

Hedegaard, B., C. French, and C. Shield. 2013. "Investigation of Thermal Gradient Effects in the I-35W St. Anthony Falls Bridge." *Journal of Bridge Engineering* 18 (9): 890–900. https://doi.org/10.1061/(ASCE)BE.1943-5592.0000438.

Hedegaard, B., C. French, C. Shield, H. Stolarski, and B. Jilk. 2013. “Instrumentation and Modeling of I-35W St. Anthony Falls Bridge.” *Journal of Bridge Engineering* 18 (6): 476–85. https://doi.org/10.1061/(ASCE)BE.1943-5592.0000384.

Huang, Dongzhou, and Bo Hu. 2020. *Concrete Segmental Bridges: Theory, Design, and Construction to AASHTO LRFD Specifications*. 1st Edition. Boca Raton: CRC Press.

Imbsen, R., D. Vandershaf, R. Schamber, and R. Nutt. 1985. “Thermal Effects in Concrete Bridge Superstructures.” National Cooperative Highway Research Report 276. National Cooperative Highway Research Program. Washington, DC: Transportation Research Board.

Ju, Hyunjin, Meirzhan Yerzhanov, Deuckhang Lee, Hyeongyeop Shin, and Thomas H.-K. Kang. 2023. “Modifications to ACI 318 Shear Design Method for Prestressed Concrete Members: Detailed Method.” *PCI Journal* 68 (1). https://www.pci.org/PCI_Docs/Publications/PCI%20Journal/2023/January-February/21-0046_Shin_JF23.pdf.

Lucko, Gunnar. 1999. “Means and Methods Analysis of a Cast-in-Place Balanced Cantilever Segmental Bridge: The Wilson Creek Bridge Case Study.” PhD Thesis, Virginia Tech. https://vtechworks.lib.vt.edu/items/7b392989-2969-4d64-923e-710634b1adb9.

MacGregor, J., S. Mirza, and B. Ellingwood. 1983. “Statistical Analysis of Resistance of Reinforced and Prestressed Concrete Members.” *ACI Journal* 80 (3): 167–76.

Maguire, M., C. Roberts-Wollmann, and T. Cousins. 2018. “Live-Load Testing and Long-Term Monitoring of the Varina-Enon Bridge: Investigating Thermal Distress.” *Journal of Bridge Engineering* 23 (3): 04018003. https://doi.org/10.1061/(ASCE)BE.1943-5592.0001200.

Mander, Thomas J., and Adolfo B. Matamoros. 2019. “Constitutive Modeling and Overstrength Factors for Reinforcing Steel.” *ACI Structural Journal* 116 (3).

MIDAS. 2021a. *Advanced Application 5: Construction Stage Analysis of a FCM Bridge Using General Functions*. MIDAS Civil.

———. 2021b. *Advanced Application 6: Construction Stage Analysis for ILM*. MIDAS Civil.

———. 2021c. *Advanced Application 19: Construction Stage Analysis for FSM (Full Staging Method) Using General Functions*. MIDAS Civil.

Mirza, S., D. Kikuchi, and J. MacGregor. 1980. “Flexural Strength Reduction Factor for Bonded Prestressed Concrete Beams.” In *Journal Proceedings*, 77:237–46.

Mirza, Sher Ali, Dennis K. Kikuchi, and James G. MacGregor. 1980. “Flexural Strength Reduction Factor for Bonded Prestressed Concrete Beams.” In *Journal Proceedings*, 77:237–46.

Moses, F. 2001. *Calibration of Load Factors for LRFR Bridge Evaluation*. Project C12-46 FY’97. https://trid.trb.org/View/692975.

Nilson, Arthur H., David Darwin, and Charles W. Dolan. 2004. *Design of Concrete Structures*. 13th Edition. Boston: McGraw-Hill Higher Education.

Nowak, A. 1999. “Calibration of LRFD Bridge Design Code.” NCHRP Report 368. Washington, D.C.: Transportation Research Board.

Nowak, A., and K. Collins. 2013. *Reliability of Structures*. 2nd edition. CRC press.

Nowak, A., and H. Grouni. 1983. “Development of Design Criteria for Transit Guideways.” In *Journal Proceedings*, 80:387–95. https://www.concrete.org/publications/internationalconcreteabstractsportal/m/details/id/10862.

———. 1986. “Serviceability Criteria in Prestressed Concrete Bridges.” In *Journal Proceedings*, 83:43–49. https://www.concrete.org/publications/internationalconcreteabstractsportal/m/details/id/1761.

Nowak, A., A. Rakoczy, and E. Szeliga. 2012. “Revised Statistical Resistance Models for R/C Structural Components.” *ACI Special Publication* 284:1–16.

Nowak, A. S., M. M. Szerszen, E. K. Szeliga, A. Szwed, and P. J. Podhorecki. 2005. “Reliability-Based Calibration for Structural Concrete.” *University of Nebraska, UNLCE*, 05–3.

Nowak, A., and M. Szerszen. 2003. “Calibration of Design Code for Buildings (ACI 318): Part 1-Statistical Models for Resistance.” *ACI Structural Journal* 100 (3): 377–82.

Popok, K., V. Aguilar, P. Hurtado, A. Nowak, R. Barnes, and A. Schindler. 2021. “Calibration of Flexural Strength Reduction Factor for Precast, Prestressed Concrete Slabs and Beams.” Precast/Prestressed Concrete Institute. Auburn, Alabama: Auburn University.

Popok, K., A. Nowak, H. Nassif, P. Lou, F. Menkulasi, C. Eamon, J. Corven, et al. 2024. “Proposed AASHTO Guideline for Load Rating of Segmental Bridges.” National Cooperative Highway Research Report 1128. National Cooperative Highway Research Program. Washington, DC: Transportation Research Board.

Potgieter, I., and W. Gamble. 1983. “Response of Highway Bridges to Nonlinear Temperature Distributions.” Civil Engineering Studies. Urbana, IL: University of Illinois at Urbana-Champain. https://trid.trb.org/View/279477.

Priestley, M. 1972. “Thermal Gradients in Bridges—Some Design Considerations.” *New Zealand Engineering* 27 (7): 228–33.

———. 1978. “Design of Concrete Bridges for Temperature Gradients.” In *Journal Proceedings*, 75:209–17. https://www.concrete.org/publications/internationalconcreteabstractsportal/m/details/id/10934.

Rakoczy, A., and A. Nowak. 2013. “Reliability-Based Sensitivity Analysis for Prestressed Concrete Girder Bridges.” *PCI Journal* 58 (4).

RePicture. 2024. “Methods of Post-Tensioned Segmental Bridge Construction.” https://www.repicture.com/project/methods-of-post-tensioned-segmental-bridge-construction. Accessed November 19, 2024.

Roberts-Wollman, C., J. Breen, and J. Cawrse. 2002. “Measurements of Thermal Gradients and Their Effects on Segmental Concrete Bridge.” *Journal of Bridge Engineering* 7 (3): 166–74. https://doi.org/10.1061/(ASCE)1084-0702(2002)7:3(166).

Shushkewich, K. 1998. “Design of Segmental Bridges for Thermal Gradient.” *PCI Journal* 43 (4): 120–37.

Sivakumar, B., M. Ghosn, and F. Moses. 2011. “Protocols for Collecting and Using Traffic Data in Bridge Design.” National Cooperative Highway Research Report 683. National Cooperative Highway Research Program. Washington, DC: Transportation Research Board.

Tadros, Maher K., Nabil Al-Omaishi, Stephen J. Seguirant, and James G. Gallt. 2003. “Prestress Losses in Pretensioned High-Strength Concrete Bridge Girders.” National Cooperative Highway Research Report 496. National Cooperative Highway Research Program. Washington, DC: Transportation Research Board.

Thompson, M., R. Davis, J. Breen, and M. Kreger. 1998. “Measured Behavior of a Curved Precast Segmental Concrete Bridge Erected by Balanced Cantilevering.” Texas. Dept. of Transportation. https://rosap.ntl.bts.gov/view/dot/42103.

Wassef, W., Kulicki, J., Nassif, H., Mertz, D., and Nowak, A. 2014. “Calibration of AASHTO LRFD Concrete Bridge Design Specifications for Serviceability.” NCHRP Web Document 201.

Wight, James K. 2015. *Reinforced Concrete: Mechanics and Design*. 7th Edition. Upper Saddle River, New Jersey: Pearson.

Yu, Z., Q. Huang, F. Li, Y. Qin, and J. Zhang. 2019. “Experimental Study on Mechanical Properties and Failure Criteria of Self-Compacting Concrete under Biaxial Tension-Compression.” *Journal of Materials in Civil Engineering* 31 (5): 04019045. https://doi.org/10.1061/(ASCE)MT.1943-5533.0002675.

Appendix A: NOTATION

A = cross-sectional area

a = depth of the equivalent stress block

A_0 = torsional area (total area enclosed by the median line of the exterior webs and slabs of the box section)

A_{ps} = area of prestressing steel

A_s = area of nonprestressed tension reinforcement

A'_s = area of compression reinforcement

A_v = area of transverse reinforcement within a distance s

b = width of the compression face of the member. For a flange section in compression, the effective width of the flange

b_v = effective web width taken as the minimum web width within the depth d_v

b_w = gross width of web, not reduced for the presence of post-tensioning ducts

C = load carrying capacity

c = distance from the extreme compression fiber to the neutral axis

COV = coefficient of variation

CR = force effects due to creep

d = $0.8h$ or the distance from the extreme compression fiber to the centroid of the prestressing reinforcement, whichever is greater

DC = dead load of structural components and nonstructural attachments

d_p = distance from extreme compression fiber to the centroid of prestressing tendons

d_s = distance from extreme compression fiber to the centroid of nonprestressed tensile reinforcement

d'_s = distance from extreme compression fiber to the centroid of compression reinforcement

d_v = effective shear depth

DW = dead load of wearing surfaces and utilities

E = concrete modulus of elasticity

EL = miscellaneous locked-in force effects resulting from the construction process, including jacking apart of cantilevers in segmental construction

F = axial force acting at the cross section; fabrication factor

f = normal flexural stress

f_1 = principal tensile stress

$f_{1,R}$ = allowable principal tensile stress

f'_c = specified concrete compressive strength

f_{pc} = unfactored compressive stress in concrete after prestress losses have occurred either at the centroid of the cross section resisting transient loads or at the junction of the web and flange where the centroid lies in the flange

f_{ps} = average stress in prestressing steel at nominal bending resistance

f_{pu} = specified tensile strength of prestressing steel

f_{py} = yield strength of prestressing steel
FR = friction load
f_R = allowable normal flexural stress specified in the LRFD code
f_s = stress in the nonprestressed tension reinforcement at nominal flexural resistance
f'_s = stress in the nonprestressed compression reinforcement at nominal flexural resistance
f_y = yield strength of the nonprestressed reinforcement
g = limit state function
h = depth of the cross section
I = moment of inertia of the cross-sectional area about the neutral axis
IM = dynamic load allowance
LL = vehicular live load
M = bending moment acting at the cross section; material factor
m = live load multiple presence factor
M = bending moment acting at the cross section
M' = distributed continuity moment in determining thermal gradient stress
M_n = nominal bending moment strength
N = number of data points
P = permanent loads other than dead loads, including prestress; professional factor
p = probability
PS = secondary forces from post-tensioning for strength limit states; total prestress forces for service limit states
PS_{pr} = primary forces from post-tensioning for service limit states
PS_{sc} = secondary forces from post-tensioning for service limit states
P_f = probability of failure / exceeding the limit state
Q = total load
Q_y = first moment of area of section above centroidal axis
R = structural resistance (load-carrying capacity)
R_R = radius of the Mohr's circle corresponding to the allowable principal stress
RF = rating factor
S = reliability
s = spacing of transverse reinforcement measured in a direction parallel to the longitudinal reinforcement
SH = force effects due to shrinkage
SLS = serviceability limit state
T = torque acting at the cross section
TG = force effect due to temperature gradient
TU = force effect due to uniform temperature
t_w = total web width perpendicular to median slope of web, at centroidal axis
$t_{(y)}$ = temperature change
ULS = ultimate limit state

V = shear force acting at the cross section
v = total shear stress at the cross section
V_c = nominal shear resistance of the concrete
V_n = nominal shear force strength
V_p = component of prestressing force in the direction of the shear force; positive if resisting the applied shear
v_R = allowable shear stress (corresponding to the allowable principal stress)
V_s = nominal shear resistance of the transverse reinforcement
v_t = shear stress from torsion
v_v = transverse shear stress
X = nominal value
y = distance from the neutral axis of the cross section to the location where the normal stress is being determined
z = standard normal variable
α = angle of inclination of transverse reinforcement to longitudinal axis; linear coefficient of thermal expansion
β = reliability index; factor indicating ability of diagonally cracked concrete to transmit tension and shear
β_1 = stress block factor
β_T = target reliability index
γ = load factor
$\gamma_{CR,SH}$ = load factor for uniform temperature, creep and shrinkage
γ_{DC} = load factor for structural components and attachments
γ_{DW} = load factor for wearing surfaces and utilities
γ_{EL} = load factor for secondary posttensioning effects and locked-in erection loads
γ_{FR} = load factor for bearing friction or frame action
γ_{LL} = live load factor
γ_P = load factor for permanent loads other than dead loads, including prestress
γ_{PS} = load factor for secondary forces from post-tensioning for strength limit states; load factor for total prestress forces for service limit states
γ_{PSpr} = load factor for primary forces from post-tensioning for service limit states
γ_{PSsc} = load factor for secondary forces from post-tensioning for service limit states
γ_{TG} = load factor for temperature gradient
γ_{TU} = load factor for uniform temperature load
δ = duct diameter correction factor, taken as 2.0 for grouted ducts
ε = longitudinal strain
ε_f = free longitudinal strain
θ = angle of inclination of diagonal compressive stresses
λ = bias factor (mean-to-nominal ratio); concrete density modification factor

λ_{duct} = shear strength reduction factor accounting for the reduction in the shear resistance provided by transverse reinforcement due to the presence of a grouted post-tensioning duct. Taken as 1.0 for ungrouted post-tensioning ducts and with a reduced web or flange width to account for the presence of ungrouted duct

μ = mean value

σ = standard deviation

Φ = standard normal cumulative distribution function (CDF)

ϕ = resistance factor

ϕ_c = condition factor

ϕ_{duct} = diameter of post-tensioning duct present in the girder web within depth d_v

ϕ_s = system factor

ψ = curvature

Appendix B: STATISTICAL ANALYSIS OF THE CRSI REINFORCING STEEL DATABASE

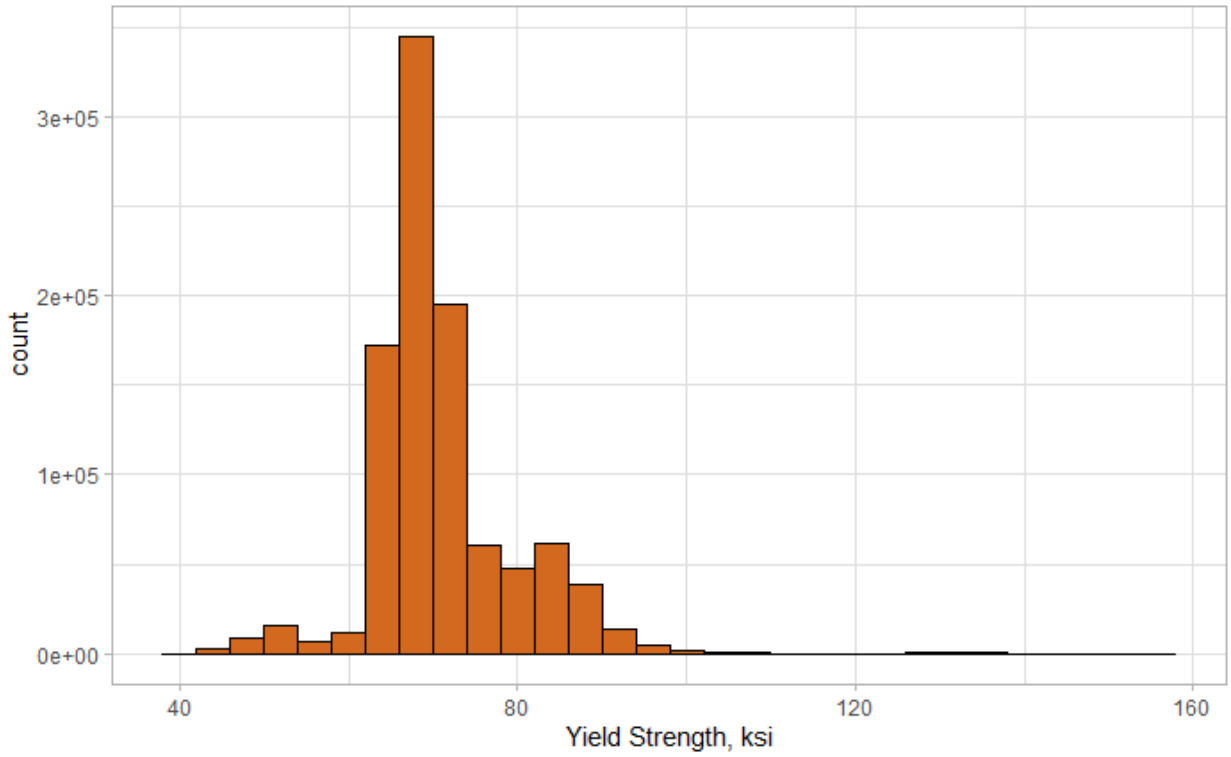

Figure B-1Yield Strength Distribution

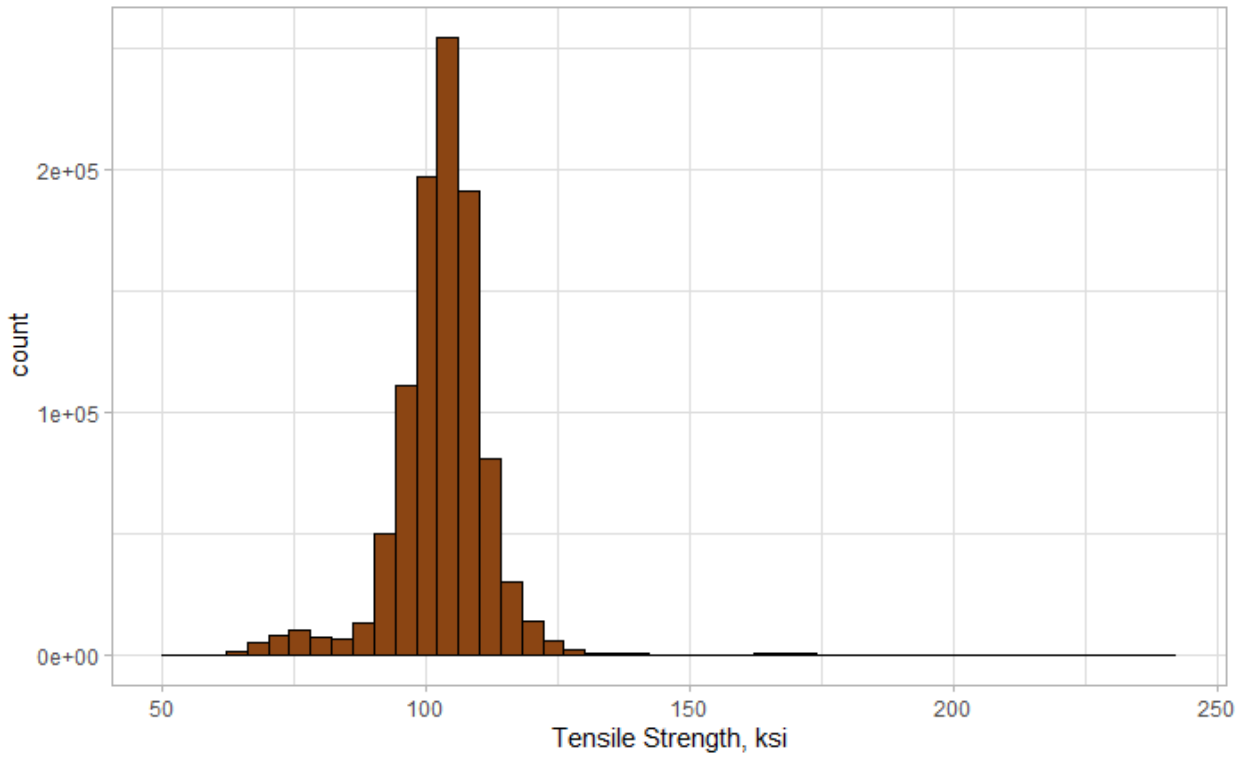

Figure B-2 Tensile Strength Distribution

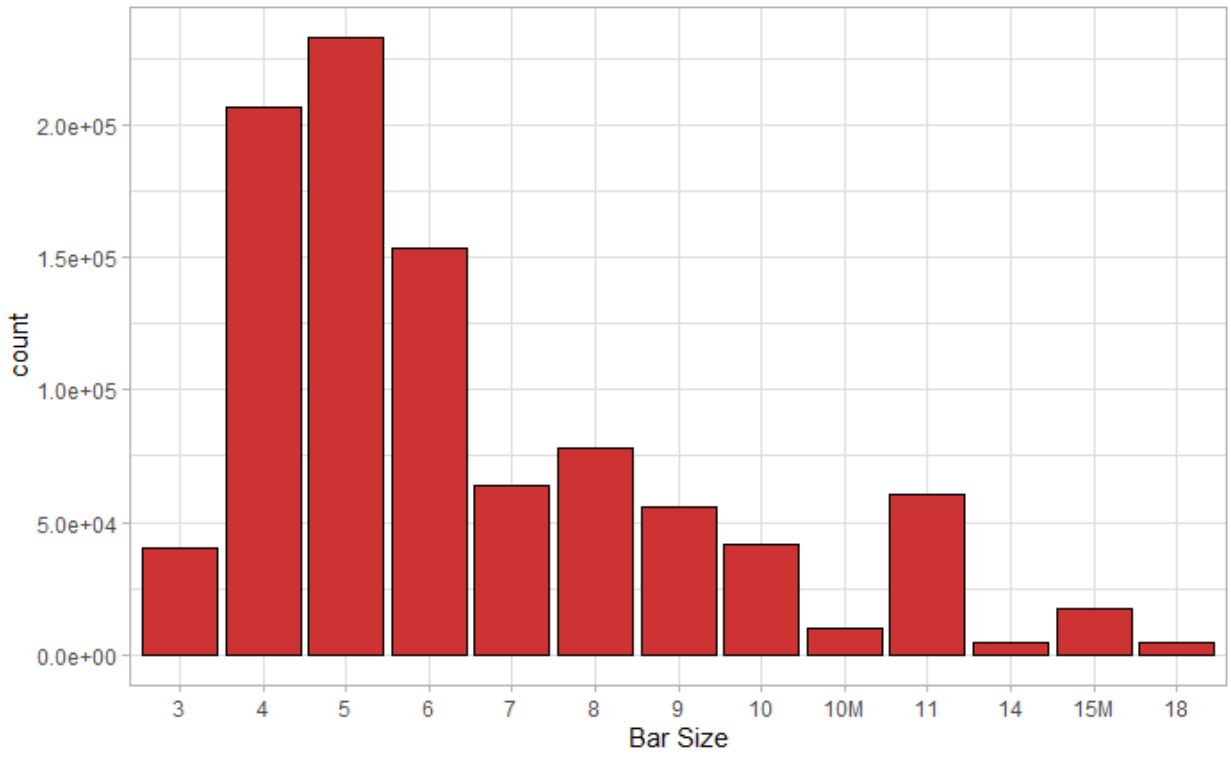

Figure B-3 Bar Size Distribution

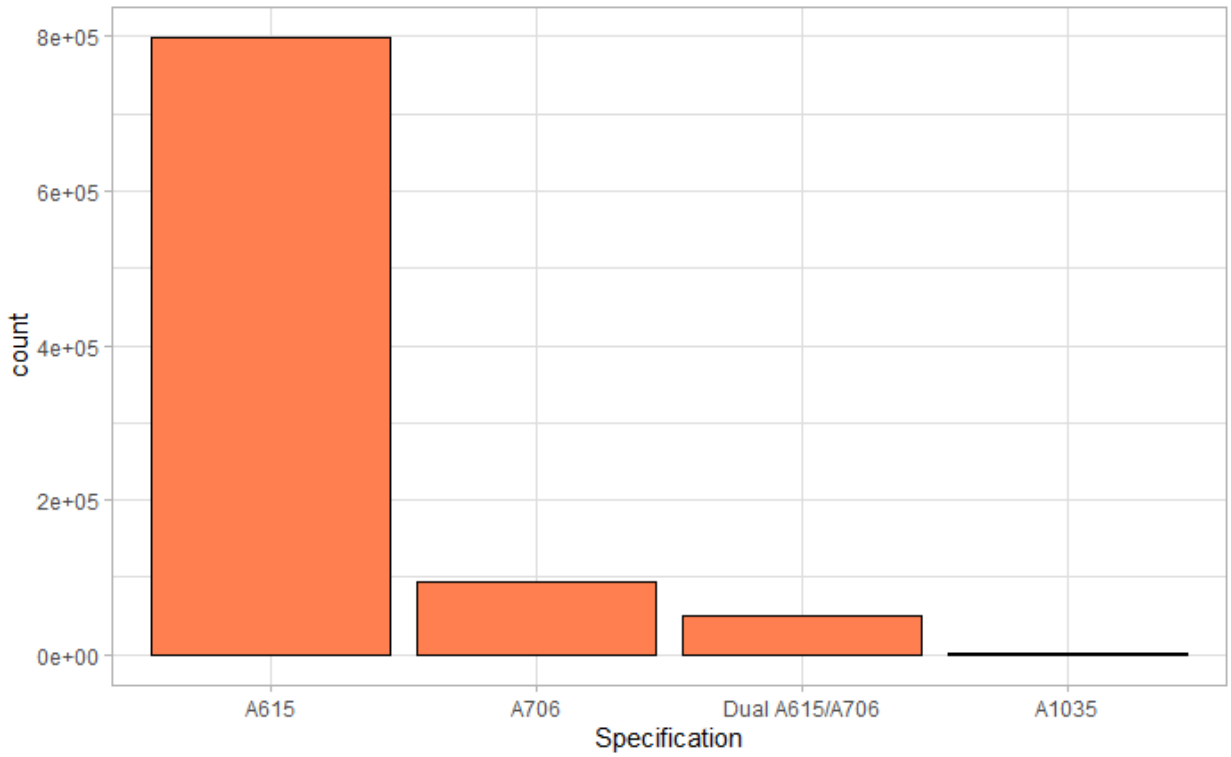

Figure B-4 Specification Distribution

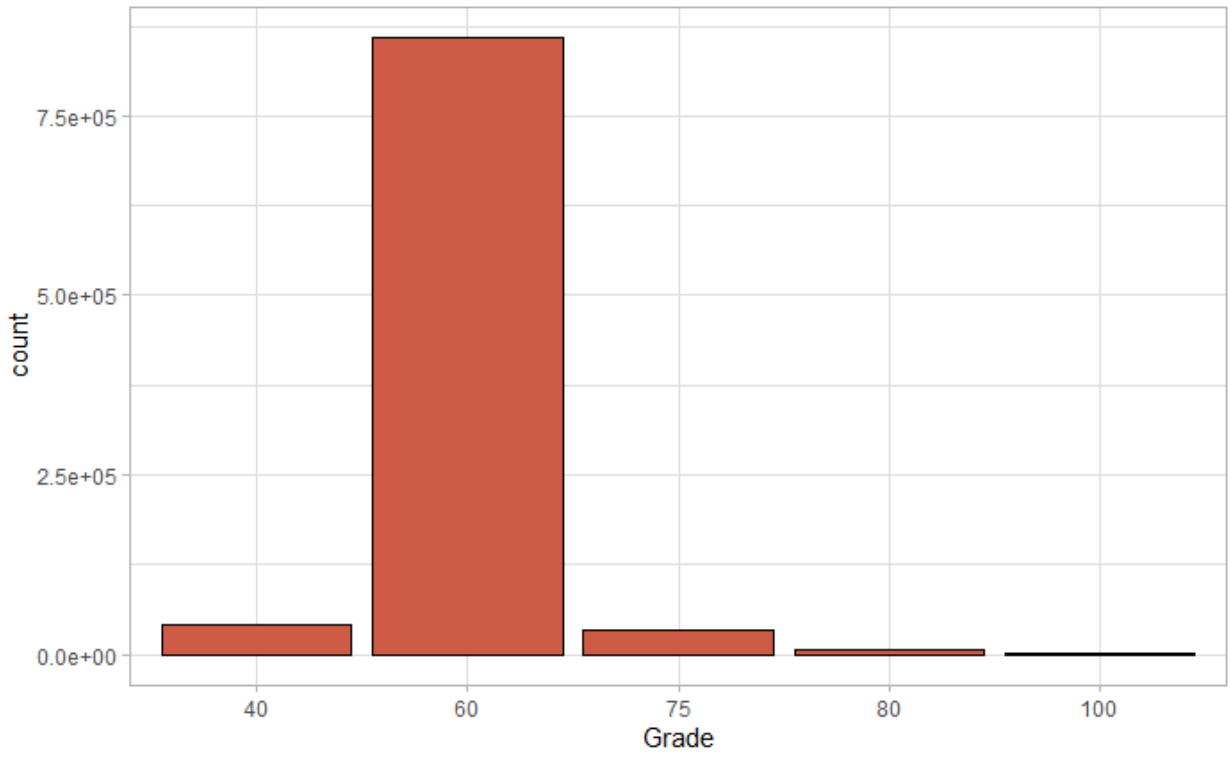

Figure B-5 Grade Distribution

Appendix C: EVOLUTION OF THE STATISTICAL PARAMETERS OF THE YIELD STRENGTH OF REINFORCING STEEL OVER TIME

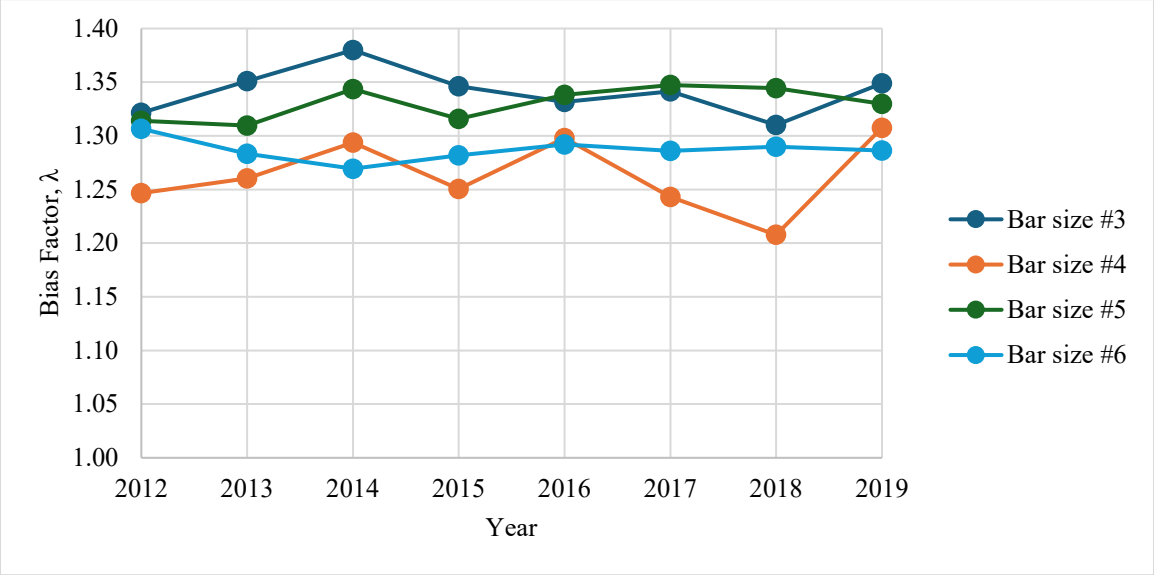

Figure C-1 Evolution Trends of the Bias Factor, λ, for the ASTM A615 Grade 40 Steel

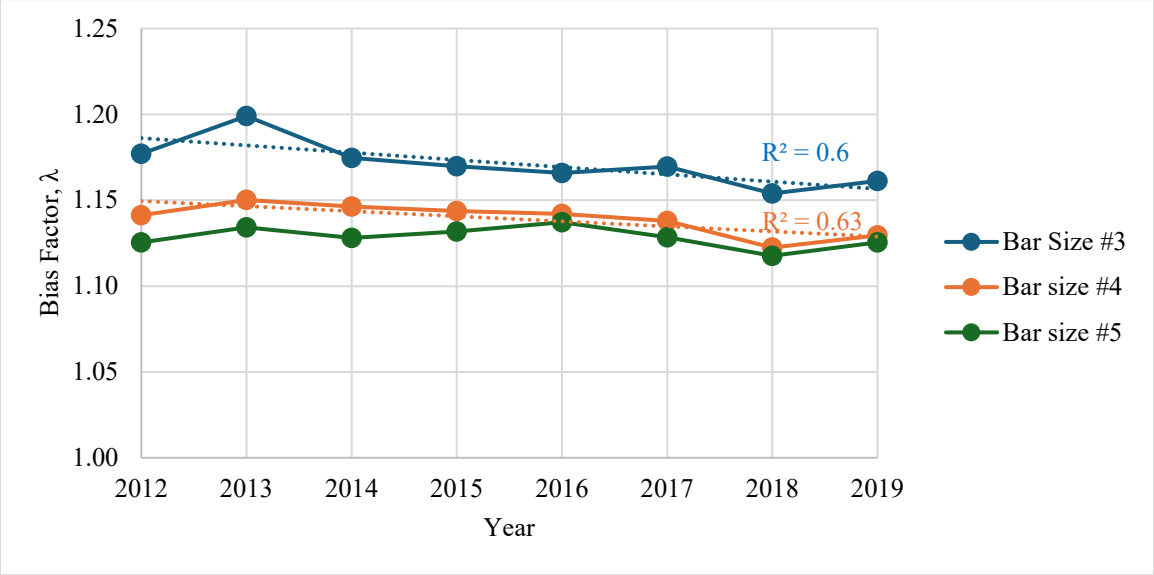

Figure C-2 Evolution Trends of the Bias Factor, λ, for the ASTM A615 Grade 60 Steel (Shear Reinforcement)

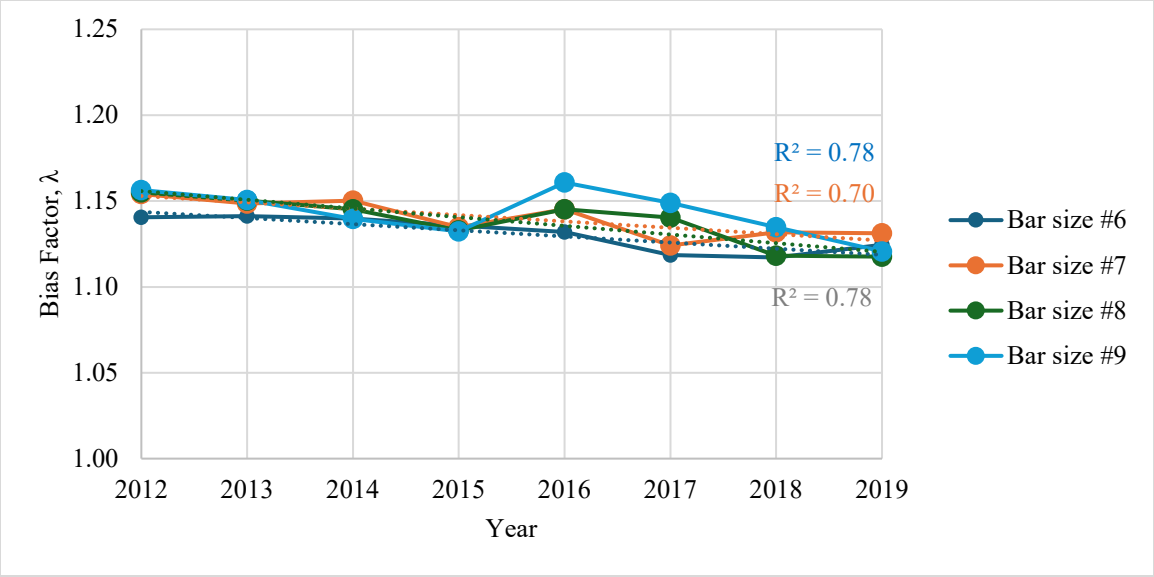

Figure C-3 Evolution Trends of the Bias Factor, λ, for the ASTM A615 Grade 60 Steel (Longitudinal Reinforcement—Common)

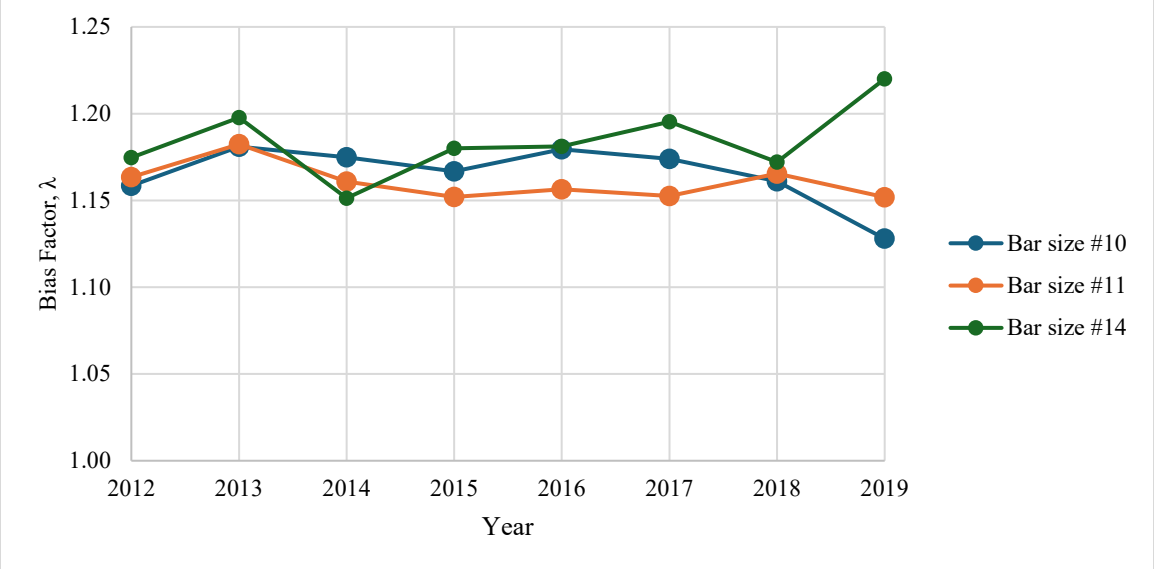

Figure C-4 Evolution Trends of the Bias Factor, λ, for the ASTM A615 Grade 60 Steel (Longitudinal Reinforcement—Large Diameters)

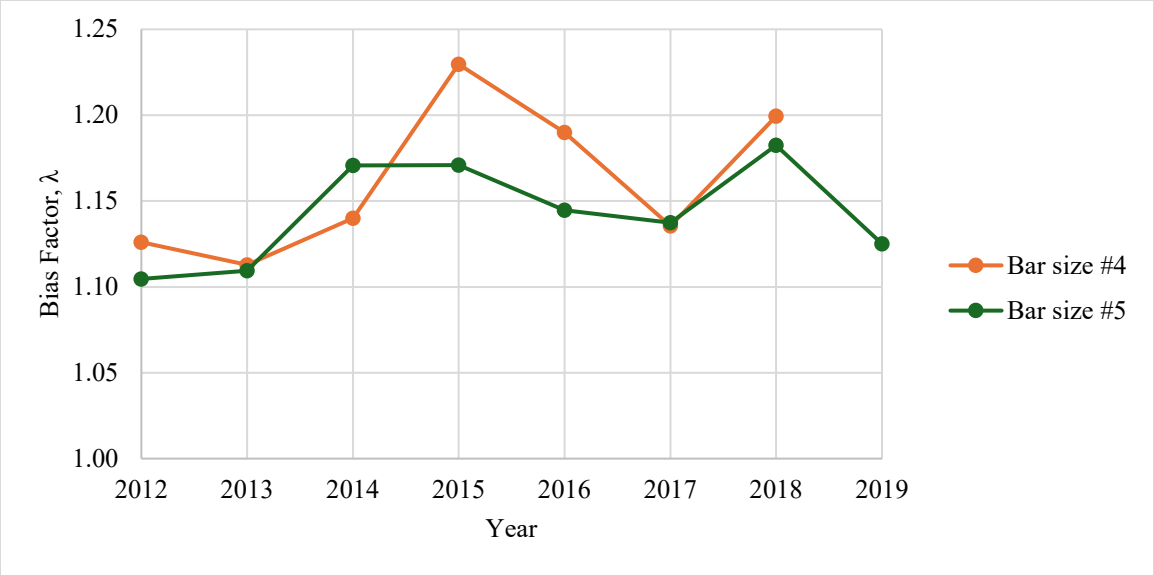

Figure C-5 Evolution Trends of the Bias Factor, λ, for the ASTM A615 Grade 75 Steel (Shear Reinforcement)

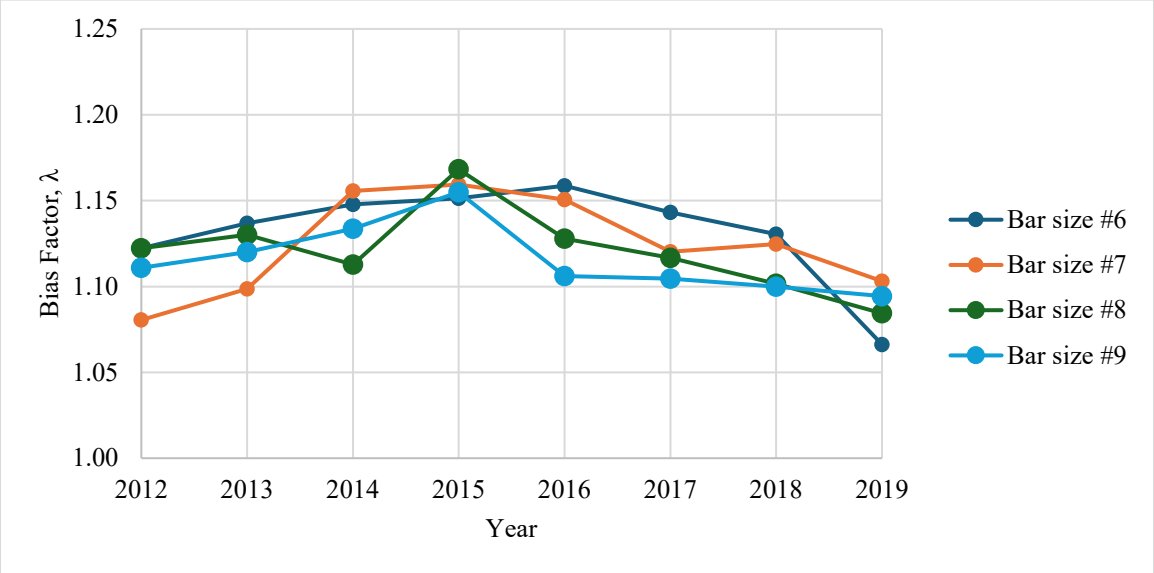

Figure C-6 Evolution Trends of the Bias Factor, λ, for the ASTM A615 Grade 75 Steel (Longitudinal Reinforcement—Common)

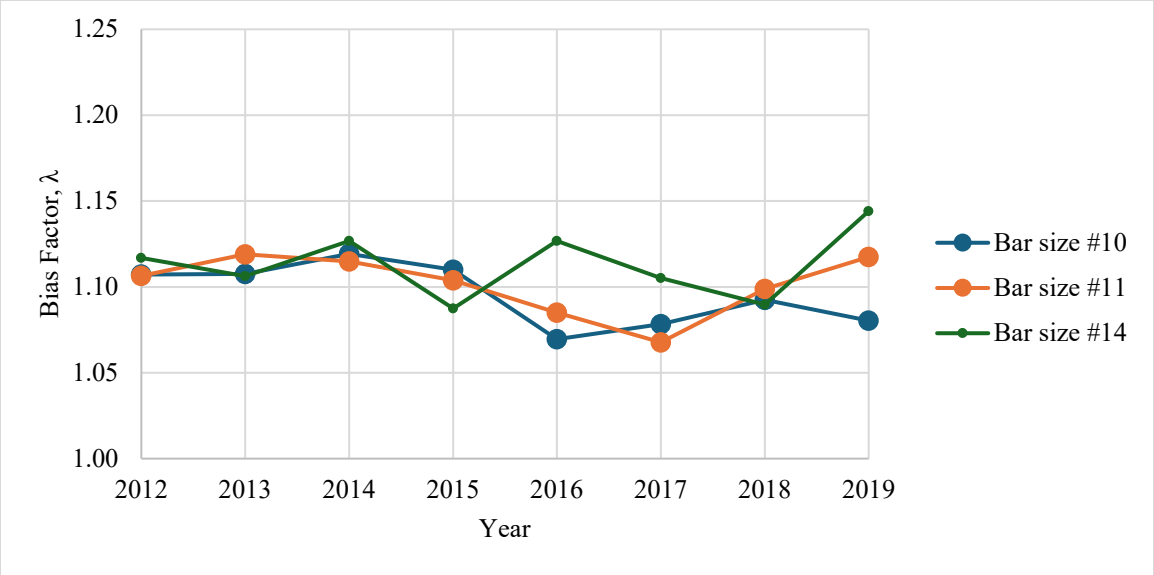

Figure C-7 Evolution Trends of the Bias Factor, λ, for the ASTM A615 Grade 75 Steel (Longitudinal Reinforcement— Large Diameters)

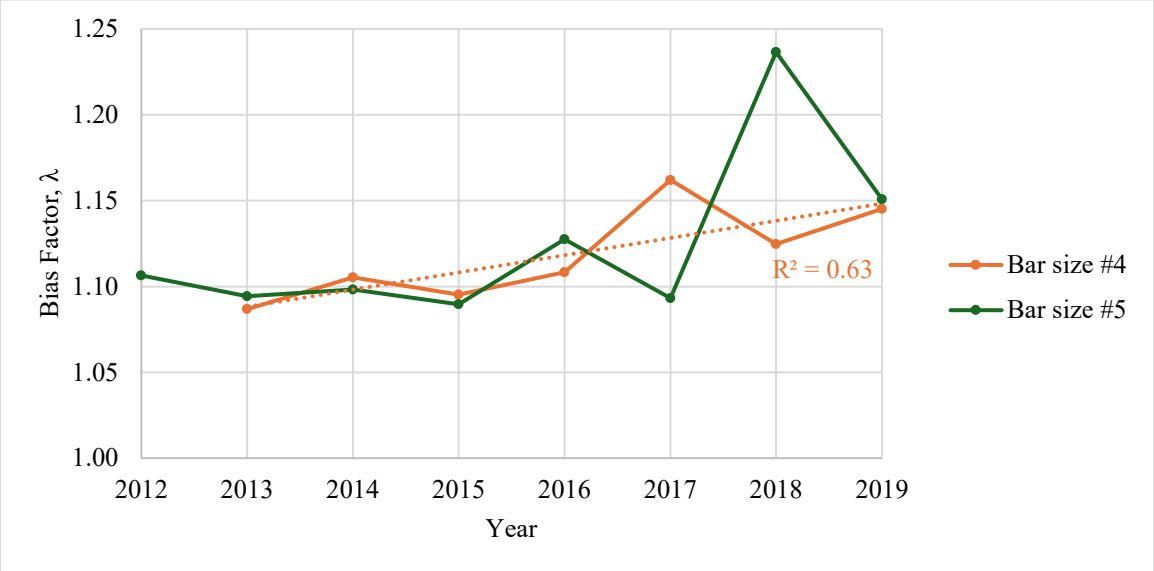

Figure C-8 Evolution Trends of the Bias Factor, λ, for the ASTM A615 Grade 80 Steel (Shear Reinforcement)

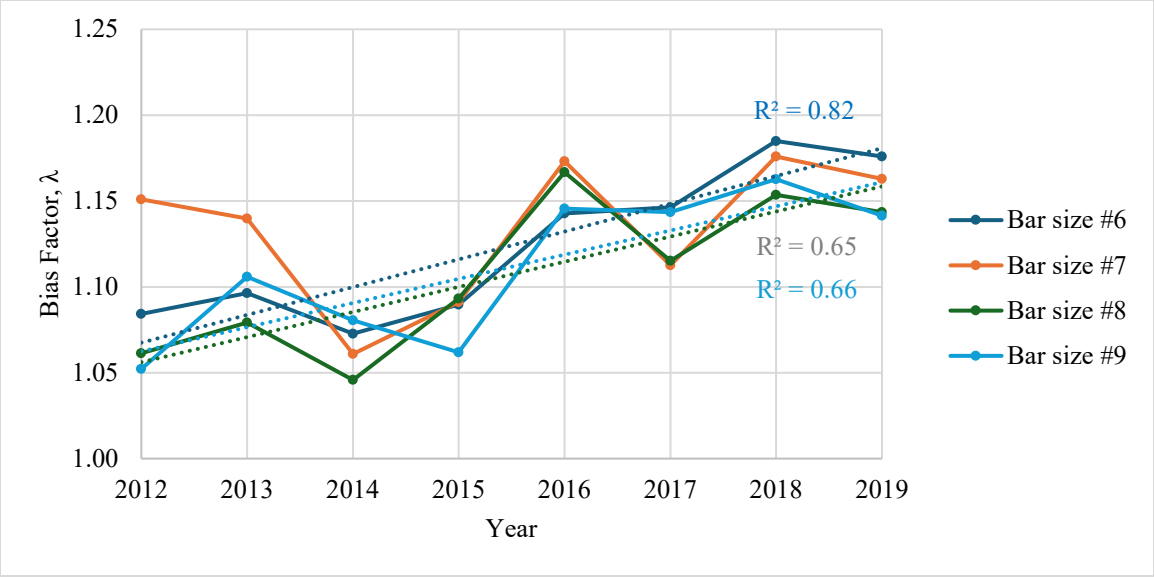

Figure C-9 Evolution Trends of the Bias Factor, λ, for the ASTM A615 Grade 80 Steel (Longitudinal Reinforcement—Common)

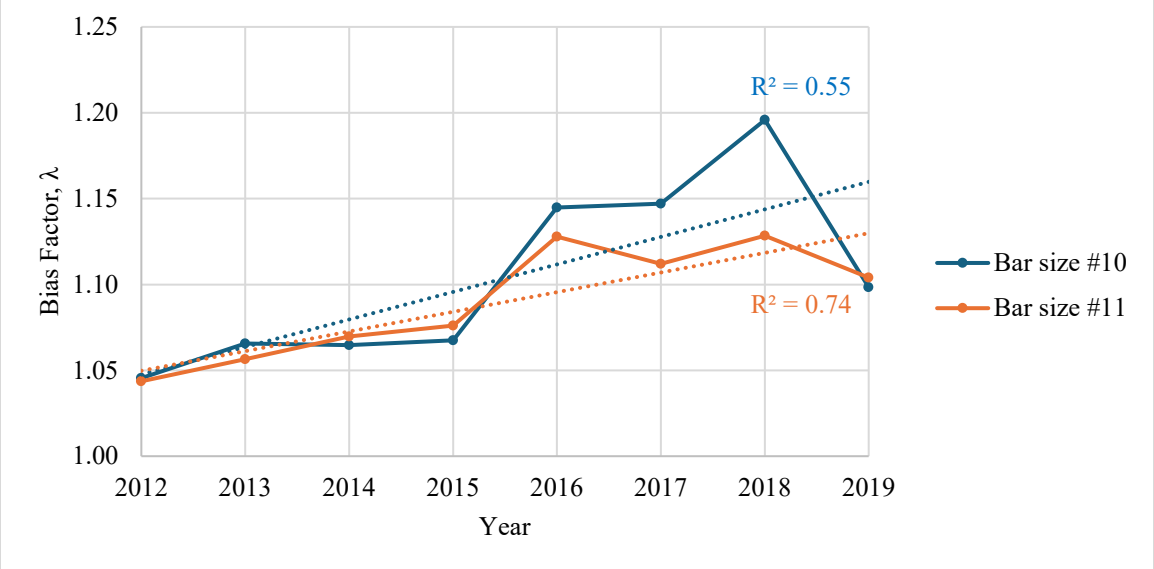

Figure C-10 Evolution Trends of the Bias Factor, λ, for the ASTM A615 Grade 80 Steel (Longitudinal Reinforcement—Large Diameters)

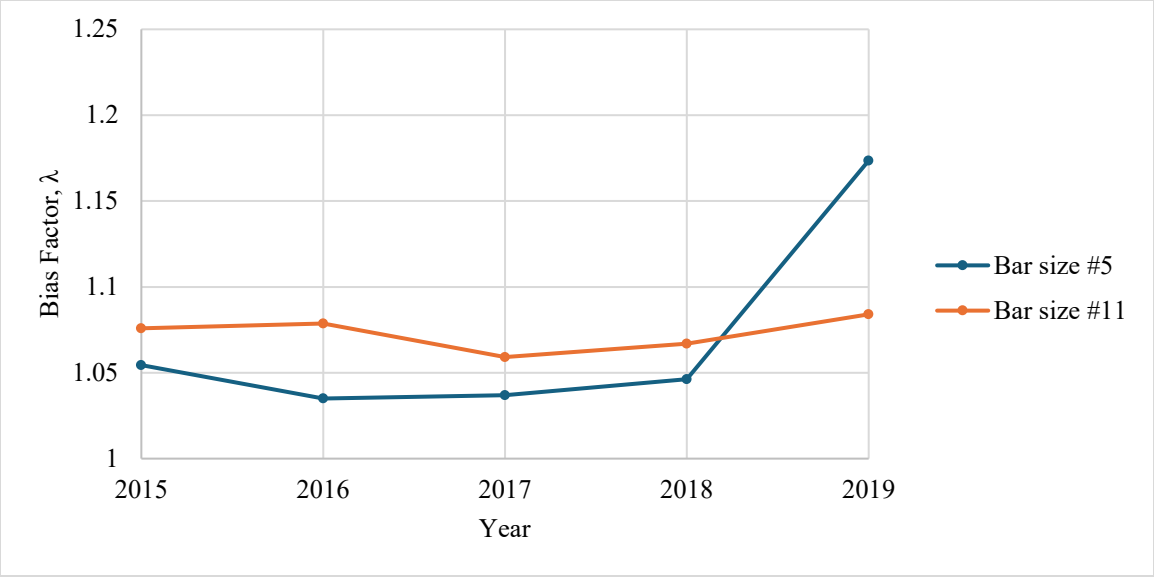

Figure C-11 Evolution Trends of the Bias Factor, λ, for the ASTM A615 Grade 100 Steel

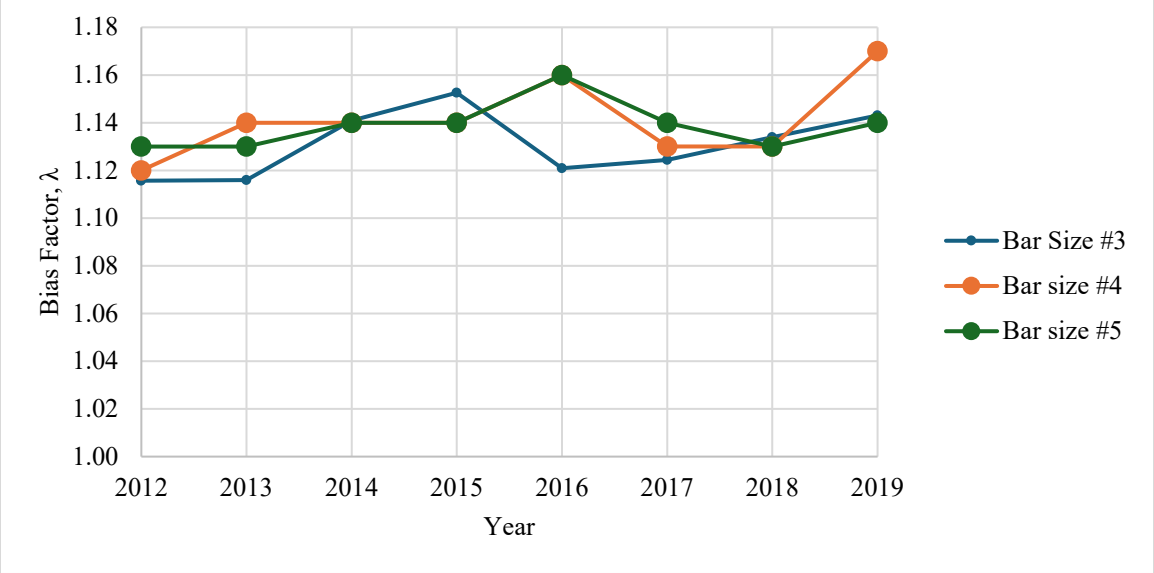

Figure C-12 Evolution Trends of the Bias Factor, λ, for the ASTM A706 Grade 60 Steel (Shear Reinforcement)

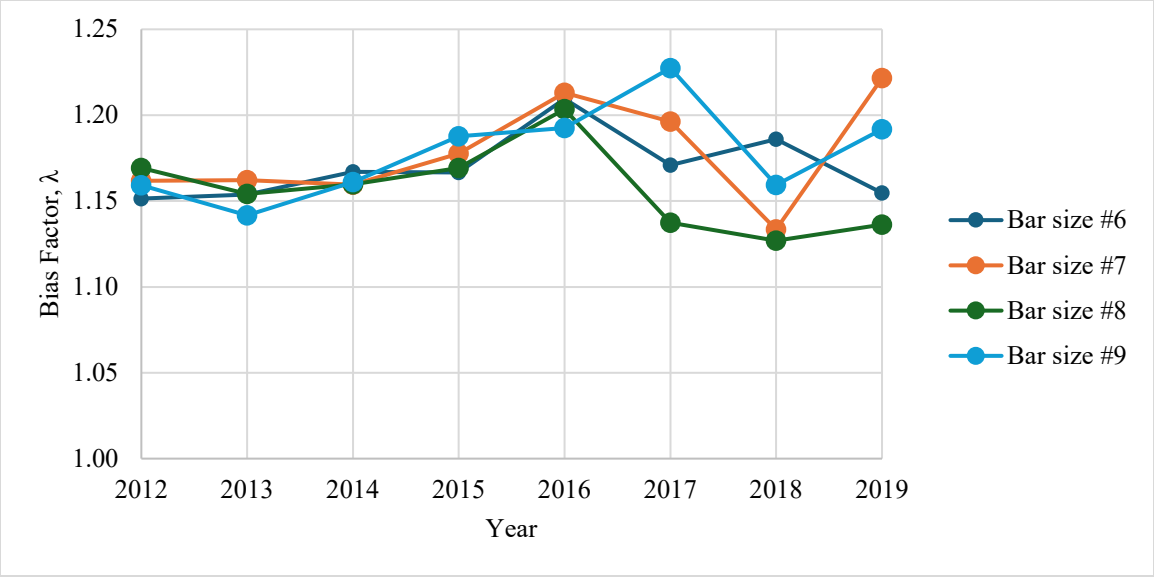

Figure C-13 Evolution Trends of the Bias Factor, λ, for the ASTM A706 Grade 60 Steel (Longitudinal Reinforcement—Common)

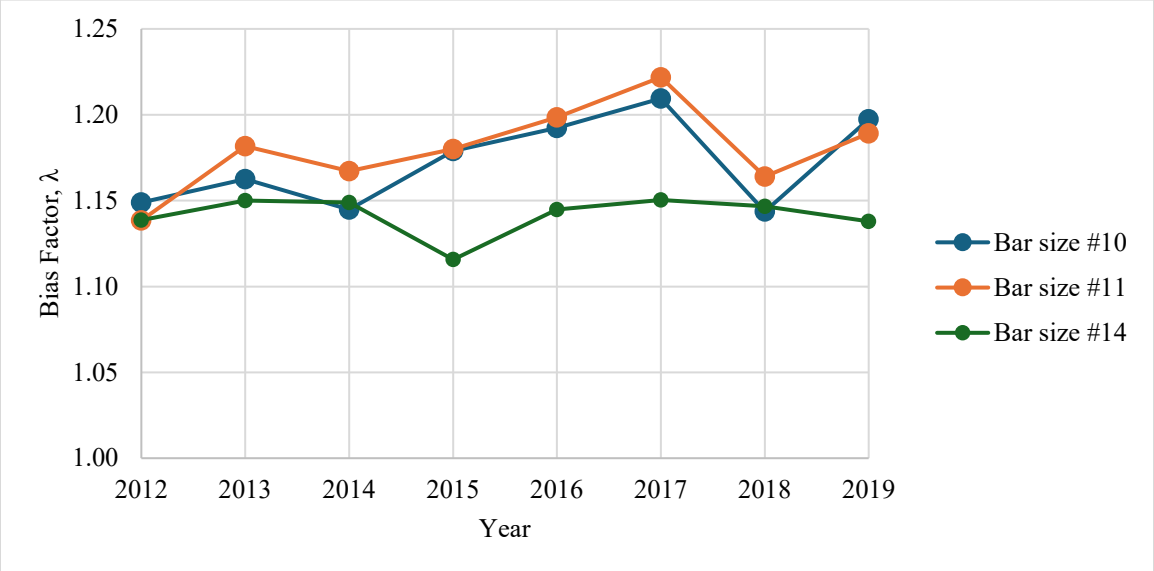

Figure C-14 Evolution Trends of the Bias Factor, λ, for the ASTM A706 Grade 60 Steel (Longitudinal Reinforcement—Large Diameters)

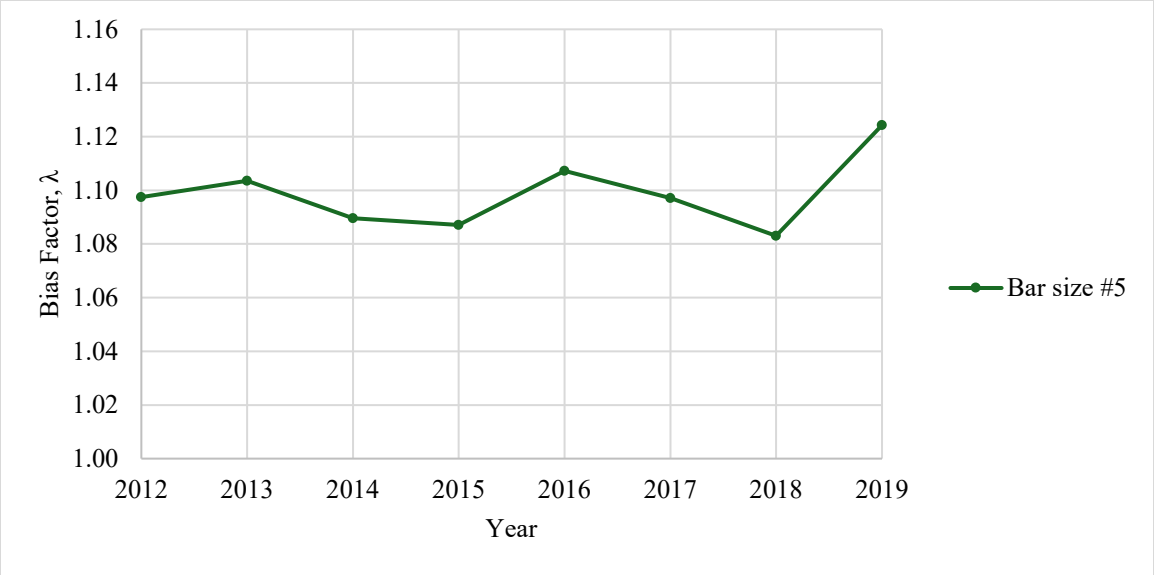

Figure C-15 Evolution Trends of the Bias Factor, λ, for the ASTM A706 Grade 80 Steel (Shear Reinforcement)

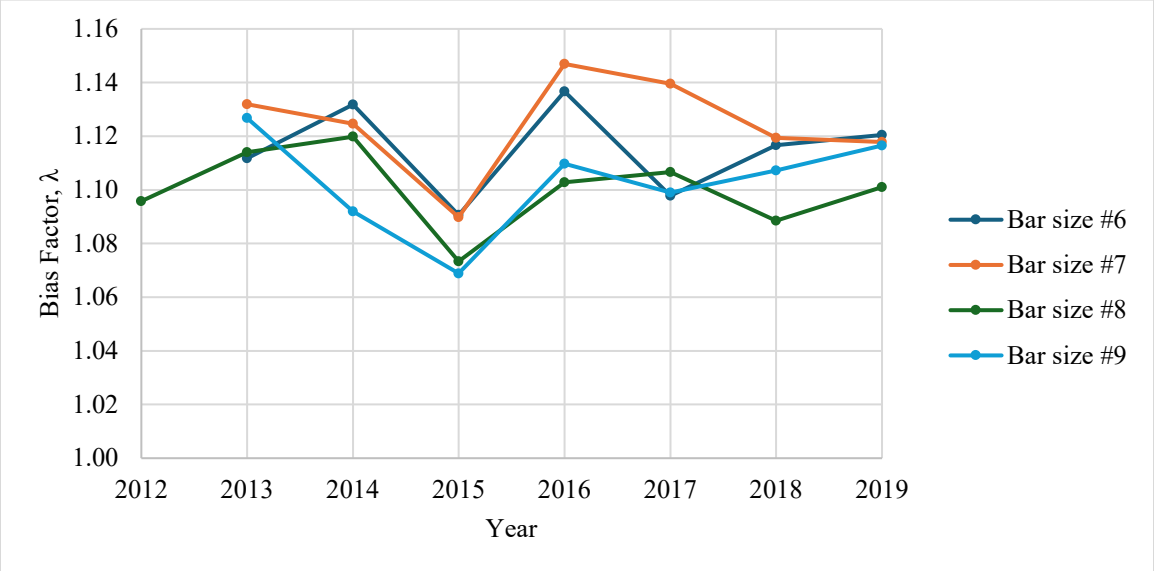

Figure C-16 Evolution Trends of the Bias Factor, λ, for the ASTM A706 Grade 80 Steel (Longitudinal Reinforcement—Common)

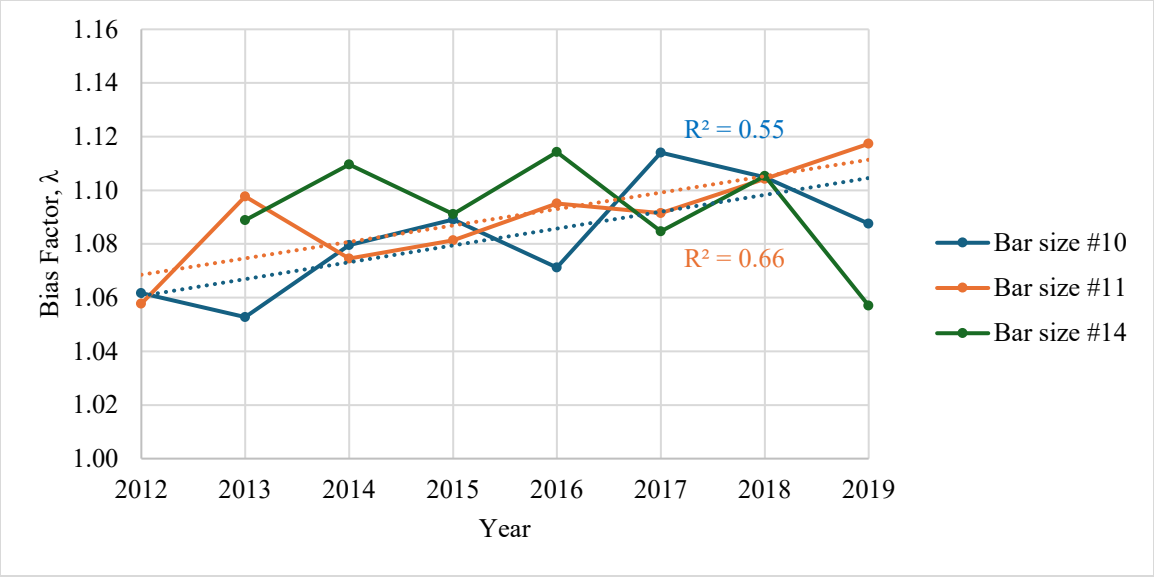

Figure C-17 Evolution Trends of the Bias Factor, λ, for the ASTM A706 Grade 80 Steel (Longitudinal Reinforcement—Large Diameters)

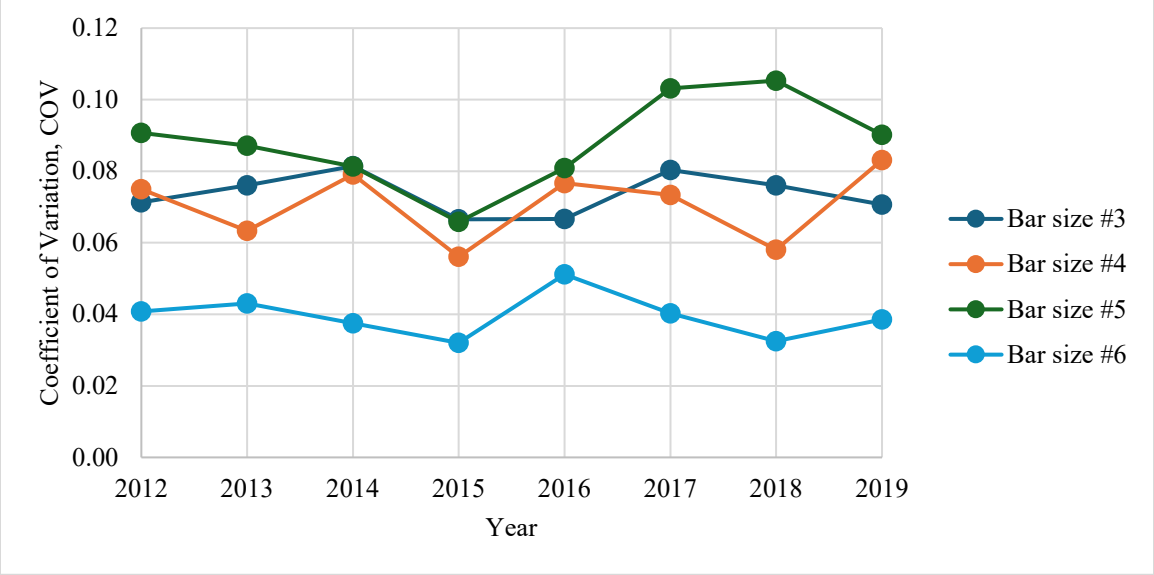

Figure C-18 Evolution Trends of the Coefficient of Variation, COV, for the ASTM A615 Grade 40 Steel

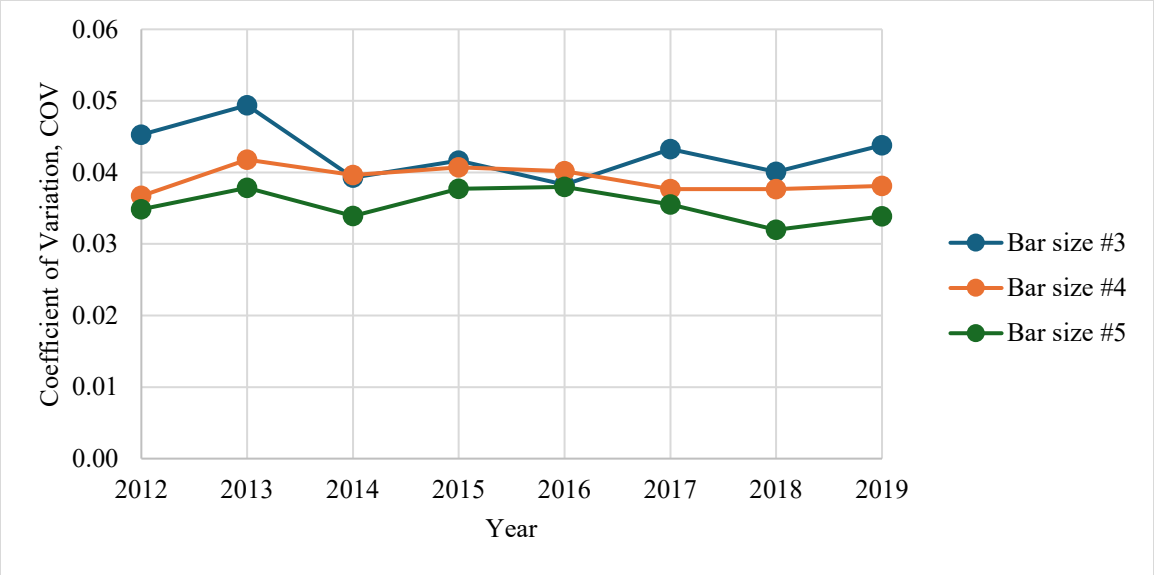

Figure C-19 Evolution Trends of the Coefficient of Variation, COV, for the ASTM A615 Grade 60 Steel (Shear Reinforcement)

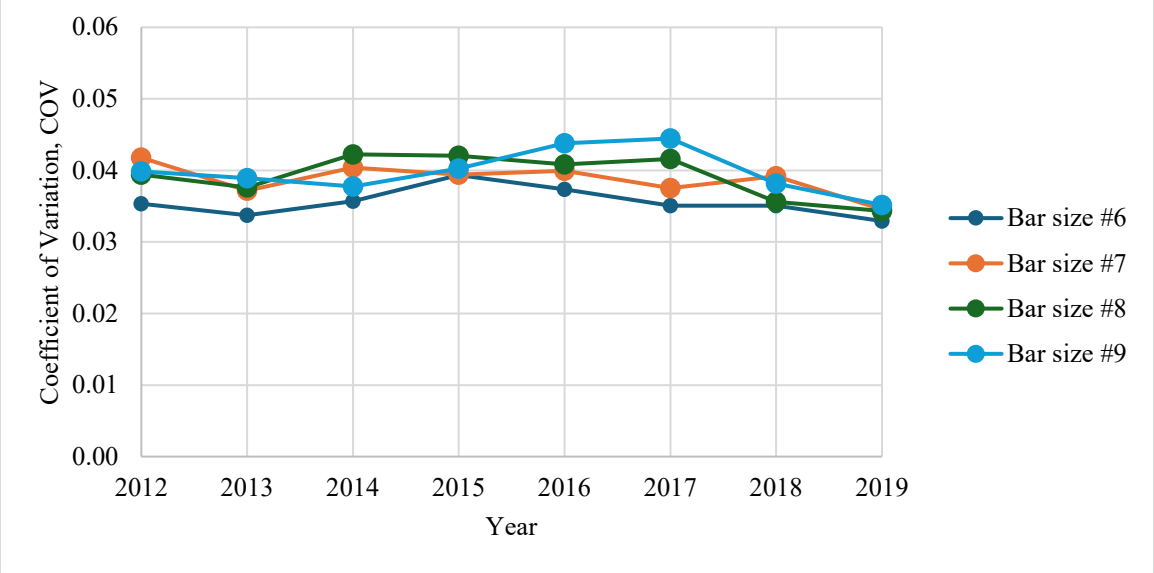

Figure C-20 Evolution Trends of the Coefficient of Variation, COV, for the ASTM A615 Grade 60 Steel (Longitudinal Reinforcement—Common)

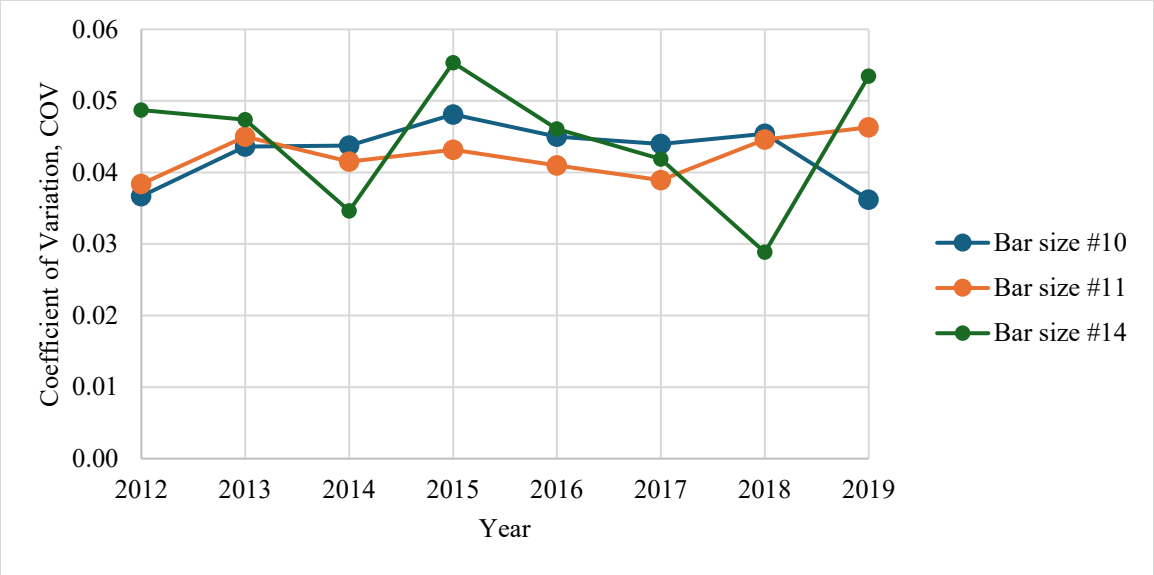

Figure C-21 Evolution Trends of the Coefficient of Variation, COV, for the ASTM A615 Grade 60 Steel (Longitudinal Reinforcement—Large Diameters)

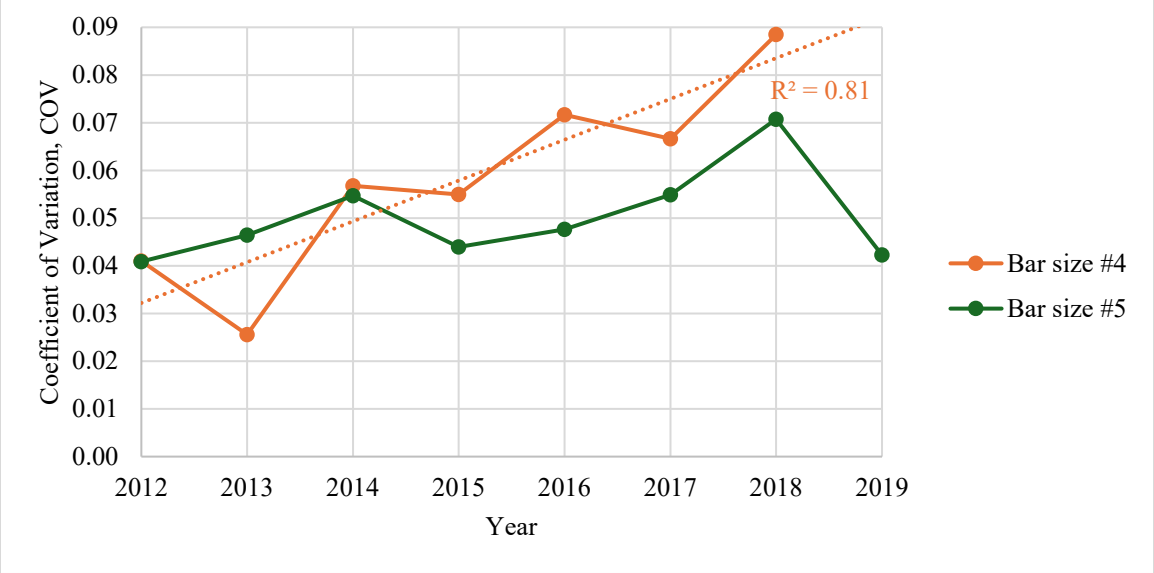

Figure C-22 Evolution Trends of the Coefficient of Variation, COV, for the ASTM A615 Grade 75 Steel (Shear Reinforcement)

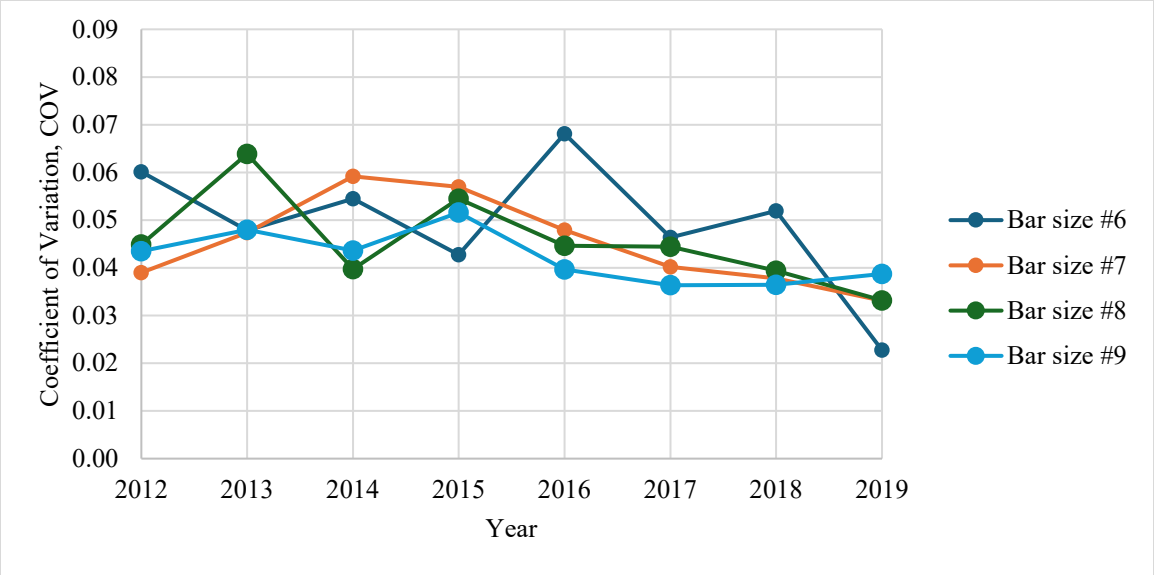

Figure C-23 Evolution Trends of the Coefficient of Variation, COV, for the ASTM A615 Grade 75 Steel (Longitudinal Reinforcement—Common)

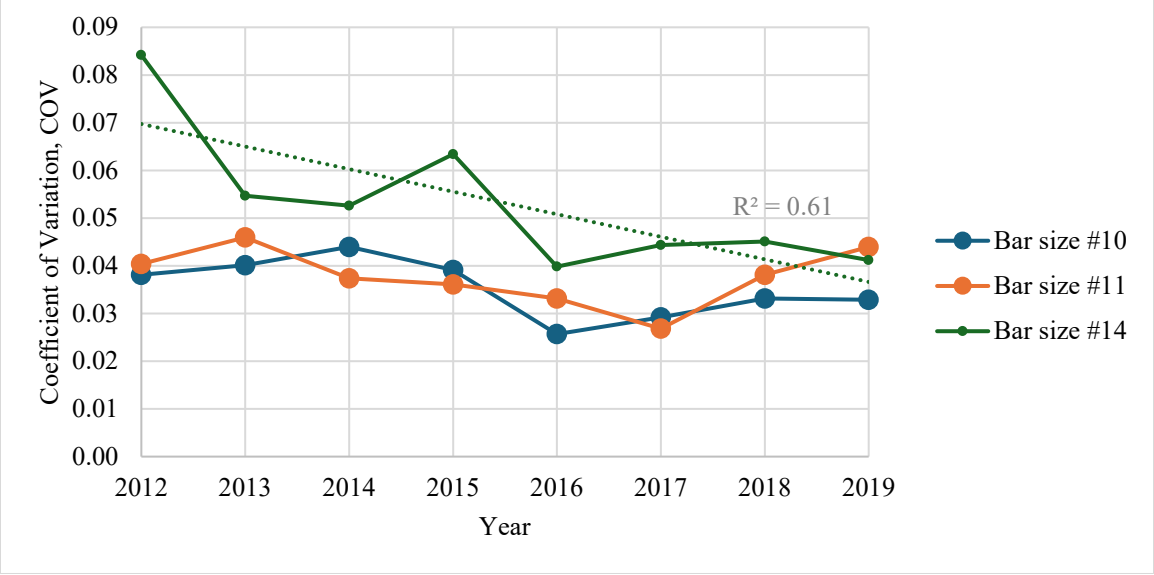

Figure C-24 Evolution Trends of the Coefficient of Variation, COV, for the ASTM A615 Grade 75 Steel (Longitudinal Reinforcement—Large Diameters)

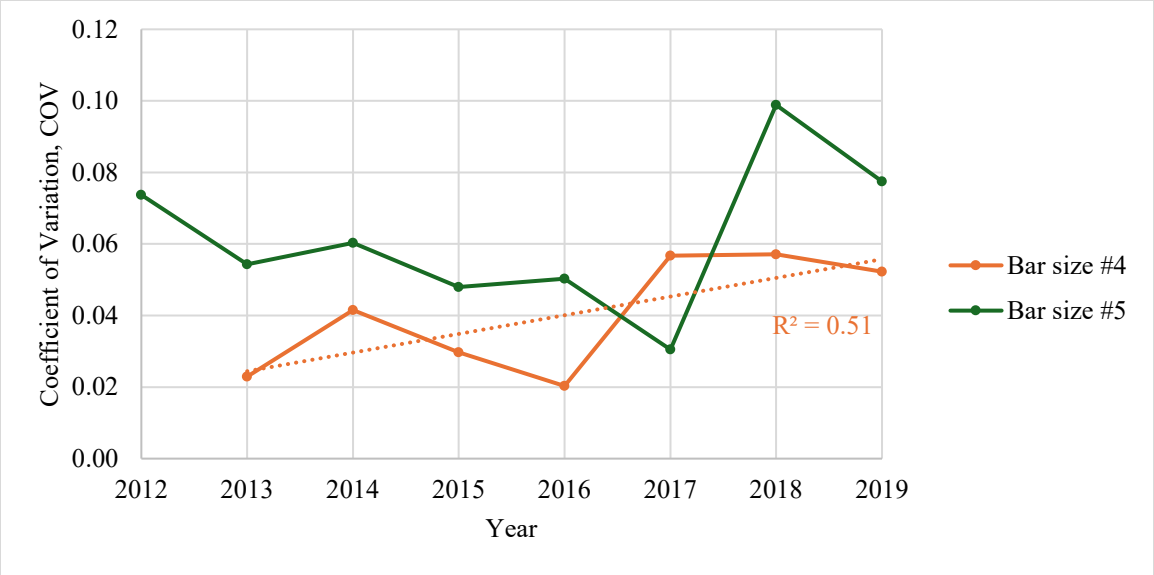

Figure C-25 Evolution Trends of the Coefficient of Variation, COV, for the ASTM A615 Grade 80 Steel (Shear Reinforcement)

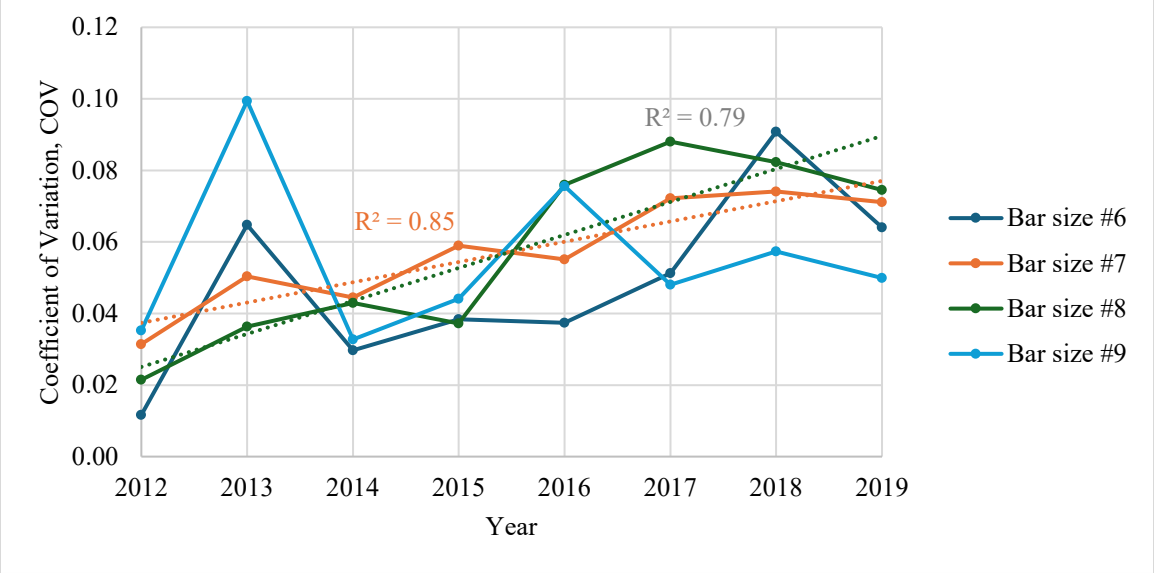

Figure C-26 Evolution Trends of the Coefficient of Variation, COV, for the ASTM A615 Grade 80 Steel (Longitudinal Reinforcement—Common)

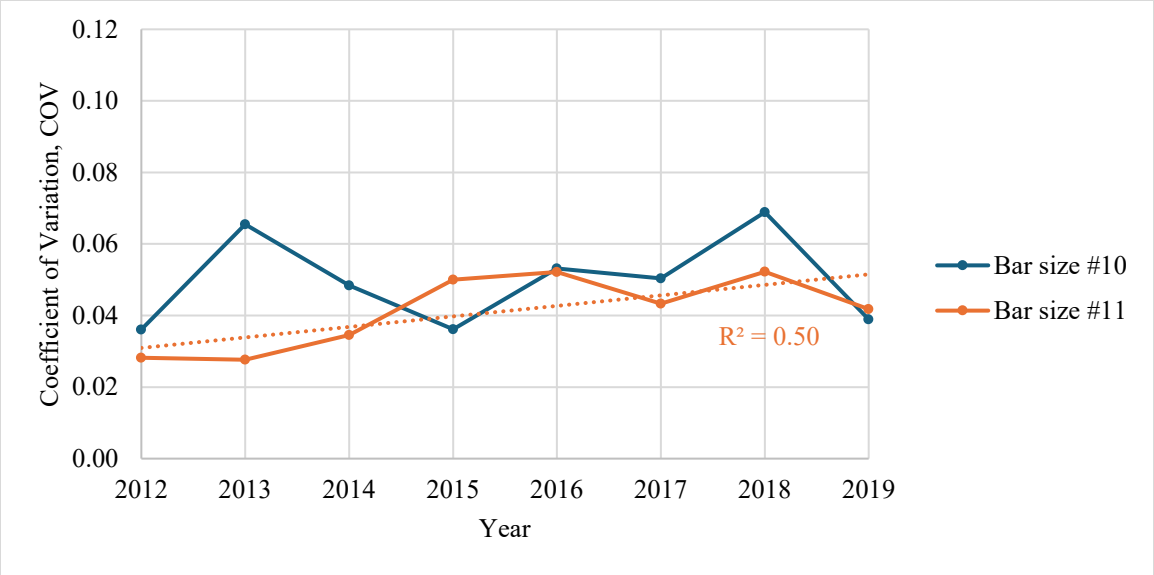

Figure C-27 Evolution Trends of the Coefficient of Variation, COV, for the ASTM A615 Grade 80 Steel (Longitudinal Reinforcement—Large Diameters)

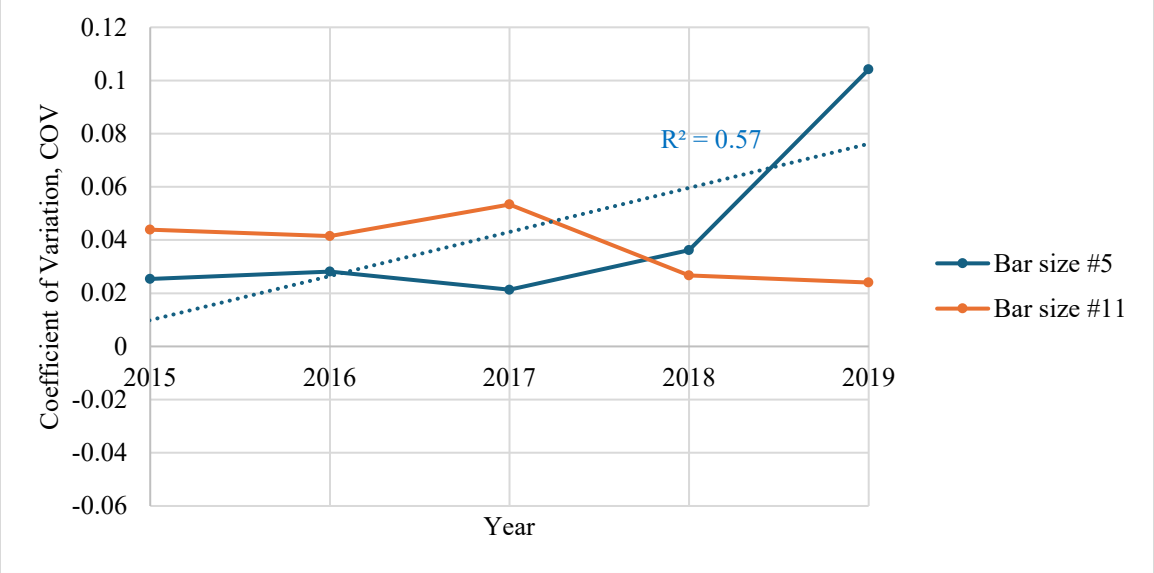

Figure C-28 Evolution Trends of the Coefficient of Variation, COV, for the ASTM A615 Grade 100 Steel

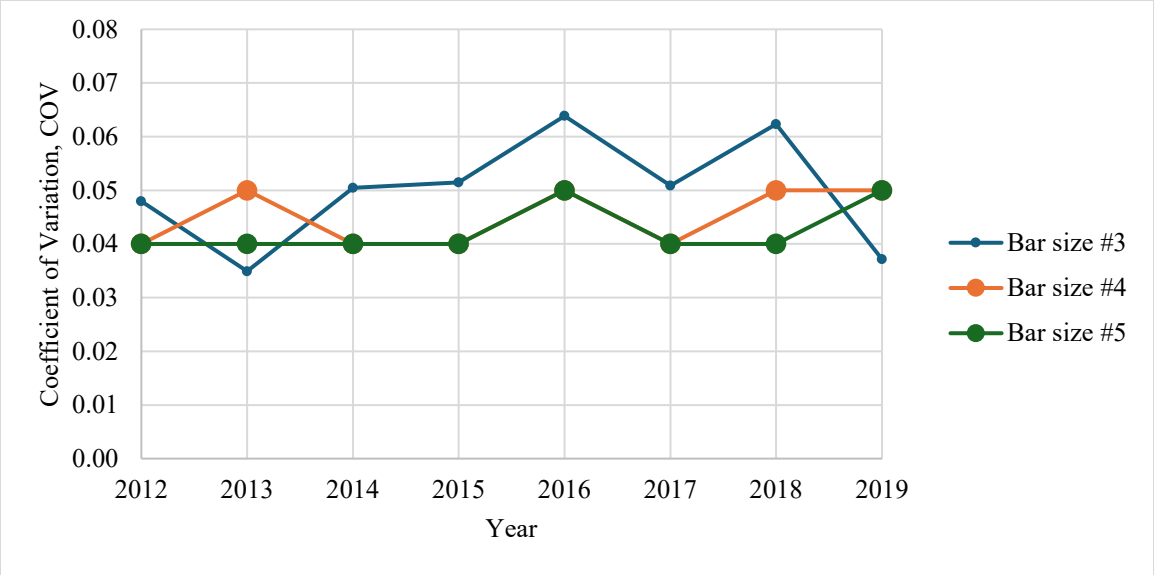

Figure C-29 Evolution Trends of the Coefficient of Variation, COV, for the ASTM A706 Grade 60 Steel (Shear Reinforcement)

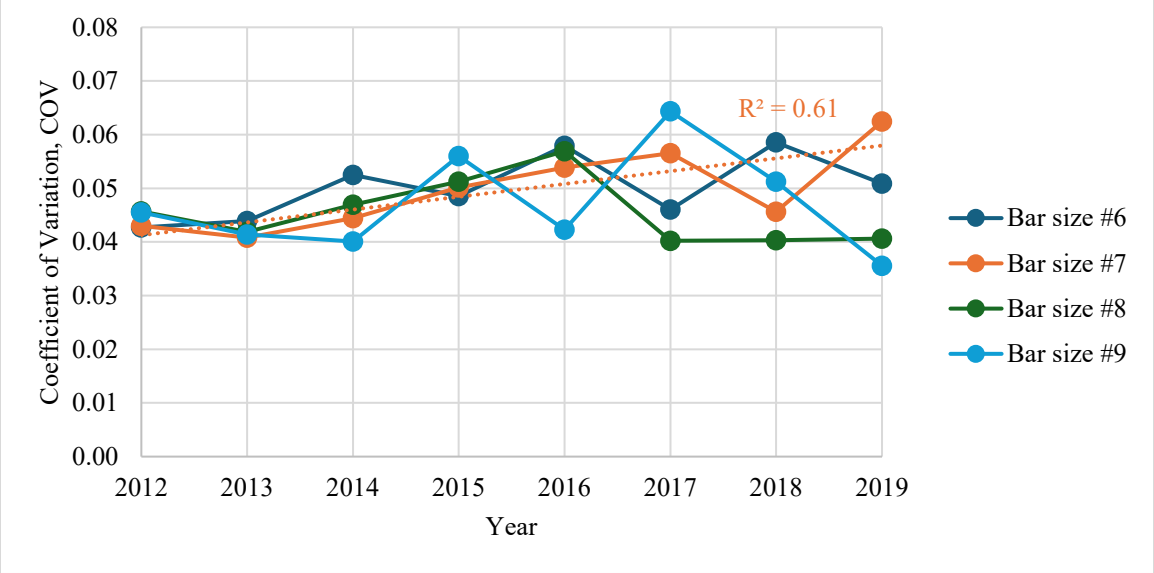

Figure C-30 Evolution Trends of the Coefficient of Variation, COV, for the ASTM A706 Grade 60 Steel (Longitudinal Reinforcement—Common)

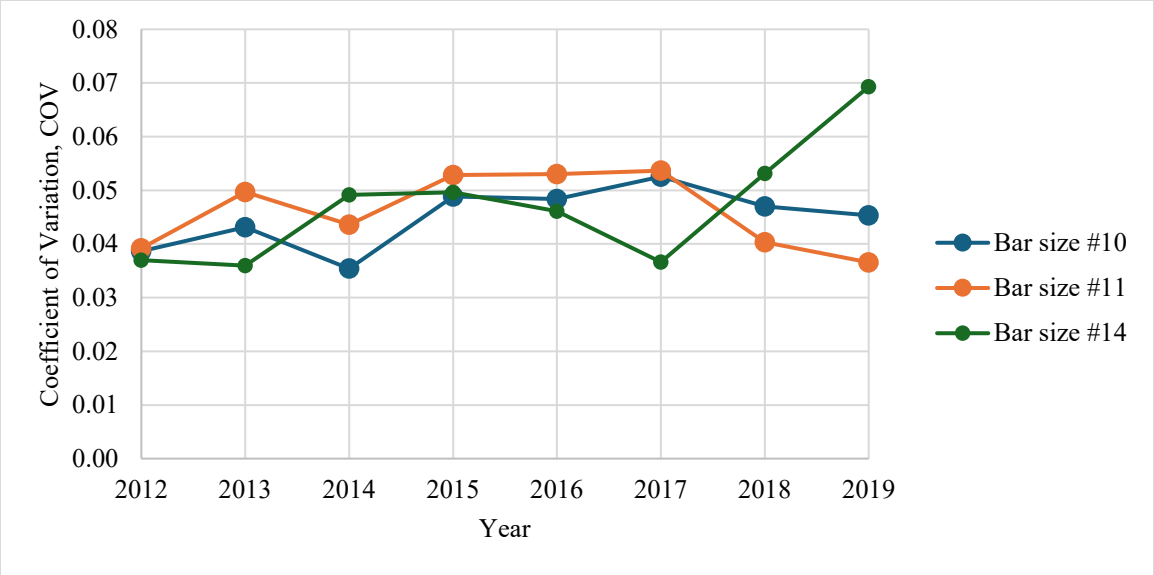

Figure C-31 Evolution Trends of the Coefficient of Variation, COV, for the ASTM A706 Grade 60 Steel (Longitudinal Reinforcement—Large Diameters)

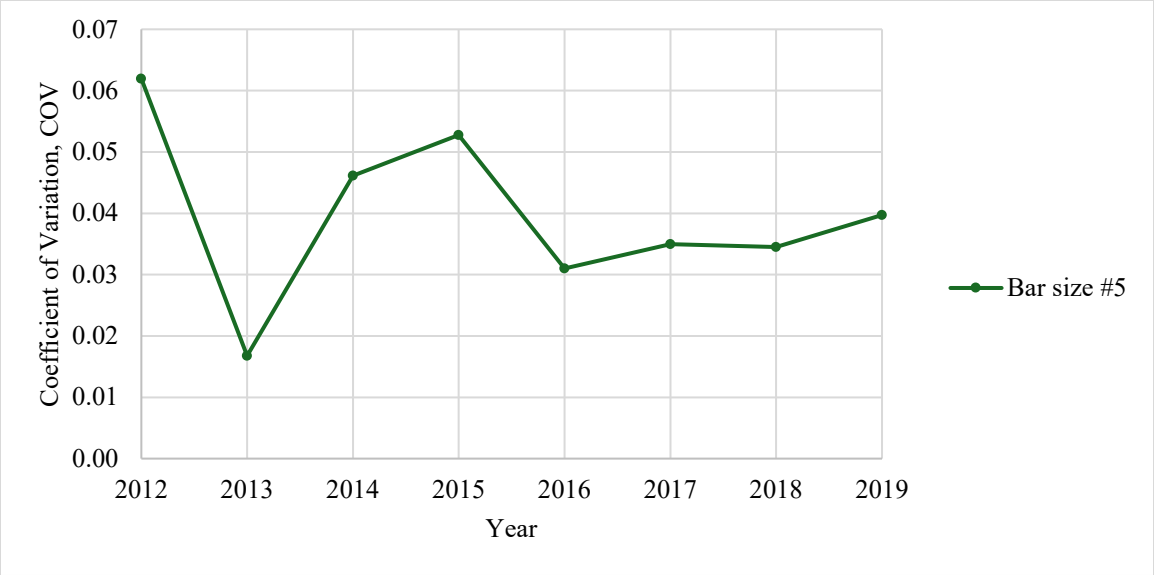

Figure C-32 Evolution Trends of the Coefficient of Variation, COV, for the ASTM A706 Grade 80 Steel (Shear Reinforcement)

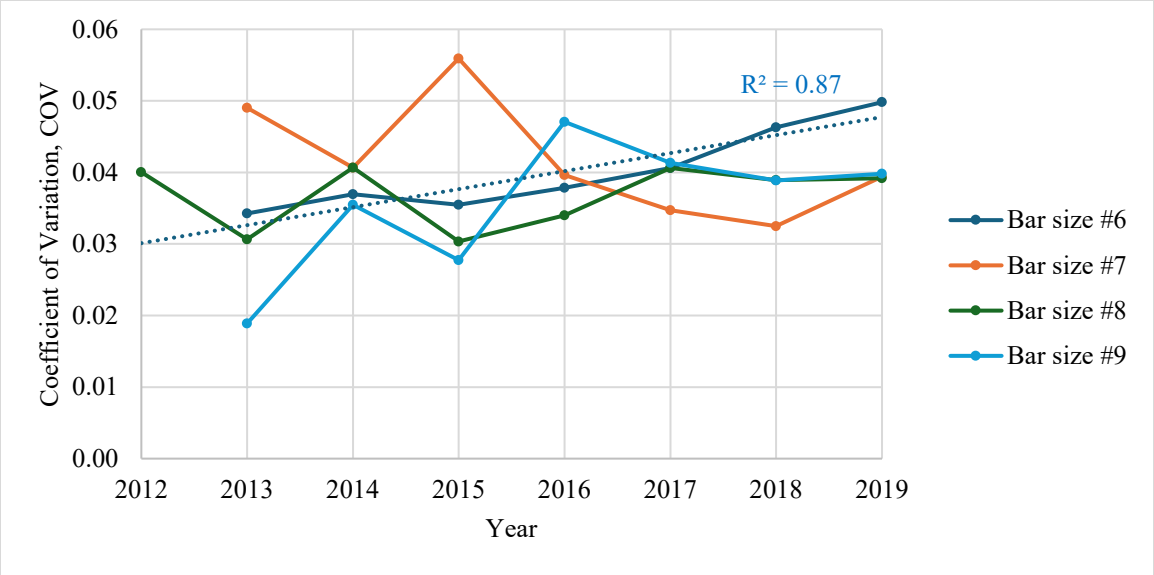

Figure C-33 Evolution Trends of the Coefficient of Variation, COV, for the ASTM A706 Grade 80 Steel (Longitudinal Reinforcement—Common)

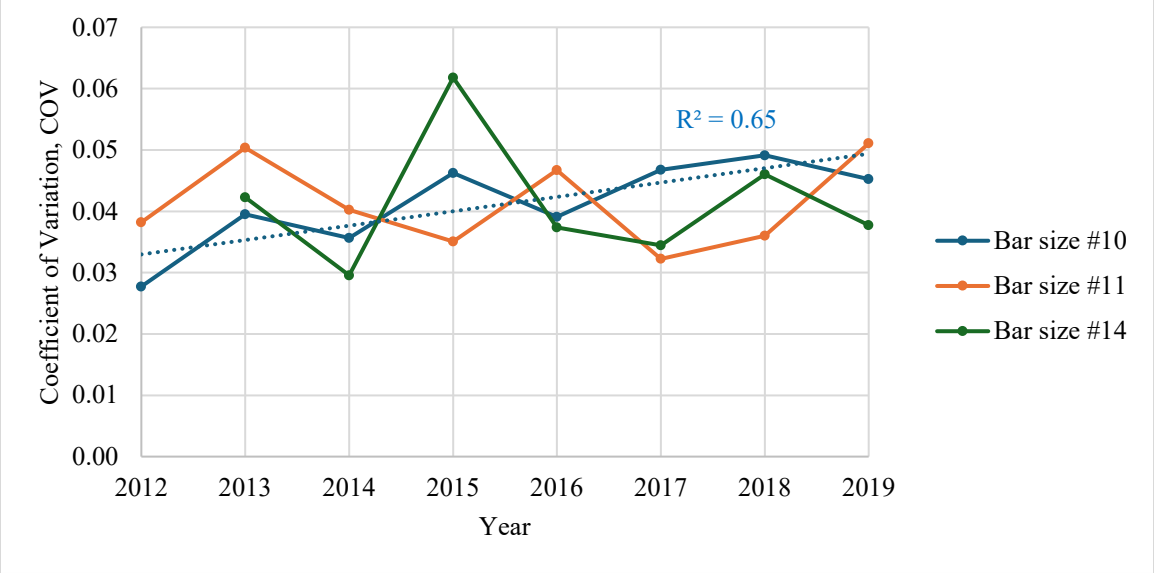

Figure C-34 Evolution Trends of the Coefficient of Variation, COV, for the ASTM A706 Grade 80 Steel (Longitudinal Reinforcement—Large Diameters)